

ISSN 0288-4534
CODEN:KONAE7

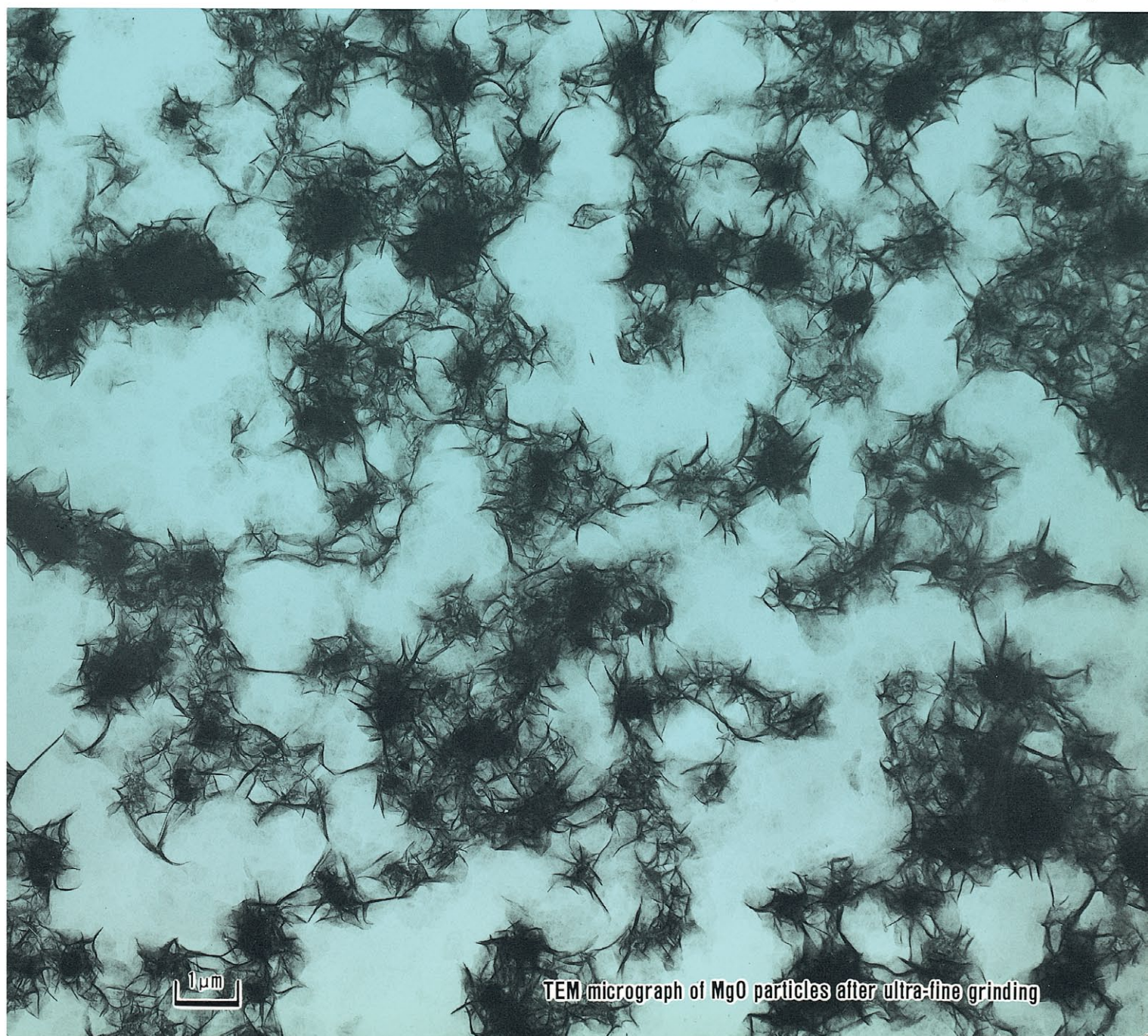
粉

KONA

**POWDER SCIENCE AND
TECHNOLOGY IN JAPAN**

No. 3 (1985)

Published by The Party of Powder Technology (JAPAN)



TEM micrograph of MgO particles after ultra-fine grinding

KONA is aimed, as its subtitle indicates, to introduce annually the recent works on powder science and technology in Japan to the interested parties in the world. It consists of the English version of reports and reviews carefully selected out of the latest papers which were originally written in Japanese.

KONA is distributed without charge to senior researchers, institutions and libraries in this field throughout the world under the sponsorship of Hosokawa Micron Corporation. Within these limits the editors are always glad to consider the addition of names to the mailing list.

Explanation of the Cover

“粉”; This Chinese character is pronounced as “KONA” in Japanese and means “Powder”.
“粉” on the front page was written by the late Mr. Eiichi Hosokawa, founder of Hosokawa Micron Corporation.

Editorial Board

Naoya Yoshioka	(Professor Emeritus of Kyoto University) Editor in Chief.
Masafumi Arakawa	(Professor of Kyoto Institute of Technology)
Masuo Hosokawa	(President of Hosokawa Micron Corp.)
Koichi Iinoya	(Professor of Aichi Institute of Technology)
Genji Jimbo	(Professor of Nagoya University)
Yasuo Kousaka	(Professor of University of Osaka Prefecture)
Kei Miyanami	(Professor of University of Osaka Prefecture)
Takeo Yano	(Professor Emeritus of University of Osaka Prefecture)
Tetsuo Yoshida	(Professor of Chubu University)
Tohei Yokoyama	(Managing Director of Hosokawa Micromeritics Lab.)

Editorial Assistants	
Shigesumi Kobayashi	(Hosokawa International Inc.)
Toyokazu Yokoyama	(Hosokawa Micromeritics Lab.)
Tomoyuki Yamaguchi	(Hosokawa Micromeritics Lab.)



Hosokawa Micromeritics Laboratory & Hosokawa Micron Corporation

Publication Office and Owner of Copyright

The Party of Powder Technology (Japan)
in **Hosokawa Micromeritics Laboratory**

9, Shodai-tajika 1-chome, Hirakata, Osaka 573 Japan

(Complimentary Copy)

Printed in Japan

Contents

A Laser Diagnostic Technique for Sauter Mean Diameter of Fuel Oil Sprays	<i>Hiroyuki Hiroyasu, Masataka Arai and Tsugio Kishi</i>	2
Comparative Data of Particle Size Distribution of Flake Like Particles by Various Methods	<i>Masafumi Arakawa, Tohei Yokoyama, Tomoyuki Yamaguchi and Takawa Minami.</i>	10
Deposition of Charged Aerosol Particles Flowing through Parallel Plates	<i>Hiroaki Masuda, Shunya Ikumi and Takashi Ito</i>	17
Relationships between Particle Size and Fracture Energy for Single Particle Crushing	<i>Yoshiteru Kanda, Shigeru Sano, Fumio Saito and Saburo Yashima</i>	26
Process of Forming Seamless Capsules by Concentric Nozzle System	<i>Toshiyuki Suzuki, Hideki Sunohara and Ryosei Kamaguchi</i>	32
Numerical Simulation of Pneumatic Conveying in a Horizontal Pipe	<i>Yutaka Tsuji, Takao Oshima and Yoshinobu Morikawa</i>	38
Simulation of Moving Granular-Bed Type Heat Exchanger	<i>Tadayuki Minoura, Shun-ichi Mizukami, Hiroyuki Kohama and Takayoshi Asami</i> . .	52
 < Review >		
Experimental Examination on the Shear Process of Powder Bed	<i>Toshio Oshima and Mitsuaki Hirota</i>	63
Behavior of Submicron Particles Suspending in a Fluid	<i>Yasuo Kousaka</i>	69
Tableting and Granulation of Pharmaceutical Materials	<i>Yoshiro Funakoshi</i>	76
Informational Articles		83

See page 25 for description of the cover photograph.

A Laser Diagnostic Technique for Sauter Mean Diameter of Fuel Oil Sprays

Hiroyuki Hiroyasu and Masataka Arai

*Department of Mechanical Engineering
Hiroshima University**

Tsugio Kishi

*Mitsubishi Heavy Industries, Ltd.***

Abstract

A laser diffraction system was used to obtain the history of the Sauter mean diameter of an evaporating fuel spray.

The errors due to the characteristic properties of the laser diffraction method were examined by using many kinds of sprays. Then, the application procedure was established by using a micro-computer system. The sectional Sauter mean diameter was introduced to examine the overall evaporation rate of a spray in hot air. The Sauter mean diameter of gasoline, kerosene and heavy oil sprays were measured. The Sauter mean diameter of an evaporating spray increased once and decreased at the end of the evaporation.

1. Introduction

Evaporation rate of spray and time-resolved Sauter mean diameter of evaporating spray are the controlling factors which determine a combustion rate of a spray and the characteristics of its flame. To predict the spray combustion phenomena, we wanted to find the evaporation rate of an individual droplet in a burning spray. But due to the difficulties of measuring a droplet size in a burning spray and a statistical analysis of a droplet size distribution of an overall spray, we cannot obtain an evaporation rate of a fuel spray in a burning state or in a hot stream. Therefore the knowledge of the spray evaporation was first supplied by the measurement of the volumetric evaporation rate of a spray in a hot stream^{1)~3)}. Since a lack of knowledge of a droplet size distribution cannot be derived from a volumetric evaporation rate, it can not predict a spray

combustion phenomena.

In recent years, the new laser diagnostic technique which is called the laser diffraction techniques was developed^{4)~7)}. The purposes of this report are to present one of the application technique of a laser diffraction system (ST-1800 particle analyzer) to an evaporating fuel oil spray, and to present the method of measuring a sectional Sauter mean diameter which presents an average Sauter mean diameter at any sectional area of a spray. Next, a time-resolved Sauter mean diameter of an evaporating spray was studied in fuel oil sprays.

2. Application of a laser diffraction system to a fuel oil spray

2. 1 Laser diffraction system

An optical technique which is based on the Fraunhofer diffraction makes the on-line measurement of particle size distribution possible. When a spherical particle is illuminated by a parallel beam of monochromatic coherent light, a diffraction pattern is formed, superimposed on the geometrical image, this pattern being large compared with the image. The first diffraction angle on which 84% of the diffraction light is gathered, is expressed as follows:

* Shitami, Saijo, Higashi-Hiroshima, Hiroshima, 724
TEL. 0824 (22) 7111

** Akunoura, Nagasaki, 850
TEL. 0958 (61) 2111

Received April 1, 1985

$$\theta = \tan^{-1} \left(\frac{1.22\lambda}{X} \right) \quad (1)$$

where: θ = diffraction angle of the first peak
 λ = wave length of monochromatic and coherent light
 X = diameter of a particle

If a lens is placed in the light path after the particle and screen placed at the focal plane, then undiffracted light is focussed to a point on the axis and diffracted light forms a pattern or rings around the central spot. Movement of the particle does not cause movement of the diffraction pattern, since light diffracted at angle θ will give the same radial displacement in the focal plane irrespective of the particles' position in the illumination beam. The 'far field' diffraction pattern thus produced is known as a Fraunhofer diffraction pattern.

If, instead of a single particle, we have a collection of particles of different sizes, then the diffraction light from these particles is the sum of the contribution from individual particles. If a detector is used which is divided into a set of circular rings, then each of these rings will define a characteristic particle size. In the practical approach, the Rosin-Rammler distribution is first assumed as a particle size distribution and the pattern of the diffracted light from assumed particles is calculated. Next, the comparison of the assumed diffracted pattern and measured diffracted pattern is made. The most fitting Rosin-Rammler equation is defined by the least square estimating method by reiterating the above procedure.

The measuring system used in this work is shown in Fig. 1. The monochromatic and coherent light of which the wave length was

0.6328 μm and power was 2mW, was radiated by the He-Ne laser. The laser beam was expanded by the beam expander to a parallel laser beam of which the diameter was about 6 mm and illuminated spray particles. The focussing length of a fourier transform lens was 300 mm. The diffract light was detected by the multi-element photo detector. The detected signal was analyzed by the signal processor 1 (DEC, PDP-8/A) according to the program developed by Malvern Instrument Ltd. The signal processor 2 (HP, System 45S) was used to obtain a Sauter mean diameter and further knowledge of a spray size distribution mentioned later. The theory and detail processes of the laser diffraction method have already been reported by the pioneers in this field.

2. 2 Fitting error of a distribution curve

It was considered that there were two different error sources in a measuring system used in this work. One was a fitting error of a Rosin-Rammler distribution equation, and the other was an error due to multi-diffraction by particles which were spatially dispersed in the laser path.

In the routine work developed by Malvern Instruments Ltd. for ST-1800 particle analyzer, the following Rosin-Rammler volumetric distribution function was used:

$$\frac{1}{v} \frac{dv}{dX} = \frac{\beta}{X_p} \left(\frac{X}{X_p} \right)^{\beta-1} \exp \left\{ - \left(\frac{X}{X_p} \right)^{\beta} \right\} \quad (2)$$

where: v = volume of particles
 X = diameter of particle
 X_p = characteristic diameter where it can be seen that a weight fraction $1/e$ ($=0.368$) is larger than X_p and 62.3% of the particles are less than X_p
 β = measure of the spread of the size distribution

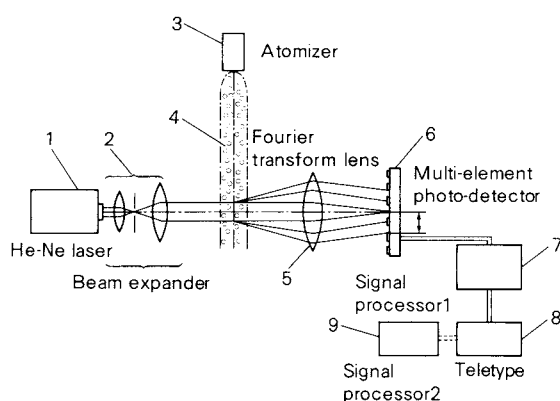


Fig. 1 The measuring system

The fitting error of the Rosin-Rammler function to a spray distribution was tested first. To avoid a multi-diffraction by the particles, the particles which were disposed two-dimensionally on a glass plate were used. The used particles were glass beads which were relatively monodisperse particles and paint particles which were sprayed a far distance from a glass plate and have almost the same size distribution

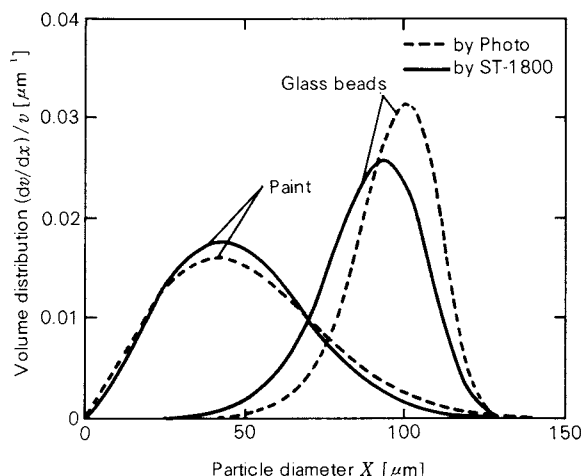


Fig. 2 The comparison of the distribution curves

as a fuel oil spray. **Figure 2** shows the comparison between the Rosin-Rammler distribution curves obtained by ST-1800 particle analyzer and the distribution curves obtained by the micro-photographs of particles. The fitting error is larger for the glass beads than for the paint particles. It was considered that the distribution of the glass beads was more mono-disperse than the distribution of the paint particles and the analyzing program of ST-1800 was developed favorably for poly-disperse particles.

The physical meaning of the Sauter mean diameter X_{32} is more directly connected with an evaporating phenomena of a spray than X_p which was introduced as a characteristic diameter in the Rosin-Rammler equation. Therefore, in this work the Sauter mean diameter X_{32} was printed out as the final output of the particle analyzer. The relation between X_{32} and X_p was obtained by the definition of the Sauter mean diameter and the Rosin-Rammler equation:

$$X_{32} = \frac{X_p}{\Gamma\left(\frac{\beta-1}{\beta}\right)} \quad (3)$$

where: Γ := gamma function of β

Equation (3) was only accurate if the particles were distributed from an infinitely small size to an infinitely large size. But in a spray, there were lower and upper limits of the droplet diameter. Then the Sauter mean diameter of a spray had to be obtained as follows:

$$X_{32} = \frac{\int_{X_a}^{X_b} X^3 dn}{\int_{X_a}^{X_b} X^2 dn} \quad (4)$$

where: X_a = lower limit of diameter
 X_b = upper limit of diameter
 n = number of droplets or particles

If the size distribution of X was expressed as the Rosin-Rammler equation, there was some difference in the Sauter mean diameters obtained by the equations (3) and (4). For example, X_p was 40 μm and β was 1.5 in the Rosin-Rammler equation and the lower and the upper limits of diameter were 5.7 μm and 562.9 μm according to the arrangement of the multi-detector shown in **Fig. 1**. The Sauter mean diameter obtained from equation (3) was 14.9 μm but 24.5 μm was obtained by equation (4). It was considered that the difference was due less to the weight of the smaller size particles than X_a . Therefore in this work, the Sauter mean diameter obtained by equation (4) was used in the further analyses.

Table 1 shows the X_p , β and two kinds of X_{32} of the glass beads and paint particles which were used in **Fig. 1**.

2. 3 Error due to a multi-diffraction

The error due to multi-diffraction was intrinsically unavoidable as long as a spray was being dispersed spatially. The experimental apparatus used for the investigation of a multi-diffraction is shown in **Fig. 3**. The main apparatus consisted of a throat (2) which controlled a flow rate of glass beads, stratified nets (3) for making uniform flow of glass beads and one pair of shutter (4) to control a width of the glass beads flow which was illuminated by a laser beam.

Table 1 The analyzing results of glass beads and paint particles

	Glass beads	Paint particles
X_{32} by micro-photograph	99.1 μm	39.8 μm
X_p	102 μm	56 μm
β	8.6	2.1
X_{32} by the equation (3)	94.4 μm	33.1 μm
X_{32} by the equation (4)	94.7 μm	36.3 μm

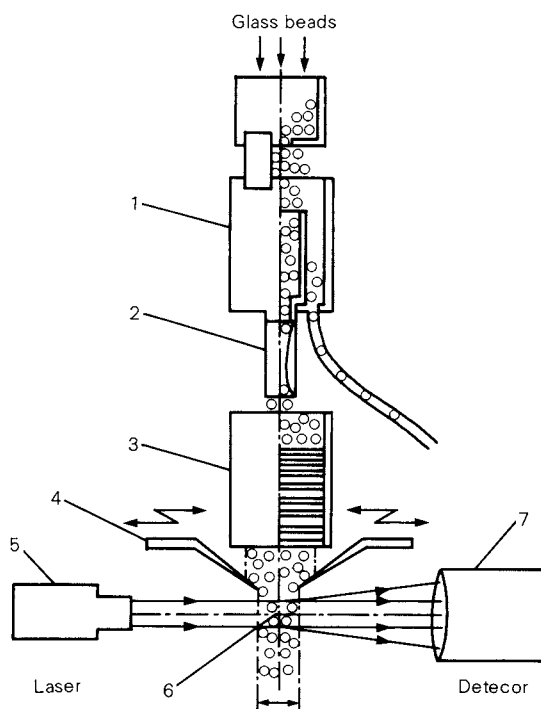


Fig. 3 The apparatus for investigation of the multi-diffraction

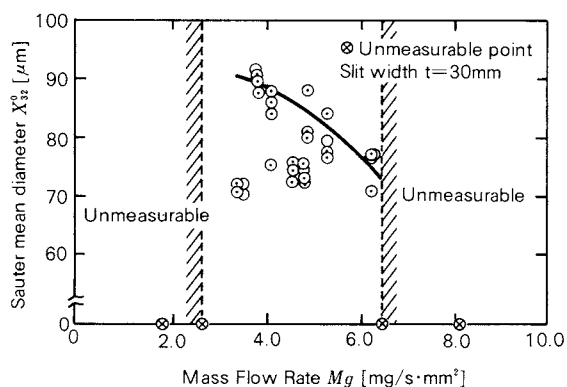


Fig. 4 The effect of mass flow rate on the Sauter mean diameter

Figure 4 shows the effect of the flow rate of glass beads on the measured Sauter mean diameter. X_{32}^0 shows a Sauter mean diameter obtained by the equation (4). At the low flow rate, the Sauter mean diameter was consisted with the results which were obtained by measuring the glass beads on the glass plate. Therefore at the low flow rate, the effect of the multi-diffraction could be neglected. It was clear that by increasing the flow rate, the multi-diffraction effect increased and the Sauter mean diameter decreased. If the multi-diffraction occurred the diffraction angle always increased and it meant that there were some more small

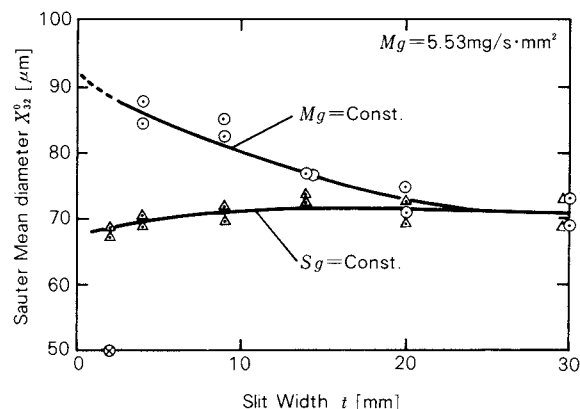


Fig. 5 The effect of the width of the slit on the Sauter mean diameter

particles in the laser path. Other experimental results are shown in Fig. 5. In this figure, $Mg = \text{const.}$ means that the mass flow rate per unit area is constant. And $Sg = \text{const.}$ means that the total mass flow rate measured in the condition of the slit width $t = 30 \text{ mm}$ is $5.53 \text{ mg/(s} \cdot \text{mm}^2)$ and the flow rate per unit area increases being in inverse ratio to the width of the slit. In other words, the total number of particles illuminated by the laser beam is constant. Decreasing the width of the slit, the Sauter mean diameter of $Mg = \text{const.}$ increased and at $t = 0$ it would consist with the results obtained on the glass plate. But the results of $Sg = \text{const.}$ showed almost the same value at any width of the slit. It was considered that if Sg was constant, the effect of the multi-diffraction was the same and it was independent of the width of the slit.

The many kinds of air blast atomizers and pressure-type nozzles were used to make the other kind of spray to calibrate the laser diffraction method. Finally we concluded that the Sauter mean diameter which was obtained by this analyzer (ST-1800) with the slit for a fuel oil spray was about 30% smaller than that obtained by the direct photograph method. Therefore, we used the signal processor (2) in Fig. 1 to correct the final data.

3. Sectional Sauter mean diameter of a spray

3. 1 Measuring apparatus for fuel oil spray

The error due to the multi-diffraction should not be neglected to use this system to measure a fuel oil spray. The Sauter mean diameter of a fuel oil spray could only be calculated from

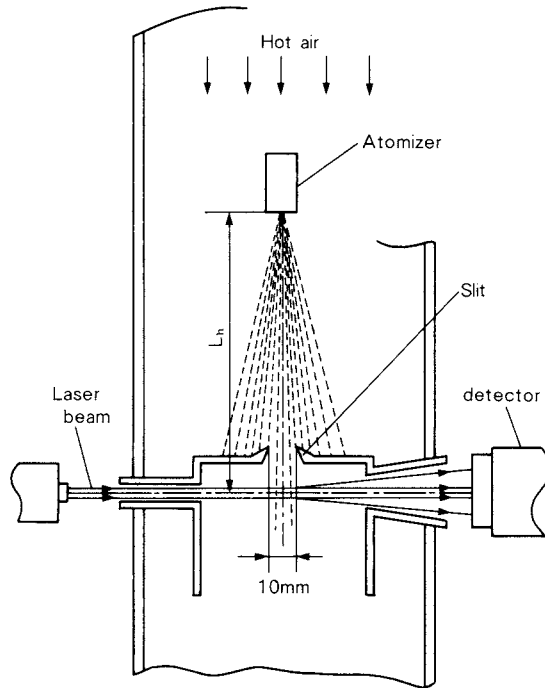


Fig. 6 The experimental apparatus to study a spray evaporation

local Sauter mean diameters which could be measured by the laser diffraction method mentioned above. **Figure 6** shows the experimental apparatus used for the study of spray evaporation. This apparatus consisted of a wind tunnel, an air blast atomizer, a slit and the laser diffraction system. The atomizing condition was determined by flow rate of atomizing air W_a , flow rate of atomized liquid W_l and air orifice diameter D_a .

3. 2 Calculation of a sectional Sauter mean diameter

A local Sauter mean diameter and a droplet density were not constant in a spray. Then to know a sectional Sauter mean diameter which presented the overall Sauter mean diameter of droplets that existed in any sectional area of a spray, it was necessary to measure the distributions of the Sauter mean diameter and the droplet density in this sectional area of a spray. The droplet density of a spray at any location was calculated by the following equations:

$$\rho = \frac{S}{U} \quad (5)$$

$$S = \frac{Q}{A} \quad (6)$$

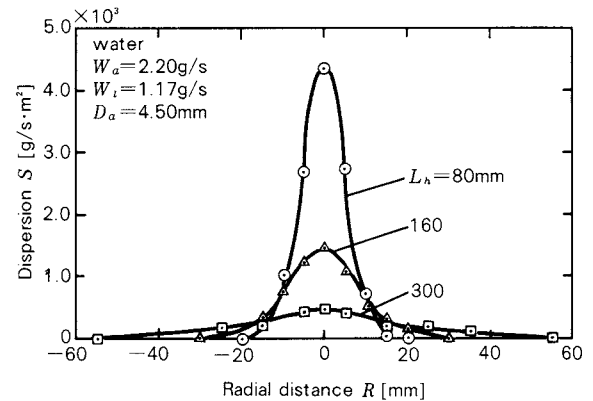


Fig. 7 Radial distribution of the dispersion

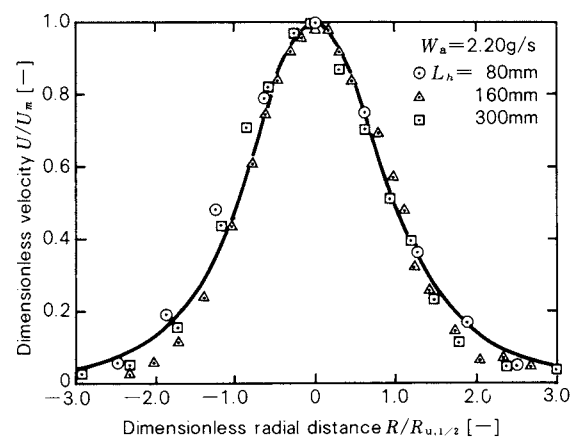


Fig. 8 Radial distribution of the dimensionless velocity

where: ρ = droplet density, g/(m³ air)
 S = dispersion, g/(s.m²)
 U = velocity of droplet, m/s
 A = sampling area, m²
 Q = sampled mass of droplet, g/s

A droplet in a spray had its own velocity which was different from another droplet. Since in a spray atomized by an air blast atomizer, the droplet velocity was almost the same as the atomizing air velocity. The gas velocity measured by a hot wire method was used as the droplet velocity in this study. The dispersion S was calculated by a sampling area and sampled mass of droplets which were captured by an isokinetic sampling probe.

One of the results of the measured dispersions is shown in **Fig. 7**. The dispersion on the spray axis took the highest value and it decreased by increasing the axial distance from the atomizer. **Figures 8 and 9** show the dimensionless expression of the velocity and the dispersion at $L_h = 80$ mm, 160 mm and 300 mm,

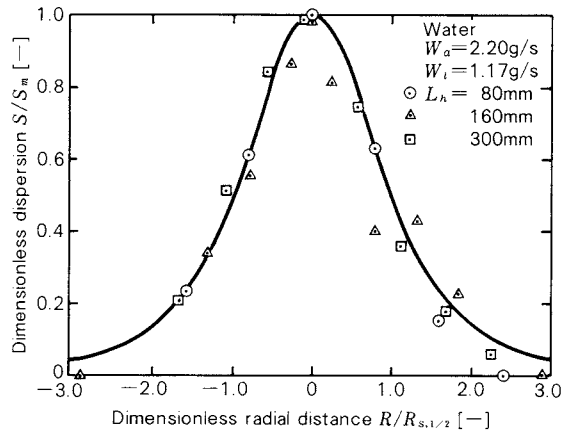


Fig. 9 Radial distribution of the dimensionless dispersion

respectively. The solid lines were the calculated results obtained by the following Gortler's⁸⁾ equations:

$$\frac{U}{U_m} = 1 / \left\{ 1 + 0.414 \left(\frac{R}{R_1} \sqrt{\frac{\sqrt{U_m/U_1} - 1}{0.414}} \right)^2 \right\}^2 \quad (7)$$

$$\frac{S}{S_m} = 1 / \left\{ 1 + 0.414 \left(\frac{R}{R_1} \sqrt{\frac{\sqrt{S_m/S_1} - 1}{0.414}} \right)^2 \right\}^2 \quad (8)$$

where: R = radial distance from a spray axis
 Subscript m = spray axis
 Subscript 1 = any position except a spray axis

$R_{u,1/2}$, $R_{s,1/2}$, $R_{\rho,1/2}$ = radial distance where u or S or ρ took the half value of the maximum

The estimated distributions of the velocity and the dispersion fit well to the experimental results. Therefore, for the simplification and rapidity of the experimental procedure, equations (7) and (8) could be used instead of the full experiments. If these equations were adopted, the measuring positions of the velocity and the dispersion were reduced to two points, that is, the positions on the spray axis and one of the other points. Usually, the position where U or S took the half value of the U_m or S_m was used as the position 1 respectively. The droplet density was calculated using equations (7) and (8) or the experimental distributions of the velocity and the dispersion. The droplet density obtained from Figs. 8 and 9 are shown in Fig. 10. The estimated results expressed as the solid line also fit well to the calculating

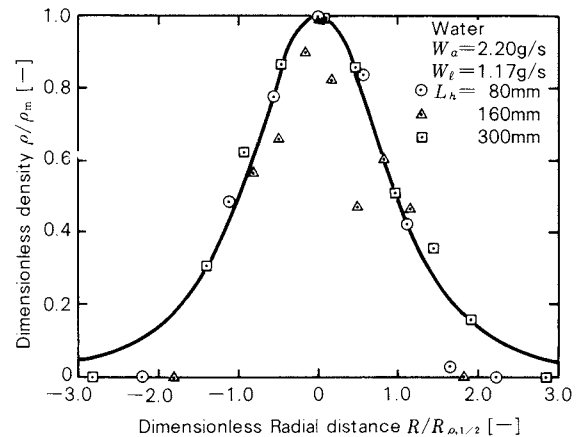


Fig. 10 Radial distribution of the dimensionless droplet density

results based on the measured U and S . Therefore, equations (7) and (8) were used in the following analysis.

The sectional Sauter mean diameter X_{32} could be calculated by considering the droplet density, as follows.

$$\bar{X}_{32} = \frac{\sum_i \sum_j X_i^3 \rho(R_j) \Delta n(X_i, R_j)}{\sum_i \sum_j X_i^2 \rho(R_j) \Delta n(X_i, R_j)} \quad (9)$$

The outline of the calculating procedure is shown in Fig. 11. This procedure was programmed in the signal processor 2 in Fig. 1 as the routine work.

4. Sauter mean diameter of evaporating spray

4. 1 Water spray

Sauter mean diameter of evaporating spray in a hot air stream was studied by the laser diffraction measuring system mentioned above. The effect of the ambient temperature T_a on the sectional Sauter mean diameter along the spray axis is shown in Fig. 12. The sectional Sauter mean diameter increased by increasing the axial distance from the atomizer. The effect of the ambient temperature on \bar{X}_{32} increased by increasing the ambient temperature. It was considered that the evaporation rate of every droplet increased by increasing the ambient temperature. According to the theoretical analysis studied by the authors⁹⁾, it was considered as follows: When the air temperature was high, the relatively small droplets in the spray evaporated quickly before the relatively large droplets in the spray being heated up to the beginning of the evaporation. There-

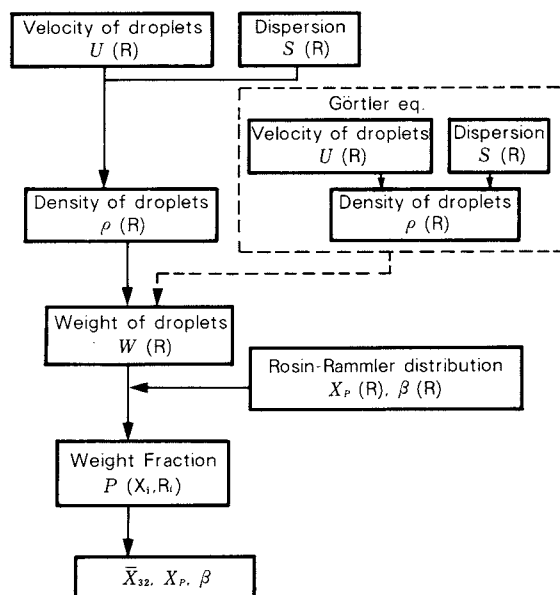


Fig. 11 The flow chart for calculating the sectional Sauter mean diameter

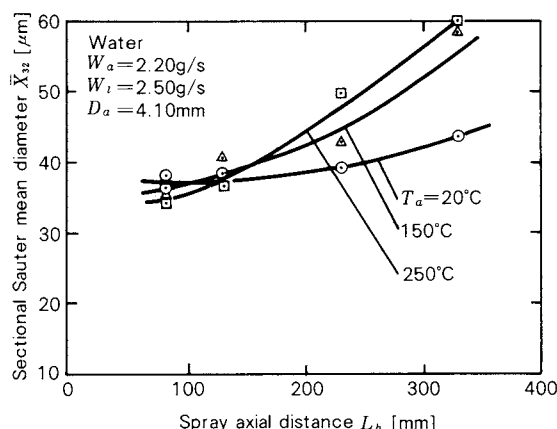


Fig. 12 Sectional Sauter mean diameter of water spray ($W_i = 2.5\text{g/s}$)

fore the increment of the sectional Sauter mean diameter at $T_a = 250^\circ\text{C}$ was larger than at $T_a = 20^\circ\text{C}$. **Figure 13** shows another result. In this case, the flow rate of atomized water was lower than in **Fig. 12**. When the ambient temperature was 250°C , the sectional Sauter mean diameter increased from $26\mu\text{m}$ up to $46\mu\text{m}$ and it was suddenly impossible to measure because of almost 'all of the spray droplets evaporated completely.

4. 2 Fuel oil spray

The sectional Sauter mean diameters of an evaporating spray of fuel oils were very important to know for the spray combustion

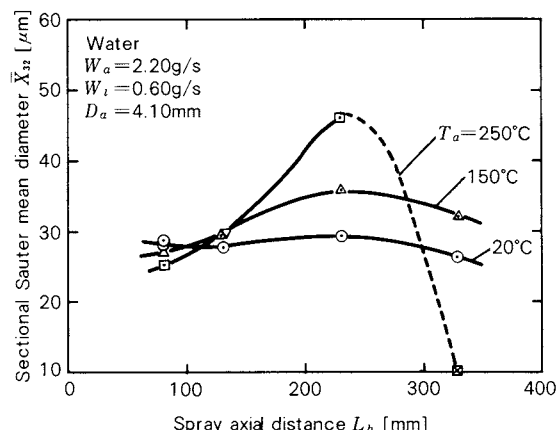


Fig. 13 Sectional Sauter mean diameter of water spray ($W_i = 0.6\text{g/s}$)

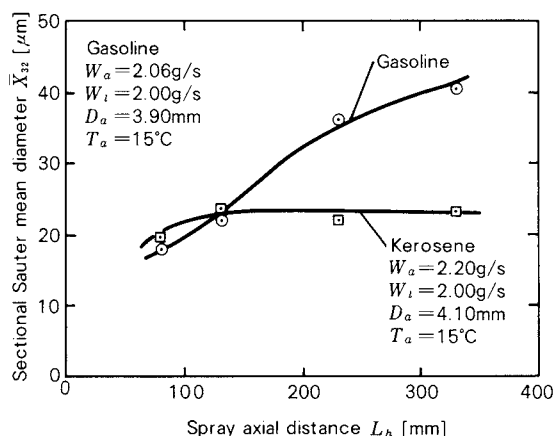


Fig. 14 Sectional Sauter mean diameter of a gasoline spray and a kerosene spray

phenomena of these fuels. So in this study, gasoline, kerosene and heavy oil were chosen as the high, medium and low volatile fuel, respectively. **Figure 14** shows the results of gasoline and kerosene spray at room temperature. The initial Sauter mean diameter of these sprays were almost the same. The sectional Sauter mean diameter of the kerosene spray was not changed along the spray axis, but that of the gasoline spray increased rapidly. **Figure 15** shows the results of the heavy oil. In this case, the fuel temperature T_f was 90°C because at room temperature the viscosity of heavy oil was too high to be atomized.

Figure 16 shows the effect of the ambient air temperature on the sectional Sauter mean diameter of the kerosene spray. When the temperature increased from the room temperature to 50°C , the tendency of the increment of \bar{X}_{32} along the spray axis increased, but this effect

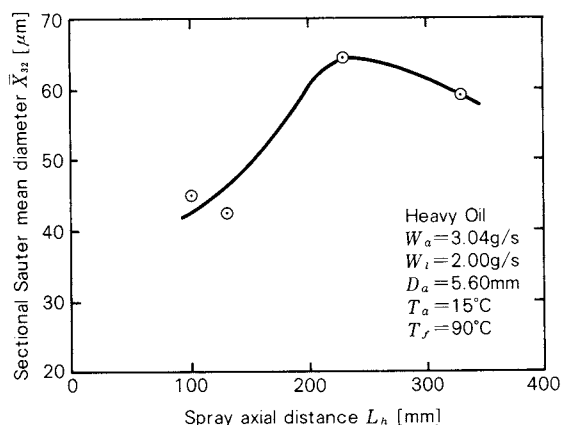


Fig. 15 Sectional Sauter mean diameter of a heavy oil spray

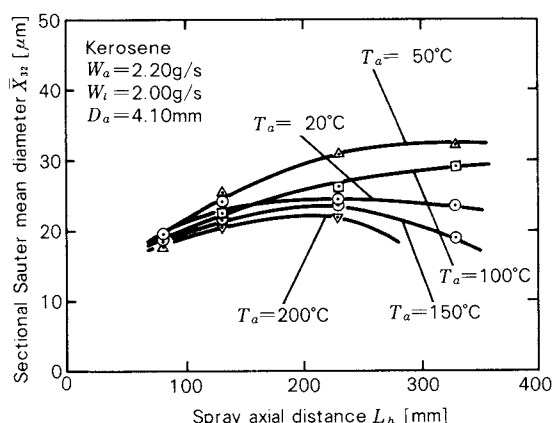


Fig. 16 The effect of the ambient air temperature on the sectional Sauter mean diameter of a kerosene spray

was not clear at temperatures higher than 50°C . In the condition of $T_a = 150^\circ\text{C}$, the sectional Sauter mean diameter increased once but after some axial position it decreased.

5. Conclusions

The laser diffraction method developed by Malvern Instruments Ltd. was modified to measure the sectional Sauter mean diameters of sprays. The modified points and the experimental results are as follows:

- (1) The multi-diffraction effect of this system could not be avoided. Therefore, the some

correction factors and the slit were used to measure the Sauter mean diameter of a fuel spray.

- (2) To know the sectional Sauter mean diameter of the spray, the theoretical analysis and the routine program for this analysis were made.
- (3) The distribution of the Sauter mean diameter of the fuel sprays was measured. The experimental results showed that the Sauter mean diameter in the evaporating spray increased and then decreased along the spray axis.

References

- 1) Tacina, Robert R.: "Degree of vaporization using an air blast type fuel injector for a premixed pre-vaporized combustor", *ICLAS '78* (1978) 369-375.
- 2) Rao, K.V.L. and A.H. Lefebvre: "Evaporation Characteristics of Kerosene Spray Injected into a Flowing Air Stream", *Combustion and Flame*, **26** (1976), 303-309.
- 3) Habib, I.S.: "The Interaction of a Hot Gas Flow and a Cold Liquid Spray in Channels", *Trans. of the ASME*, August (1976), 421-426.
- 4) Caroon, T.A. and G.L. Borman: "Comments on Utilizing the Fraunhofer Diffraction Method for Droplet Size Distribution Measurement", *Combustion Science and Technology*, **19** (1979), 255-258.
- 5) Azzopadi, B.J.: "The analysis of Malvern ST-1800 output by different models and a comparative test of a near monodisperse distribution": *AERE-M3067* (1980).
- 6) Swithenbank, J., J.M. Beer, D.S. Taylor, D. Abbot and G.C. McCreath: "A Laser Diagnostic Technique for the Measurement of Droplet and Particle Size Distribution", *AIAA Paper* 76-69 (1976).
- 7) Felton, P.G.: "In-stream Measurement of Particle Size Distribution", International Symposium on In-stream Measurements of Particle Solid Properties, in Bergen, Norway, Aug. 22&23 (1978).
- 8) Gortler, H.: "Berechnung von Aufgaben der freien Turbulenz auf Grund eines neuen Nährungsansatzes", *Z. angew. Math. Mech.*, **22** (1942), 241-254.
- 9) Tharwat M. Farag, M. Arai and H. Hiroyasu: "Effects of Temperature and Fuel Volatility on Spray Evaporation Characteristics", *Mem. Fac. Eng. Hiroshima Univ.*, **8**, No.1 (1982), 31-39.

Comparative Data of Particle Size Distribution on Flake Like Particles by Various Methods[†]

Masafumi Arakawa

*Department of Inorganic Materials
Kyoto Institute of Technology**

**Tohei Yokoyama, Tomoyuki Yamaguchi
and Takawa Minami**

*Hosokawa Micromeritics Laboratory***

Abstract

The results of the particle size measurements by several methods based on different principles are almost equal to each other as far as these methods are applicable, when the powder is considered to be made of sphere shape particles. However, there are some questions about the particle size measurement of irregular shape particles such as plate or needle like powder. Using mica powders as samples of the thin plate like particles, we compared the results of particle size measurements based on six different principles; optical microscope, sieve, sedimentation balance, photo sedimentation, Coulter counter and Microtrac. The measurement of the particle thickness by the mono-particulate film method gave a relation between the thickness and the projected diameter of mica particles classified by microsieves with a high accuracy. From this relation, the volume of the plate like mica particle was obtained and then the sphere equivalent diameter was calculated. We compared the particle size distribution based on this sphere equivalent diameter with the results measured by the other methods.

1. Introduction

It is generally accepted that a knowledge of the particle size is the most essential in powder processing. For particle size measurements, there have been a lot of publications¹⁾, reviews, and reports, and various kinds of measuring methods and equipments have been successively developed in these days.

It is unfortunate, however, that the effect of sensing principles of the equipments on measured results has been little studied. This arises from the difficulty of obtaining a suitable

expression of the particle size; for spherical or near-spherical shaped material, the size of it may be in good agreement, but for irregular material with lammellar, flaky, or acicular shape, comparison of data obtained by different equipments has been little carried out.

Computer-aided equipments which can output resultant data through printer have been widely used for particle size analysis. For these equipments, constants concerning some of the particle properties such as particle shape contained in the theoretical equations are relative values which are characterized by *standard material*; however there has been no suitable procedure developed for particles with irregular shape.

The aim of this study is to compare the particle size distributions which are obtained by several methods having different sensing principle by using a mica powder that is easy to estimate its shape irregularity.

* Matsugasaki, Sakyo-ku, Kyoto, 606
TEL. 075 (791) 3211

** 9, Shodai-tajika 1-chome, Hirakata, Osaka, 573
TEL. 0720 (57) 3721

† This report was originally printed in *J. Soc. Materials Science, Japan*, **32**, 966-970 (1983) in Japanese, before being translated into English with the permission of the editorial committee of the Soc. Materials Science, Japan.

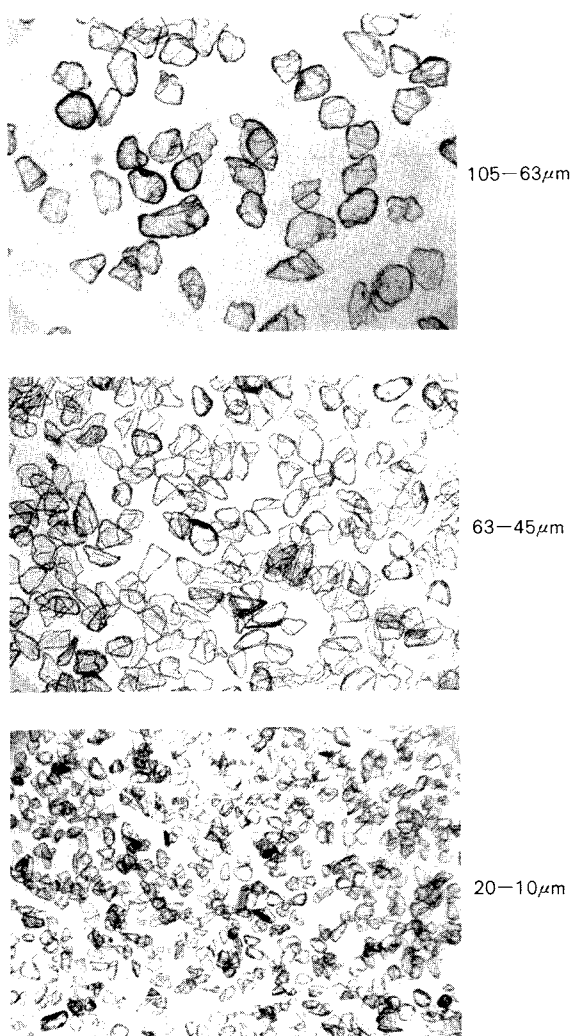


Fig. 1 Photomicrographs of classified mica particles

2. Experimental

2. 1 Sample

The material used for this work was a ground product of refined Canadian phlogopite together with synthetic mica in part, which had been separated into less than $150\ \mu\text{m}$ in advance. These particles were separated by standard sieves and precise sieves (Micro sieve) to be used as samples. Typical photomicrographs of them are shown in Fig. 1, in which the particle shape may be regarded as a hexagonal platelet similar to a crystal habit of mica.

In addition, ground calcium carbonate and colundum were used as standard particles for comparison since their shape might be considered to be almost spherical.

2. 2 Particle size analysis

The methods for determining particle size used in this work are as follows:

Sieve

A set of JIS testing sieve with woven cloth was used to separate particles larger than $105\ \mu\text{m}$. For particles smaller than $105\ \mu\text{m}$, Micro sieve manufactured by electroforming method was employed with an opening of 63, 45, 32, 20, 10, and $5\ \mu\text{m}$.

Optical microscope

Since a flaky powder like mica tends to flatly spread over a slide glass, its two-dimensional image can be obtained by optical microscope. In this work, we determined Feret's diameter which is one of the unidirectional particle size.

In addition, the individual dimensions such as length L and breadth W of 200 particles selected randomly from the separated fractions were measured to obtain the relation between elongation ratio L/W and particle size.

Sedimentation balance

For this method, a conventional procedure was employed with sodium hexametaphosphate solution of 0.2% in concentration. This method offers a diameter of sphere which falls in the medium with the same density and velocity as the particle in question. The diameter obtained in this way is well known as Stokes' diameter and its distribution is based on particle weight.

Photosedimentation

This method also adopts the same medium as that for the sedimentation balance, providing Stokes' diameter of particles. However, the particle size is dependent upon areas of the projected shadow because this method is based on the intersection of the light beam which passes perpendicularly to the settling direction of the particles in suspension.

Coulter counter

This method measures size distribution of particles suspended in an electrolyte by the presence of a fine particle in a little orifice placed between two electrodes. This size distribution is based on particle volumes because the particle size is given as a diameter of the sphere which has the same volume as that of the particle in question. The apparatus used in

this study was Coulter counter, Model TA II, which includes a microprocessor that outputs data of the particle size distribution through X-Y recorder.

Microtrac

As is well known, Fraunhofer diffraction patterns of particles take place when the monitoring zone in suspension is projected by a laser beam which is transmitted perpendicularly to the stream direction. The particle size distribution, which is based on volume of equivalent sphere, is obtainable by use of the principle that an angle distribution of its diffraction intensity is a function of particle sizes. This analyzer presents calculated results through a printer with the aid of microprocessor.

Monoparticulate film method

As reported in the literature²⁾, this method measures an average thickness of particles which are hydrophobized and dispersed so that a monoparticulate film may be formed on the water. It provides a dimension which is dependent upon the particle shape; for near-

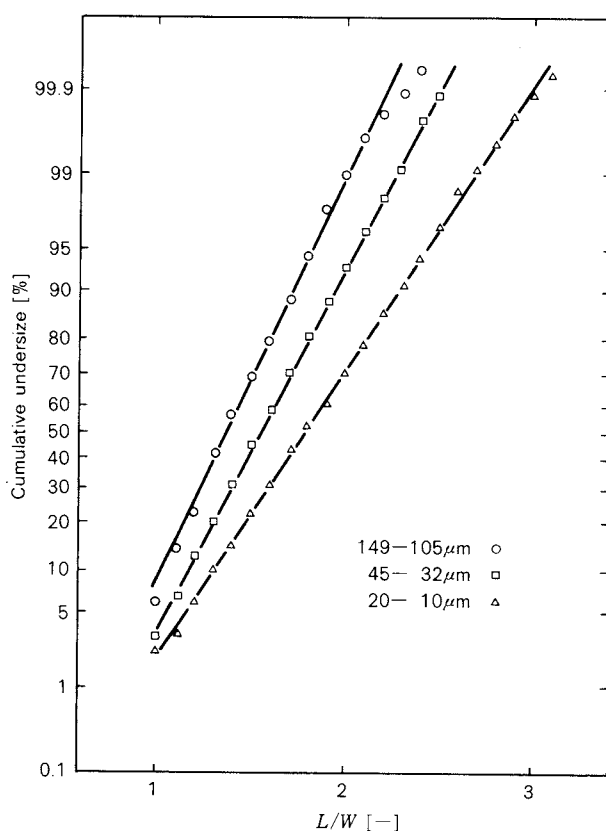


Fig. 2 Distribution of elongation ratio on mica particles

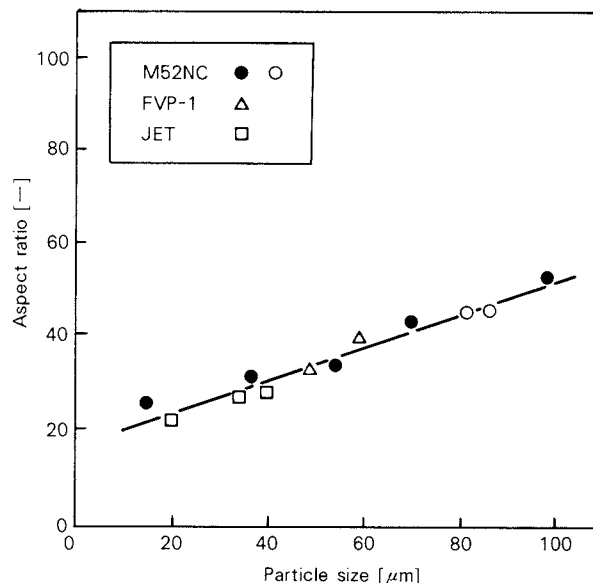


Fig. 3 Relation between the particle size and the aspect ratio (Symbols show the types of crusher.)

spherical or near-cubic materials an average size is obtainable, and for flaky-shaped materials like mica an average thickness. The method of microscope or sieve offers a plane size of particles, so the degree of relative thickness can be given by use of the ratio of plane size to thickness, namely the aspect ratio.

The detail description of the individual equipments mentioned above is to be referred in the literatures¹⁾.

3 Results and discussion

3. 1 Particle shape

Figure 2 shows typical distributions of the elongation ratio L/W obtained from the photomicrographs of the sample powder which were separated into three fractions. It was found that smaller sizes of such particles might give slenderer figures with the mean value of L/W ranging from 1.3 to 1.8.

On the other hand, the mean thickness of the sample powder was determined by the monoparticulate film method. This sample powder consisted of a ground product given by three pulverizers with different mechanism³⁾ and the fractions which were made by Micro sieve. By dividing the cumulative 50% diameter obtained by sieve by the thickness, one can get the aspect ratio. In this procedure, $\sqrt{2}$ times the sieve opening must be used for the particle size determined by sieve, because a flaky parti-

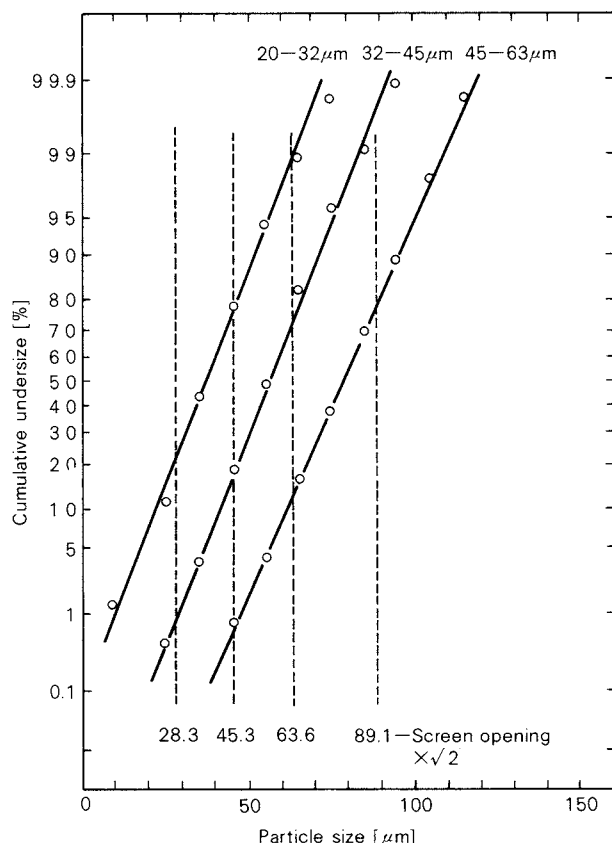


Fig. 4 Particle size distribution of classified mica by photomicrograph

cle pass diagonally through a sieve opening in square shape. As indicated in Fig. 3, plots of the aspect ratios against the cumulative 50% diameters show the linear relation expressed as

$$\text{Aspect ratio} = 0.36 D_{50} + 16 \quad (1)$$

where D_{50} represents the cumulative 50% diameter.

These results state that a particle of mica powder may become more slender and relatively thicker in its figure as its particle size decreases.

3. 2 Accuracy of Micro sieve separation

The accuracy of Micro sieve separation was evaluated as follows; the mica powder was sieved into three fractions (Sample A of 20 to 32 μm , Sample B of 32 to 45 μm , and Sample C of 45 to 63 μm). Then we determined Feret's diameters of 1000 particle images selected randomly from the photomicrograph of each fraction.

The particle size distributions obtained in this way are shown in Fig. 4. It is found that

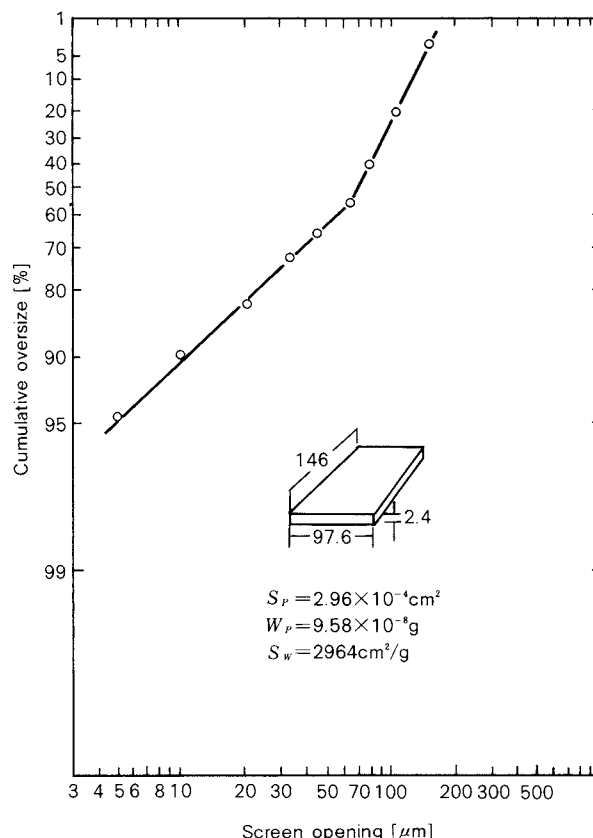


Fig. 5 Particle size distribution of mica powder by sieving

these distributions were all regular, covering 20 to 80 percent of the distribution width within the size range of $\sqrt{2}$ times the sieve opening used. This implies that a flaky particle like mica can pass diagonally through a square sieve opening as pointed out previously, despite having a considerably wide range of the elongation ratio. Thus Micro sieve was found to have sufficiently high accuracy for comparison in this work.

3. 3 Accuracy of the monoparticulate film method.

To evaluate the accuracy of the monoparticulate film method, specific surface area was determined in two ways. The material used in this work was the ground mica powder having the particle size distribution shown in Fig. 5 and the mean thickness of 2.4 μm determined by the monoparticulate film method.

One of the ways for obtaining specific surface area is to make a particular solid model which may characterize a mica particle having a platelet figure. The cumulative 50% diameter of 40 μm , as indicated in Fig. 5, was used as

a mean diameter of the particles, though it might be doubtful whether this assumption was suitable for such a broad particle size distribution or not. Using this diameter, the dimensions of the solid model were calculated as shown in Fig. 5. The breadth was considered to be $\sqrt{2}$ times the mean diameter; the length to be 1.5 times the breadth, judging from Fig. 1. With these values, the whole surface area of $2.96 \times 10^{-4} \text{ cm}^2$ and the weight of $9.58 \times 10^{-8} \text{ g}$ of the model particle were calculated, and thus the specific surface area of $2964 \text{ cm}^2/\text{g}$ could be obtained.

The other was given by calculating the volume of particles which were spread over the water to form a monoparticulate film. The area covered with the particles was $1650 \text{ cm}^2/\text{g}$, with the packing ratio of 0.9. Hence the specific surface area could be calculated to be $(1650 \times 0.9 \times 2) + 110 = 3080 \text{ cm}^2/\text{g}$, where the value 110 represents the total of the side areas.

The specific surface areas obtained in these ways were found to have fairly good agreement, and this suggests that the monoparticulate film method could be reliable for estimation of particle shape characteristics.

3. 4 Comparison of measured particle size distributions

By use of the procedures described in Section 2.2, particle size distributions of the same sample powder were determined to distinguish the difference in the expressions caused by the sensing principles. The results were compared using a sphere equivalent diameter as the same dimension and physical meaning since the particle size obtained in this work was based on the diameter of a equivalent sphere except the case of optical microscope and sieve.

Photomicrograph

As well known, a Feret diameter of projected two-dimensional micrographic images of particles has the tendency to be consistent with the arithmetic mean diameter of breadth and length when sufficiently large number of particles are counted. The mean value of the diameters may be considered to be little larger than the size which is determined by Micro

sieve. In this work, diameters of standard particles were calculated for the criterion of comparison

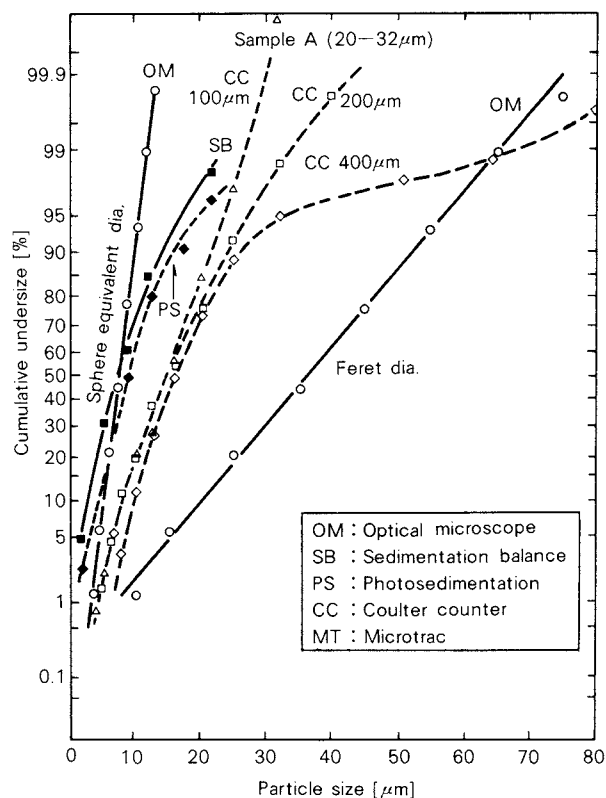


Fig. 6 Comparative data on the particle size distribution of mica A ($20 \sim 32 \mu\text{m}$) obtained by various methods

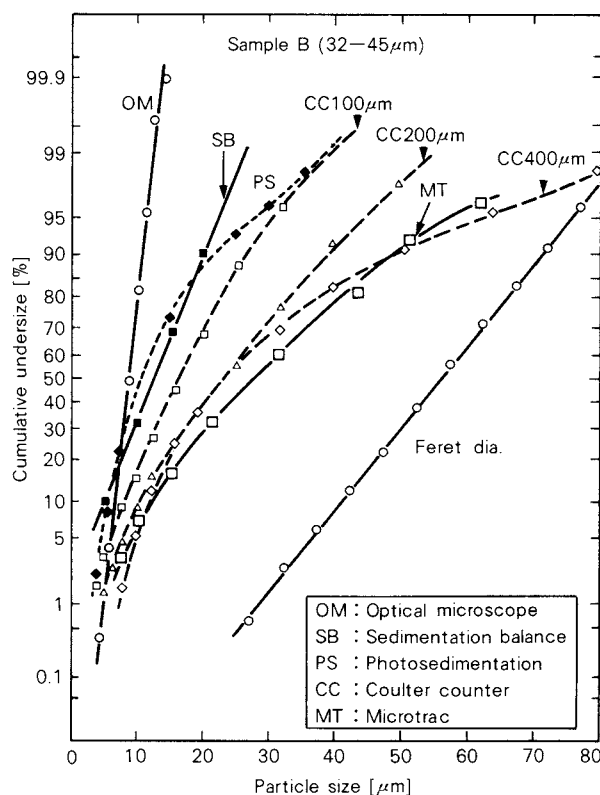


Fig. 7 Comparative data on the particle size distribution of mica B ($32 \sim 45 \mu\text{m}$) obtained by various methods

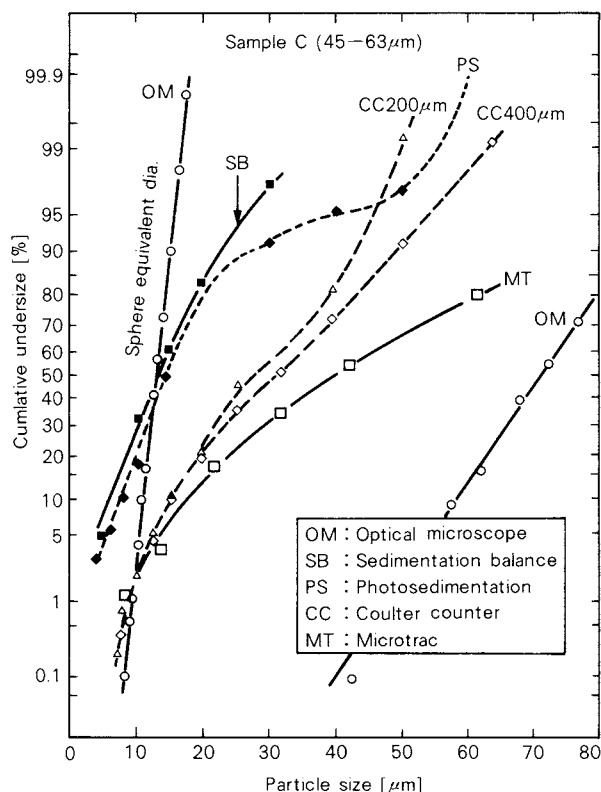


Fig. 8 Comparative data on the particle size distribution of mica C (45~63 μm) obtained by various methods

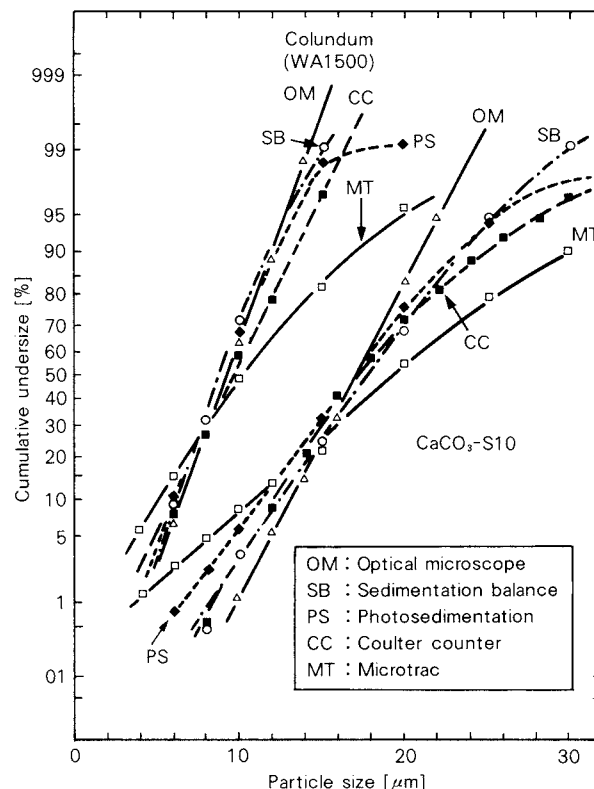


Fig. 9 Comparative data on the particle size distribution of granular shaped particles

as follows; the particle volumes of each fraction of the sample A, B, and C were obtained by using the frequency distributions of the Feret diameters with an interval range of 2 to 5 μm and the thickness calculated from Eq.(1). By considering a sphere which had the same volume as the particle in question, the required diameter was obtained. The particle size distributions of the sample are indicated in Figs. 6 to 8, together with the distributions obtained by the methods mentioned above.

Sedimentation

The particle size distributions given by sedimentation balance and photosedimentation were found to have satisfactory agreement with those of the standard particles, but the ranges of the distributions covered were relatively wide. This reason may be considered as follows; small particles in suspension have tendency to fall down in various positions in the Stokes region of particle motion. It is supposed that the falling speed might be maximum when a particle was oriented perpendicularly to the streamline owing to the minimum flow resist-

ance and, in turn, it might become minimum when the particle was oriented horizontally. Therefore the sedimentation method seemingly tends to provide a relatively wide distribution of particle sizes, even if the particles to be measured are actually monodispersed.

It should be noticed that an extraordinarily large number of particles apparently existed in the coarser side in the coarsest sample C. It is possibly because the orientation of the particles remained during the falling period since the settling depth was relatively short and the agitation flow was not negligible. This effect will be more noticeable when a particle was faced perpendicularly to the beam path.

Coulter counter

It is generally known that the values measured by Coulter counter may vary according to its aperture size. The result obtained in this work shows that a smaller diameter of the aperture might permit the particle size distribution to approach the standard distribution, as illustrated in Figs. 6 to 8, where the value in μm unit refers to a diameter of the apertures used.

The following problems should be noticed, though no sufficient discussion has been made in this work; no suitable standard material for calibration has been obtained and the value measured by this method is considerably dependent upon the magnitude of the electrical charge which does not seem to be distributed uniformly on the surface of a mica powder with two-dimensionally crystalline structure.

Microtrac

Microtrac permits liquid suspended with particles to flow down fast at the detecting zone which is placed perpendicularly to the path of a laser beam. In this case, flaky particles like mica tend to be oriented in parallel with the streamline or perpendicularly to the beam path, rotating arbitrarily around the streamline. Thus the particle size obtained in this way is larger than the Feret diameter. On the other hand, the size is smaller than the sedimentation diameter since the sedimentation methods allow the particles to settle with random attitude.

The results obtained in this work might support the tendency mentioned above, though it is not always possible because of the difference in sensing principle of the individual particle size measuring method.

As explained above, adequate comparison requires other information than geometrically equivalent diameter of a particle, unless the particle shape is fitted to the set-up condition of the equipment to be employed. This is understandable from the fact that for near-spherical particles like ground calcium carbonate or colundum, a relatively unitary particle size distribution independent of the measuring equipments could be obtained as shown in **Fig. 9**, except the case of Microtrac which would tend to provide a coarser distribution.

4. Conclusion

In this work, a mica powder with flaky shape was used to find the effect of irregular shape on its particle size distribution by use of 6 par-

ticle size measuring equipments with different sensing principles. For comparison based on the same dimension and physical meaning, the sample was sieved into several monodispersed particle fractions by precise sieve and the dimensions of the particles were determined by microscope and the monoparticulate film method. The accuracy of these methods was discussed before the particle size distribution of spheres which had the same volumes as those of the particles in question were obtained. By using these sphere equivalent diameters, the results were compared together with the distributions obtained by the other methods; for photosedimentation, the basis of a particle size was changed from area to volume.

The result of this work is that a particle size measuring equipment which is more sensitive to the orientation of irregular shape particle would give more deviation of particle size distribution from that of the standard material. This was ascertained from the comparison with the measured result of near-spherical materials.

Acknowledgement

The authors wish to express their appreciation to Development Department of Kuraray Co., Ltd. for the gift of the sample of mica.

References

- 1) The Society of Powder Technology, Japan: "Ryudo Sokutei Gijutsu (Particle size analysis)", Nikkan Kōgyō Shinbunsha (1975).
Kubo K., G. Jimbo, E. Suito, H. Takahashi and S. Hayakawa: "Funtai - Riron to Oyo (Powder - theory and application)", Maruzen (1979).
Association of Powder Process Industry and Engineering: "Funryūtai Keisoku Handdobbuk (Handbook of Measuring Powder and Particle Characterization)", Nikkan Kōgyō Shinbunsha (1981).
- 2) Nishino M. and M. Arakawa: *Journal of the Society of Materials Science, Japan*, **27**, 696 (1978).
- 3) Yokoyama T., T. Yamaguchi, M. Arakawa, S. Imoto and K. Hayashi: *Funsai (The Micromeritics)*, No. 28 36 (1984).
- 4) Arakawa M.: *Journal of the Society of Powder Technology, Japan*, **17**, 299 (1980).

Deposition of Charged Aerosol Particles Flowing through Parallel Plates[†]

Hiroaki Masuda, Shunya Ikumi
and Takashi Ito

Department of Chemical Engineering,
Hiroshima University*

Abstract

Deposition of unipolarly charged aerosol particles flowing through parallel plates has been investigated both theoretically and experimentally. The equation of motion for the particles was solved numerically in consideration of the Coulomb force, image force, particle-inertia force, and fluid-velocity profile. Then the deposition efficiency was calculated based on the limiting trajectories of the particles.

It was found that the calculated deposition efficiency, assuming a laminar flow, was a little smaller than the corresponding analytical solution obtained for the plug flow distribution. It was also found that the effect of the image force and particle-inertia force was negligible in the experimental range. The experimental deposition efficiencies for charged fly-ash particles were well explained in so far as the actual velocity distributions were taken into consideration.

1. Introduction

The deposition of charged aerosol particles suspended in the air flow is enhanced by the effect of electric field caused by the particles themselves. This effect, called the space-charge effect, may be applicable to practical use such as dust collection. The reduction of the collection efficiency due to back discharge in an electrostatic precipitator has become a serious problem in recent years. This problem may be successfully solved and the collection efficiency will become predictable to considerable extent when the dust particles are precharged and then captured with the aid of the space-charge effect.

The deposition of monodispersed, charged particles on the circular tube due to the space-charge effect has been studied analytically by Wilson¹⁰⁾ and experimentally by Kasper⁶⁾,

Adachi et al.¹⁾, and the author et al.⁷⁾ These experimental results are found to have reasonable agreement with the analytical solution derived by Wilson. Adachi et al. have also studied the effect of image force. For the deposition of charged aerosol particles in parallel channel flow, the effects of space charge and thermal diffusion have been studied by Ingham⁵⁾ and Chen²⁾, the effect of image force by Yu et al.^{11,12)}, and the studies on the gravity effect has been reported elsewhere^{3,9)}. Unfortunately, however, there have been a very few reports which analyze these problems synthetically.

In this paper, the deposition efficiency of unipolarly charged aerosol particles flowing in a parallel channel was theoretically determined based on the critical particle trajectory, which is obtained through numerical integration of the equation of motion for the particles. In the numerical calculation, the effects of space charge, image force, particle-inertia force, and air-velocity profile were taken into considerations. Further, the deposition of unipolarly charged fly-ash particles was experimentally investigated, and the results were compared with the theoretical predictions.

* Shitami, Saijo, Higashi-Hiroshima, Hiroshima, 724
TEL. 0824 (22) 7111

† This report was originally printed in *J. Soc. Powder Tech., Japan*, 20, 670-676 (1983) in Japanese, before being translated in English with the permission of the editorial committee of the Soc. Powder Tech., Japan.

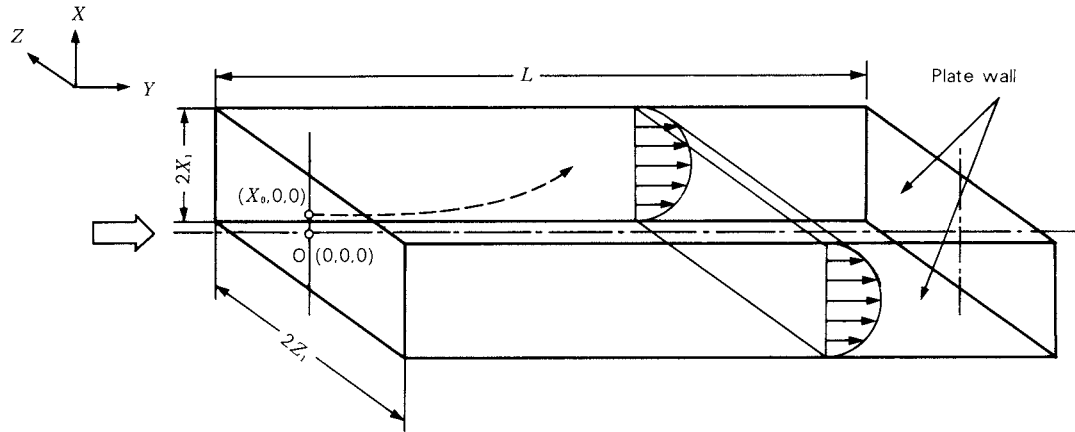


Fig. 1 Adopted coordinates in the calculation of particle trajectories

2. Theory

Assuming a plug flow, a parallel plate model of L in length, $2Z_1$ in width, and $2X_1$ in space between the plates is considered with the coordinate system illustrated in Fig. 1. When unipolarly charged aerosol particles flow into the model channel, the X -component of the intensity of electric field at the position X_o is given by the following equation:

$$E = N_o q X_o / \epsilon_o \quad (1)$$

where N_o is the particle number per unit space volume, q is the electric charge on a particle and ϵ_o is the air permittivity. The Y - and Z -components of the electrostatic field are negligible in the following analysis. Also, the electric force on a particle is given by

$$F_e = q E = N_o q^2 X_o / \epsilon_o \quad (2)$$

If the particles are assumed to be monodisperse, the Coulomb force F_e on a particle is unchanged throughout the movement. For this case, X -component of the particle velocity is determined by the force balance between the force F_e and the fluid resistance given by the Stokes law, as follows:

$$v = \frac{F_e C}{3\pi\mu D_p} = \frac{N_o q^2 C X_o}{3\pi\mu D_p \epsilon_o} = \alpha X_o \quad (3)$$

The parameter α in Eq. (3) is defined by the following equation:

$$\alpha = \frac{N_o q^2 C}{3\pi\mu D_p \epsilon_o} \quad (4)$$

where μ is the air viscosity, D_p is the particle

diameter and C is the Cunningham's slip correction factor. Thus the displacement of a particle in the X -direction is

$$dX = v dt = \alpha X_o dt \quad (5)$$

By integrating Eq. (5),

$$X_1 - X_o = \alpha X_o \tau \quad (5-a)$$

where τ is the average residence time. The deposition efficiency η is defined as

$$\eta = (X_1 - X_o) / X_1 = \alpha \tau / (1 + \alpha \tau) \quad (6)$$

By use of the following definitions:

$$N_o = c_o / m_p, \hat{q} = q / m_p, \tau = L / \bar{U}_y,$$

$$\text{and } m_p = \frac{\pi}{6} D_p^3 \rho_p$$

Hence Eq. (6) is rewritten as follows:

$$\eta = \frac{\hat{q}^2 D_p^2 \rho_p c_o L C}{18\mu \bar{U}_y \epsilon_o} \quad (7)$$

where c_o is the mass concentration of the particles, m_p is the particle mass, \hat{q} is the electric charge on a unit mass of the particles, \bar{U}_y is the average air velocity, and ρ_p is the particle density.

Although the particles are assumed to move along the plate (in the Y -direction) with the average air flow velocity, the effect of the actual velocity profile should be taken into consideration in a practical use. In addition, the inertia force and the image force should also be considered for relatively coarser parti-

cles and for low particle concentration, respectively.

Assuming that inlet air flow is fully developed so as to form a laminar velocity profile and the gravity effect is negligible, the equations of motion for particles are:

for X -component

$$\frac{\pi}{6} D_p^3 \rho_p \frac{d^2 X}{dT^2} = F_e + F_i + \frac{3\pi\mu D_p}{C} (U_x - \frac{dX}{dT}) \quad (8)$$

for Y -component

$$\frac{\pi}{6} D_p^3 \rho_p \frac{d^2 Y}{dT^2} = \frac{3\pi\mu D_p}{C} (U_y - \frac{dY}{dT}) \quad (9)$$

where F_e is the Coulomb-force given by Eq. (2) and F_i is the image force given by the following equation:

$$F_i = \frac{q^2 X_1}{4\pi\epsilon_o} \left[\frac{X}{(X_1^2 - X^2)^2} + \sum_{n=1}^{\infty} \frac{(2n+1)X}{\{(2n+1)X_1^2 - X^2\}^2} \right] \quad (10)$$

If the air flow is assumed to be laminar, the air flow velocity is expressed as

for X -component

$$U_x = 0 \quad (11)$$

for Y -component

$$U_y = \frac{3}{2} \bar{U}_y \left\{ 1 - \left(\frac{X}{X_1} \right)^2 \right\} \quad (12)$$

By substituting Eqs. (11) and (12) into Eqs. (8) and (9) respectively, the following non-dimensional equations will be obtained;

$$P \frac{d^2 x}{dt^2} = \frac{C(F_e + F_i)}{3\pi\mu D_p \bar{U}_y} - \frac{dx}{dt} \quad (13)$$

$$P \frac{d^2 y}{dt^2} = \frac{3}{2} (1 - x^2) - \frac{dy}{dt} \quad (14)$$

where $x = X/X_1$, $y = Y/X_1$ and $t = \bar{U}_y T/X_1$. The particle-inertia parameter P is defined as

$$P = \frac{D_p^2 \rho_p \bar{U}_y C}{18\mu X_1} \quad (15)$$

The Coulomb-force parameter K_e and the image-force parameter K_i may be defined by the following non-dimensional forms;

$$K_e = \frac{N_o q^2 X_1 C}{3\pi\mu D_p \bar{U}_y \epsilon_o} \quad (16)$$

$$K_i = \frac{q^2 C}{12\pi^2 \mu D_p \bar{U}_y \epsilon_o X_1^2} \quad (17)$$

Using the above parameters, Eq. (13) is rewritten in non-dimensional form as follows:

$$P \frac{d^2 x}{dt^2} = K_e x_o + K_i \left[\frac{x}{(1-x^2)} + \sum_{n=1}^{\infty} \frac{(2n+1)x}{\{(2n+1)^2 - x^2\}^2} \right] - \frac{dx}{dt} \quad (18)$$

The numerical integration of Eqs. (14) and (18) in combination yields the particle trajectories. Considering the particle which travels from the initial point X_o to the boundary point ($X = X_1$) at the outlet of the parallel channel ($Y = L$), the deposition efficiency can be determined by the following equation;

$$\eta = \frac{\int_{x_o}^1 u_y dx}{\int_0^1 u_y dx} = 1 - \frac{3}{2} x_o + \frac{1}{2} x_o^3 \quad (19)$$

where $u_y = U_y/\bar{U}_y$.

In this study, the numerical integration based on the Runge-Kutta-Merson method was applied to Eqs. (14) and (18) for various initial conditions in order to obtain the deposition efficiency by use of Eq. (19).

Equations (14) and (18) show that the deposition efficiency η is a function of P , K_e , K_i , L , and X_1 . **Figure 2** shows a typical set of correlations between η and K_e when $K_i = 0$ and $L/X_1 = 100$. All the curves using the parameter P indicate that η increases with an increase in K_e , approaching the dotted line as P decreases. This dotted line represents the

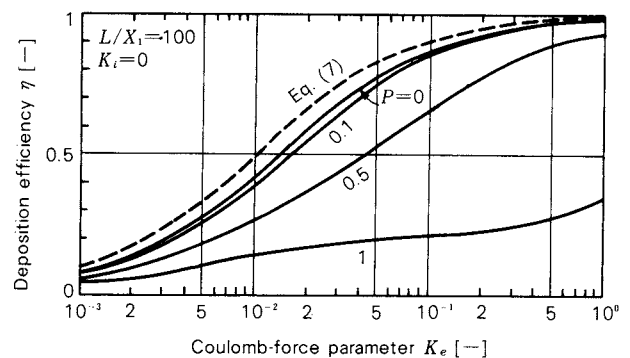


Fig. 2 Effect of inertia parameter P on the deposition efficiency (as a function of Coulomb-force parameter K_e)

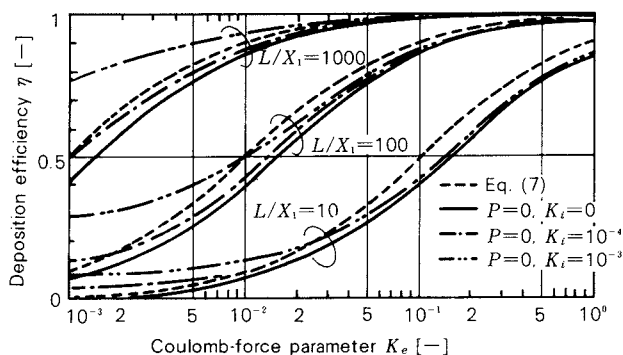


Fig. 3 Effect of image force parameter K_i on the deposition efficiency (as a function of Coulomb-force parameter K_e)

analytical solution derived from Eq. (7) based on the assumption of plug flow. The influence of particle inertia becomes dominant when $P > 0.1$ and the slope decreases as P increases.

The effect of image force on deposition efficiencies for $P=0$ is shown in Fig. 3 by use of the parameters of K_i and L/X_1 . Figure 3 employs the same coordinate system as that of Fig. 2 and the dotted line also represents a solution for plug flow. Although η increases with increasing K_i , the influence of image force is reduced as K_e increases; such an influence may be almost negligible when $K_e > 0.1$. The effect on deposition due to image force is enhanced as L/X_1 increases; in other words, when the plates are made longer or the clearance between the plates narrower.

By dividing Eq. (16) by Eq. (17), the ratio of the image force parameter K_i to Coulomb-force parameter K_e is expressed as

$$\frac{K_i}{K_e} = \frac{1}{4\pi N_o X_1^3} \quad (20)$$

Figure 4 shows the ratio $\eta/\eta_{K_i=0}$ as a function of K_e with the ratio K_i/K_e as a parameter under the conditions of $P=0$ and $L/X_1 = 100$, where $\eta_{K_i=0}$ represents the deposition efficiency for $K_i = 0$. The ratio $\eta/\eta_{K_i=0}$ increases with increasing the ratio K_i/K_e . This means that the influence of image force may be conspicuous with decreasing the particle number concentration and/or the space between the plates in consideration of Eq. (20).

3. Experiment

3-1 Experimental apparatus and method

The outline of the experimental arrangement

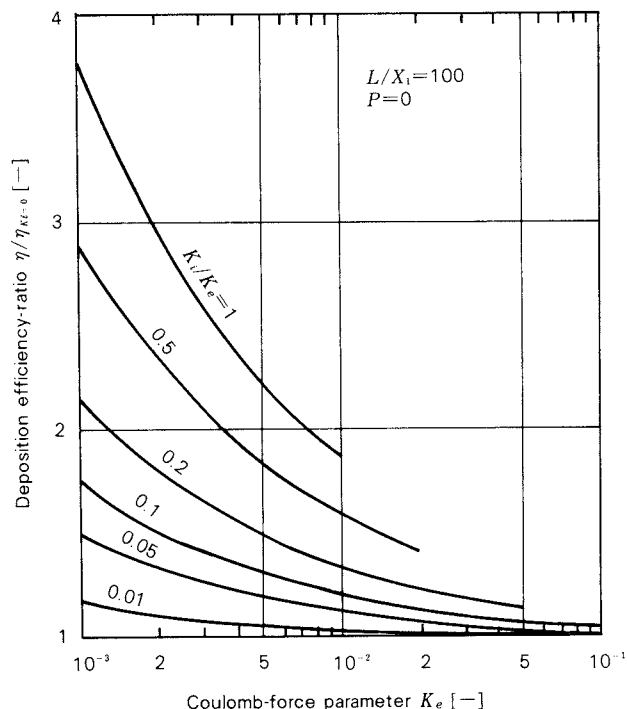


Fig. 4 Deposition efficiency-ratio $\eta/\eta_{K_i=0}$ as a function of K_i/K_e

is illustrated in Fig. 5. The powder material used for this work was JIS test dust No. 10 of fly ash with the density of 2.39 g/cm^3 and the mass median diameter of $3.5 \mu\text{m}$ having the geometrical standard deviation of 2.18 (JIS Z-8901). After dispersed with a mixer-type disperser (made by Shimadzu Seisakusho Ltd.) at a constant feed rate with a table feeder (made by Sankyo Dengyo Co., Ltd.), the sample powder was unipolarly charged with the Boxer charger (made by Sankyo Dengyo Co., Ltd.), before being introduced into the test zone. Some of the sample particles were deposited on the test plates and the others which passed through them were captured with a glass fiber filter (made by Toyo Roshi Co., Ltd.). The deposition efficiency was given by

$$\eta = (W_1 - W_2)/W_1 \quad (21)$$

where W_1 is the weight of the sample discharged out of the table feeder and W_2 is the weight of it captured with the filter. It was observed that there was no adhesion of particles on the disperser wall and the deposition except for test plates was negligible (which was less than 3% of the total captured amount). The feeding rate of the table feeder fluctuated to some extent; the variation was about 5%

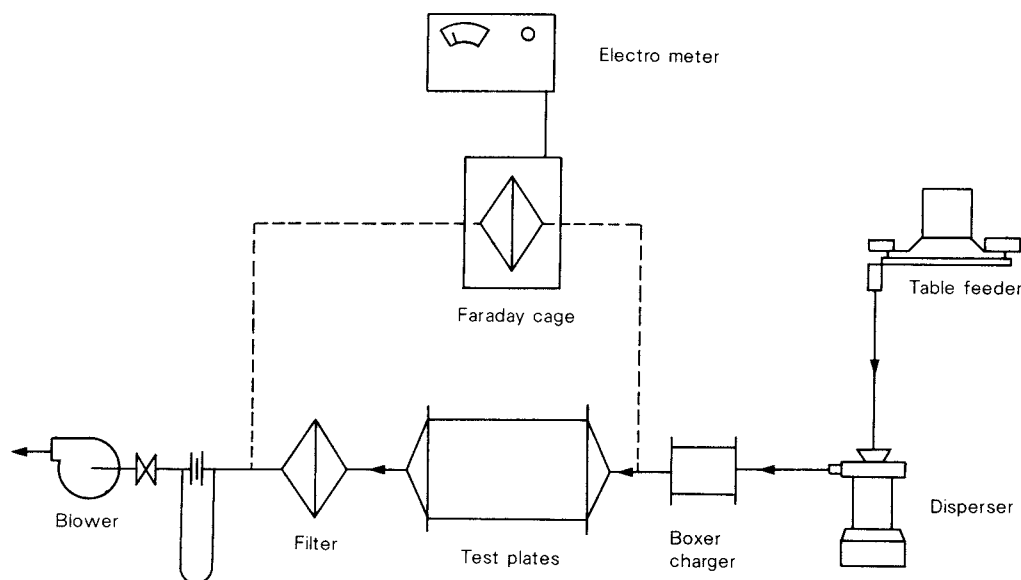


Fig. 5 Schematic diagram of the experimental arrangement

during 1 min operation with a range of 10 to 400 mg/s.

Figure 6 shows the outlook of the test plates with 39 cm height, 18 cm width, and 1 m length in which several steel plates were arranged in parallel and mounted with PVC hold-

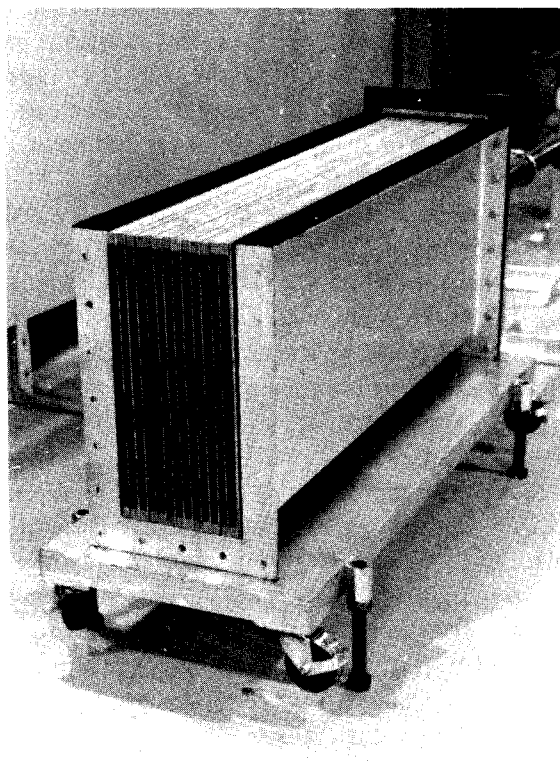


Fig. 6 Photograph of test plates (upper and connection parts are dismounted)

ing spacers on top and bottom sides. The space between each test plate was to be varied with the spacer thickness. The flow after the charging zone was enlarged toward the deposition zone and the disk of 4 cm diameter with the attitude perpendicular to the air flow was mounted at the center of the enlarged duct.

Electric charges on aerosol particles were measured with a Faraday cage and an electric meter (made by Takeda Riken Co., Ltd.) as illustrated by the dotted line in Fig. 5. In addition, the size distribution of aerosol particles was determined with a cascade impactor (made by Nippon Kagaku Kogyo Co., Ltd.).

3. 2 Experimental results and discussion

The particle inertia parameter P and the image force parameter K_i were observed to be up to 10^{-2} and 10^{-6} , respectively. Thus, the effects of such parameters would be negligible in the numerical calculation. When it is assumed that $P = 0$ and $K_i = 0$, K_e multiplied by L/X_1 gives the following new parameter $\alpha\tau$ which is independent of the space between the plates.

$$K_e \frac{L}{X_1} = \frac{\dot{q}^2 D_p^2 \rho_p c_o LC}{18\mu \bar{U}_y \epsilon_o} = \alpha\tau \quad (22)$$

The relationship between $\alpha\tau$ and η is shown in Fig. 7 where the dotted line represents the

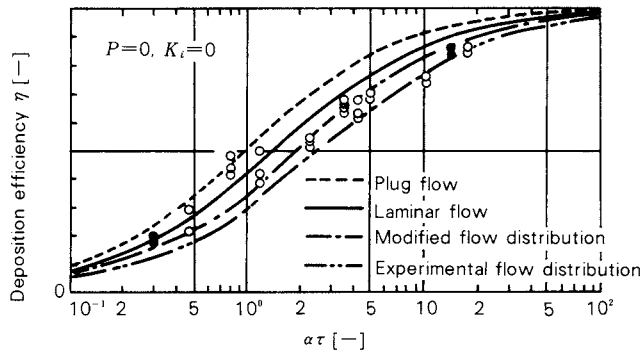


Fig. 7 Comparison between calculated and experimental deposition efficiency (as a function of parameter $\alpha\tau$)

analytical solution for plug flow and the solid line represents a calculated result for laminar flow. The deposition efficiency increases with $\alpha\tau$ and the experimental results are somewhat smaller than the solid line as $\alpha\tau > 1$.

It has been recognized from the laboratory deposition experiment that the deposition efficiency may depend upon the plate material. In this work, we employed aluminum as well as PVC to examine the spacer effect. The result suggests the effect of the spacer material would be negligible as shown in Fig. 7 where the symbol \bullet represents the measured value which was obtained by use of aluminum spacers.

It should be noticed that the actual velocity distribution of air flow would differ from the assumed one such as laminar or plug flow discussed above because of a lack of flow uniformity caused by the duct enlargement.

One of the velocity profiles at the inlet of the test plates measured by a wire anemometer is typically illustrated in Fig. 8. This figure, which is based on the non-dimensionalized coordinate system that corresponds to each inlet section in Figs. 1 and 6, implies that the flow velocity might be maximized at the center and the backward flow due to flow separation might take place near the wall. These phenomena are caused by the influence of duct enlargement, and they should be taken into consideration in a practical use.

The deposition efficiencies obtained from the modified flow distribution and the experimental flow distribution based on the actual profile indicated in Fig. 8 are also shown in Fig. 7. The latter curve provides a lower limit of the deposition efficiency because the flow development in the test plates may gradually

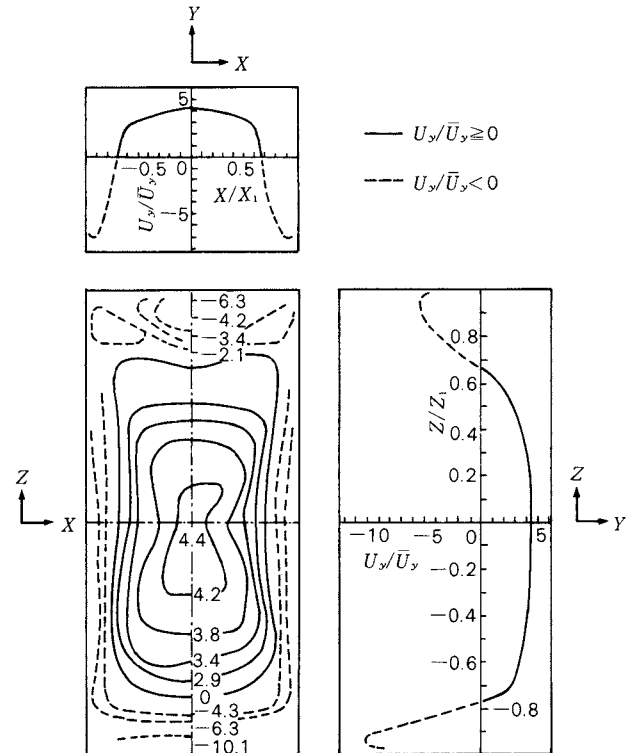


Fig. 8 Experimental profile of flow velocities at the inlet of test plates

form a laminar velocity profile. The experimental results are found within the range of the theoretical predictions, and thus the influence of the actual flow distribution may possibly justify the deviation of the experimental results from the theoretical solutions.

The experimental relationship between deposition efficiency and plate space $2X_1$ at $\alpha\tau = 4.2$ is shown in Fig. 9, where the solid line represents a theoretical solution based on the assumption of the laminar flow. The deposition efficiency was found to be independent of the plate space except that $2X_1 = 1.2$ cm. The deposition efficiency at $2X_1 = 1.2$ cm is close to the theoretical solution, and this agreement might result from the flow rectification effect of the parallel plates.

It is well-known that electric discharge takes place in atmosphere when the electric field of more than 30kV/cm is applied. If this discharge occurs between the aerosol particles and the channel wall, the deposition efficiency may be reduced because of immediate disappearance of the electrostatic force on the particle. The intensity of electric field formed by charged particles in the channel is given by Eq. (1) when the space charge density is held constant

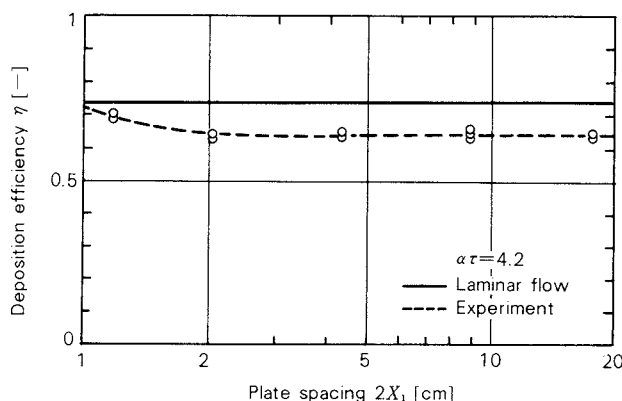


Fig. 9 Experimental relationship between deposition efficiency and the spacing of plates

at the inlet. This intensity increases to the maximum value very near the wall, and thus its maximum value will be in proportion to the plate space. In this work, this intensity was found to be up to 10kV/cm when no steel plates were inserted (in other words, only the outer case of the test box shown in Fig. 6 was used). Although it was ascertained that this intensity was smaller than the critical value for initiating atmospheric discharge, experimental studies were carried out on the distributions of particle charge and particle concentration of charged aerosols at the inlet of the test plates by use of a Faraday cage.

The particle charge distributions at the inlet of the channel along the X (width) and Z (height) directions are shown in Figs. 10 (a)

and (b) respectively. The symbols \circ and Δ in the figure denote the sampling in forward and in backward directions, respectively. With the sampling in each direction for the region where flow separation took place, it was found that the particle charge distribution in the chamber was nearly uniform. Consequently, it is reasonably considered that no electric discharge between particles and a wall of the equipment might take place.

Figures 11 (a) and (b) indicate the distributions of particle concentration in X and Z directions, respectively. The curve represents the velocity profile at the inlet of the parallel plate chamber. Although the particle concentration slightly increased near the wall, the correlation between particle concentration and velocity profile was not found.

It this work, the influences of deposition by gravity and by diffusion calculated from the equation derived by Marcus⁸⁾ were found to be up to 1% and up to 0.01%, respectively, showing that the influences might be reasonably neglected.

4. Conclusion

The deposition of unipolarly charged aerosol particles flowing through parallel plates were investigated both theoretically and experimentally.

Summarizing the results of this work:

(1) The deposition efficiency increased with

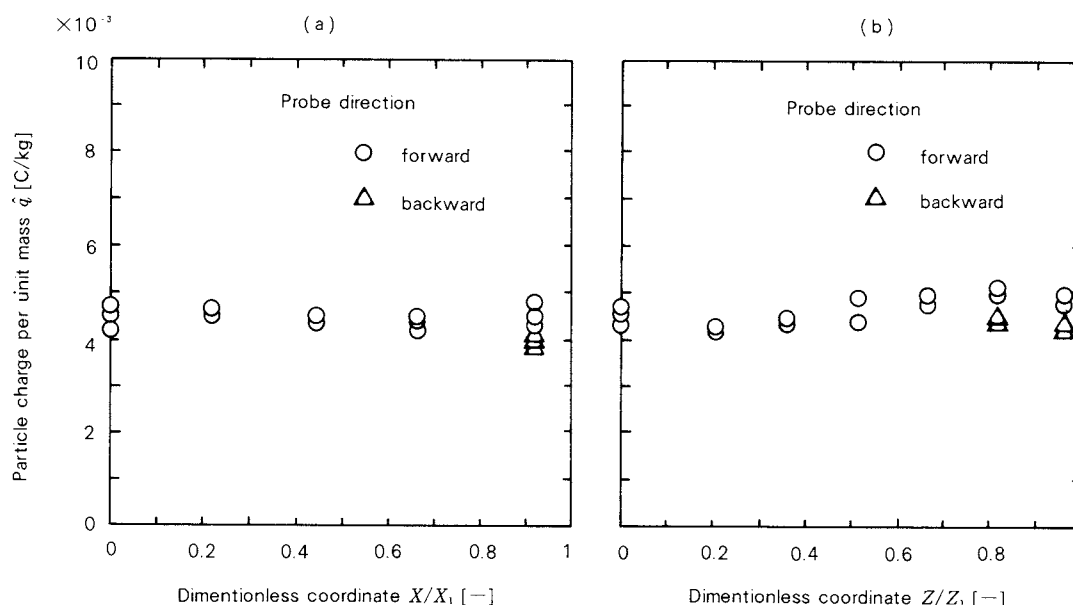


Fig. 10 Experimental results on the specific charge of particles (at the inlet of test plates)

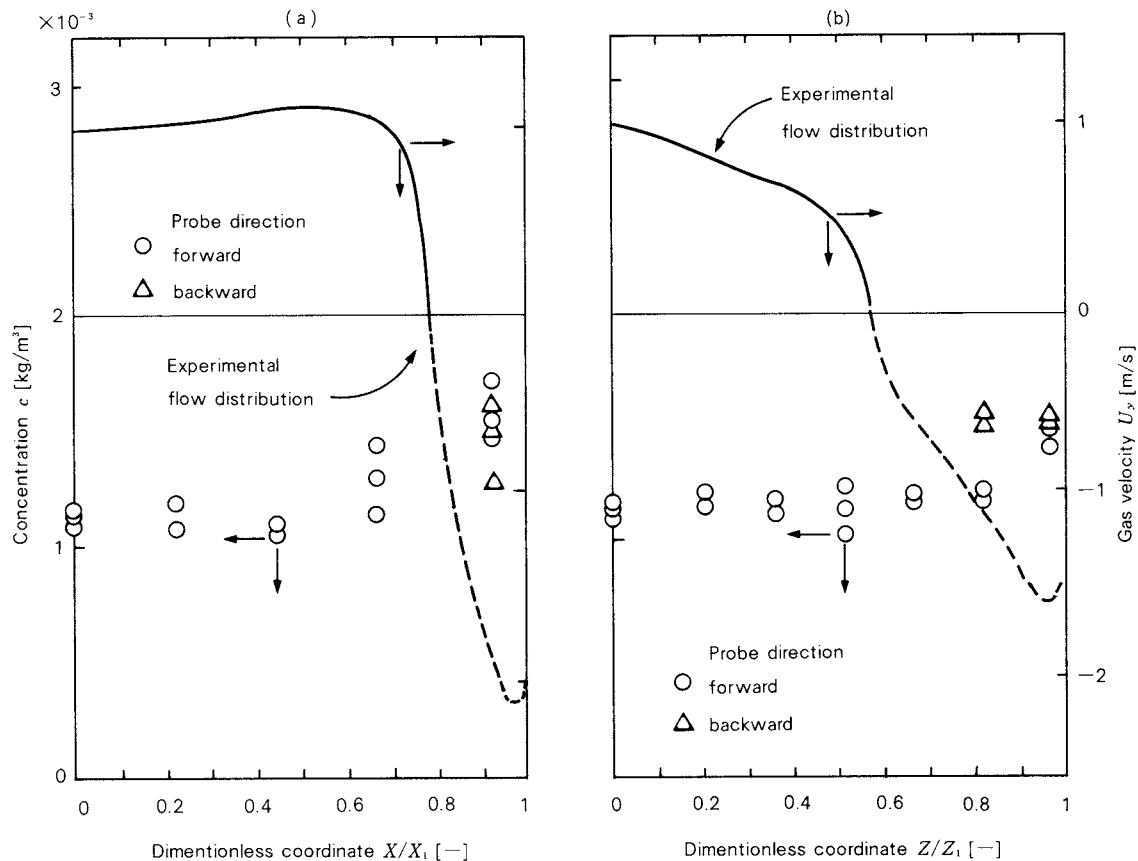


Fig. 11 Experimental distributions of the particle concentration (at the inlet of test plates)

increasing the Coumb-force parameter and the theoretical solution based on the assumption of laminar flow was slightly smaller than that for plug flow. When the image force and particle-inertia force were negligibly small, the deposition efficiency was expressed as a function of the unique parameter $\alpha\tau$ which did not depend on the space between the parallel plates.

- (2) The deposition efficiency decreased with an increase in particle-inertia parameter P . The influence of the inertia was, however, reasonably negligible if P was less than 0.1.
- (3) The image force affects the deposition efficiency when the image-force parameter is larger than 10^{-4} and the Coulomb-force parameter was smaller than 10^{-1} . The effect becomes large with increasing L/X_1 . It should be noted that the image force could be dominant when the particle number concentration and the plate space were very small.

- (4) The experimental deposition efficiency was slightly smaller than the theoretical one obtained by the assumption of laminar flow. This fact could be explained to some extent by considering the actual flow distribution.
- (5) The distributions of particle concentration and particle charge were found to be nearly uniform, and the electric discharge was not observed.

Nomenclature

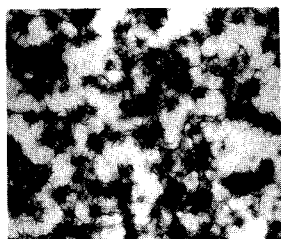
C	Cunningham's slip correction factor	[-]
c_o	particle mass concentration	[kg/m ³]
D_p	particle diameter	[m]
E	intensity of electric field	[V/m]
F_e	Coulomb-force on a particle	[kg·m/s ²]
F_i	image force on a particle	[kg·m/s ²]
K_e	Coulomb-force parameter	[-]
K_i	image-force parameter	[-]
L	plate length	[m]
m_p	particle mass	[kg]
N_o	particle number concentration	[1/m ³]
P	particle inertia parameter	[-]
q	electric charge on a particle	[C]

\hat{q} : electric charge on unit mass of particles	[C/kg]
T : time	[s]
t : non-dimensional time ($=\bar{U}_y T/X_1$)	[-]
U_x : air flow velocity in X direction	[m/s]
U_y : air flow velocity in Y direction	[m/s]
\bar{U}_y : average air flow velocity in Y direction	[m/s]
u_y : non-dimensional air flow velocity in Y direction	[-]
v : particle velocity in X direction	[m/s]
W_1 : total mass of sample	[kg]
W_2 : particle mass captured by filter	[kg]
X : coordinate perpendicular to plate	[m]
X_o : initial position of particle in X coordinate	[m]
X_1 : half distance of space between plates	[m]
x : non-dimensional X coordinate ($=X/X_1$)	[-]
x_o : initial position of particle in x coordinate (non-dimensional)	[-]
Y : coordinate in flow direction	[m]
y : non-dimensional Y coordinate ($=Y/X_1$)	[-]
Z : coordinate perpendicular to X and Y directions	[m]
Z_1 : half of plate width	[m]
ϵ_o : air permittivity	[F/m]
η : deposition efficiency	[-]

μ : air viscosity	[kg/m·s]
ρ_p : particle density	[kg/m ³]
τ : average residence time	[s]

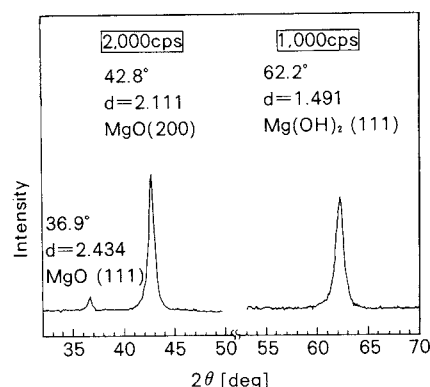
References

- 1) Adachi, M., K. Okuyama, Y. Kousaka and N. Kida: Preprints of The 15th Autumn Meeting of The Soc. of Chem. Engrs., Japan, p. 37 (1981).
- 2) Chen, R.T.: *J. Aerosol Sci.*, **9**, 253 (1978).
- 3) Chen, R.Y. and M.W. Gelber: *Powder Technol.*, **28**, 229 (1981).
- 4) Fujimoto, B.: "Ryutai Rikigaku (Fluid dynamics)" p. 193 Yokendo (1980).
- 5) Ingham, D.B.: *J. Aerosol Sci.*, **11**, 517 (1980).
- 6) Kasper, G.: *J. Colloid Interface Sci.*, **81**, 32 (1981).
- 7) Masuda, H. and S. Ikumi: *J. Soc. Powder Technol., Japan*, **18**, 867 (1981).
- 8) Takahashi, K.: "Kaicho Kiso Earozoru Kougaku (Fundamental Aerosol Technology, revised edition)", p. 51 Yokendo (1982).
- 9) Thiagarajan, V. and C.P. Yu: *J. Aerosol Sci.*, **10**, 405 (1979).
- 10) Wilson, I.B.: *J. Colloid Sci.*, **2**, 271 (1947).
- 11) Yu, C.P.: *J. Aerosol Sci.*, **8**, 237 (1977).
- 12) Yu, C.P. and K. Chanda: *ibid.*, **9**, 175 (1978).



Explanation of the cover photograph

The cover photograph (by TEM) shows very fine particles of magnesium oxide (MgO) with the magnitude of 10000X. When ground down to sub-micron size, this material becomes highly active on the particle surfaces, although it is relatively stable before grinding from the chemical point of view. Brought into contact with water in the air, it is rapidly turned into magnesium hydroxide (Mg(OH)₂) with an acicular shape, as shown in the photograph. The X-ray diffraction chart on the right verifies such a reaction.



Relationships between Particle Size and Fracture Energy for Single Particle Crushing[†]

Yoshiteru Kanda

*Department of Chemical Engineering,
Yamagata University**

Shigeru Sano

*Ichinoseki Technical College***

Fumio Saito

*Department of Chemical Engineering,
Yokohama National University****

Saburo Yashima

*Research Institute of Mineral Dressing and Metallurgy,
Tohoku University*****

Abstract

An experimental study of single-particle crushing at slow compression rate was carried out for two kinds of glassy and five kinds of natural materials. The specimens were almost spherical particles of 0.5 to 3.0 cm in diameter.

The relationships between particle size and fracture energy (strain energy) were calculated by using the results of the size effect ranging from about 10 cm to 0.0030 cm of single particle crushing, as shown in the previous papers. The experimental results are summarized as follows:

- 1) The fracture energies obtained were larger than the values calculated from the theoretical equations for limestone, marble and gypsum.*
- 2) For natural materials, the specific fracture energies rapidly increased with decreasing particle size within the range of particle size smaller than about 500 μm .*

Introduction

The importance of fracture characteristics in determining optimum design or operating condition in comminution process has been extensively recognized in various industries. The energy required for grinding materials or the grinding resistance is generally expressed as a function of particle size through size reduction. As well accepted, however, prolonged comminution has the tendency to show the finite limit of size reduction peculiar to the equipment used⁶⁾. This is not only due to the absorption of the energy into powder bed and the reduction of energy distribution for each fractured fragment, but also due to the increase in fracture strength resulted from size reduc-

tion, that is, the effect of size on strength.

In the present paper, the relationship between compressive strength of spherical specimens of 0.5 to 3 cm in nominal diameter and fracture energy was experimentally investigated. Furthermore, the energy required for single particle crushing and the specific fracture energy was calculated by use of the experimentally obtained relationship between compressive strength of spheres with an approximate diameter range of 30 μm to 10 cm presented in the literatures^{10,13)}. The result produced was that specific fracture energy in-

[†] This report was originally printed in *Kagaku Kogaku Ronbun-shu*, 10, 108-112 (1984) in Japanese, before being translated into English with the permission of the editorial committee of the Soc. Chemical Engineers, Japan.

* Jonan 4-3-16, Yonezawa, Yamagata, 992
TEL. 0238 (22) 5181

** Hagisho-takanashi, Ichinoseki, Iwate, 021
TEL. 0191 (24) 2121

*** Tokiwadai Hodogaya-ku, Yokohama, Kanagawa, 240
TEL. 045 (335) 1451

**** Katahira 2-1-1, Sendai, Miyagi, 980
TEL. 0222 (27) 6200

creased with increasing particle size, showing a remarkable rise especially within the finer range of the particle size.

The experimental or calculated results obtained in this work were based on the condition where spherical or near-spherical specimens were fractured under static compressive load⁹⁾. However, the actual fracture is accompanied by the phenomenon that irregularly shaped particles are fractured under dynamic or impact load. Therefore the results of this paper will be available in practice as far as the difference between the ideal and actual phenomenon is taken into consideration to reasonable extent.

1. Sample and experimental method

The specimens used and their mechanical properties are listed in Table 1. The relationship between compressive strength of spheres and fracture energy is studied by experiment and calculation by use of the nominal diameter and number of specimens^{*} prepared as indi-

Table 1 Properties of samples

Samples	ρ [kg/m ³]	Y [Pa]	ν [-]	W_f [kWh/t]
Quartz glass	2.20×10^3	7.35×10^{10}	0.16	14.8
Borosilicate glass	2.33×10^3	6.12×10^{10}	0.21	15.2
Quartz	2.62×10^3	8.71×10^{10}	0.16	13.3
Feldspar	2.55×10^3	5.87×10^{10}	0.26	12.4
Limestone	2.70×10^3	6.80×10^{10}	0.32	9.4
Marble	2.70×10^3	5.34×10^{10}	0.30	6.7
Gypsum	2.30×10^3	3.78×10^{10}	0.32	6.3

Table 2 Nominal diameter and number of specimens prepared

Samples	Nominal diameter [cm]					
	0.5	1.0	1.5	2.0	2.5	3.0
Quartz glass	20	20	20	20	20	—
Borosilicate glass	20	20	20	20	20	20
Quartz	20	20	20	20	20	—
Feldspar	—	20	20	20	20	—
Limestone	20	20	20	20	—	—
Marble	20	20	20	20	—	—
Gypsum	—	20	20	20	20	—

^{*} Yamaguchi⁹⁾ reported that 20 specimens must be required for one point to obtain the confidence limit up to 95% by use of granite. Our study is for the time being is based on his results which might depend on the material kind.

cated in Table 2. Fracture experiments were carried out with Simadzu universal testing machine, Model REH-30, to obtain load-displacement variation which was presented on an X-Y recorder through differential transducer. The manufacturing procedure and its accuracy of the specimens, and the experimental method were fully described in the literatures^{3,9)}.

2. Calculation of fracture energy

When the sphere of x in diameter is compressed between parallel plates as shown in Fig. 1, the elastic theory provides the displacement Δ as a function of the load P as follows:

$$\Delta = 2 \left\{ \frac{9}{16} \cdot \frac{1}{x} \cdot \left(\frac{1-\nu^2}{Y} \right)^2 \cdot P^2 \right\}^{\frac{1}{3}} \quad (1)$$

where ν is Poisson's ratio and Y is Young's modulus. For an overall or net energy for fracture, various definitions have been proposed^{4,5)}, though the final concept has been never obtained yet. In this paper, the term *energy* required for fracture is defined as elastic strain energy accumulated in a particle until the fracture will take place. That is:

$$E = \int P d(\Delta) = 0.832 \left(\frac{1-\nu^2}{Y} \right)^{\frac{2}{3}} x^{-\frac{1}{3}} P^{\frac{5}{3}} \quad (2)$$

Accordingly, the fracture energy per unit mass E/M is given by

$$\frac{E}{M} = 4.99 \frac{1}{\pi \rho} \left(\frac{1-\nu^2}{Y} \right)^{\frac{2}{3}} \left(\frac{P}{x^2} \right)^{\frac{5}{3}} \quad (3)$$

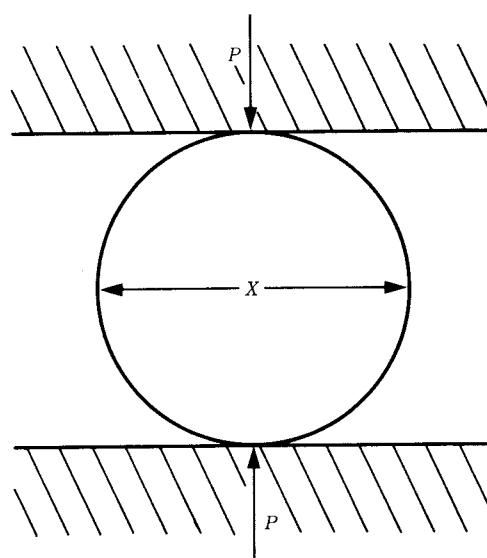


Fig. 1 Crushing of sphere

where ρ is the particle density.

The compressive strength of spheres[☆] was presented by Hiramatsu et al.²⁾ as

$$S = \frac{2.8P}{\pi x^2} \quad (4)$$

Substituting Eq. (4) into Eq. (3), E/M is determined from the compressive strength as follows:

$$\frac{E}{M} = 0.897 \rho^{-1} \pi^{\frac{2}{3}} \left(\frac{1-\nu^2}{Y} \right)^{\frac{2}{3}} S^{\frac{5}{3}} \quad (5)$$

The strength of material, which is well known to be sensitive to its structure¹⁴⁾ and thus dependent upon its size, is generally expressed as^{1,7)}

$$S = (S_0 V_0^{\frac{1}{m}}) V^{-\frac{1}{m}} \quad (6)$$

where S_0 is the strength of a specimen having a unit volume V_0 and m is Weibull's coefficient of uniformity with the value greater than 1. As shown in Eq. (6), the effect of specimen volume on strength decreases with increasing m , and the material becomes perfectly uniform in the limiting case as $m = \infty$ ^{☆☆}

By use of Eqs. (5) and (6), the fracture energy and the specific fracture energy at size x are rewritten respectively as follows:

$$E = 0.15 \cdot 6^{\frac{5}{3m}} \cdot \pi^{\frac{5m-5}{3m}} \cdot \left(\frac{1-\nu^2}{Y} \right)^{\frac{2}{3}} \cdot (S_0 V_0^{\frac{1}{m}})^{\frac{5}{3}} \cdot x^{\frac{3m-5}{m}} \quad (7)$$

$$\frac{E}{M} = 0.897 \cdot 6^{\frac{5}{3m}} \cdot \rho^{-1} \cdot \pi^{\frac{2m-5}{3m}} \cdot \left(\frac{1-\nu^2}{Y} \right)^{\frac{2}{3}} \cdot (S_0 V_0^{\frac{1}{m}})^{\frac{5}{3}} \cdot x^{-\frac{5}{m}} \quad (8)$$

The ratio E/M increases over the finer region of x with a decrease in the coefficient m or the lack of uniformity of the material in question.

3. Experimental results and discussion

3.1 Experimental results of compressive strength of spheres and fracture energy

The typical values of E/M of borosilicate glass, quartz, feldspar, and marble plotted

against the strength S are shown in Figs. 2 and 3 by using all the specimens of Table 2. The straight lines in these diagrams represent calculated solutions derived from the values ρ , Y , and ν in Table 1⁹⁾ which were experimentally obtained.

It is clear from Figs. 2 and 3 that the agreement between the experiment and the calculation seems to be satisfactory and thus these materials can be considered as semi-elastic solids. The similar tendency was also given for quartz glass. For marble, on the other hand, its experimental values are greater than the calculated line as indicated in Fig. 3. This reason was stated in the previous paper¹²⁾ as follows; the authors numerically integrated the load-displacement curve to obtain the whole fracture energy and determined the ratio of the energy required for plastic deformation to the whole energy by use of extrapolation. The calculated ratio in the case of marble was about 0.63, and this implies that the fracture energy measured would consist of the large amount of plastic deformation. From this reason, the experimental values might be greater than the calculated solutions.

For limestone and gypsum, the ratios were 0.55 and 0.78 respectively and both of their experimental results gave greater values than

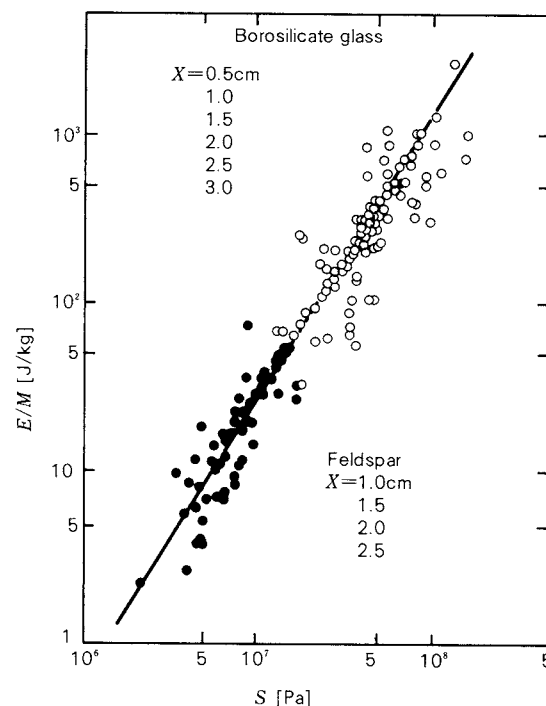


Fig. 2 Relationships between strength S and specific fracture energy E/M

☆ The value S can be calculated under compressive load which is applied on points even if the shape of particles are irregular.

☆☆ This does not imply ideal material without flaw alone, but uniform one which has the various kinds of flaw.

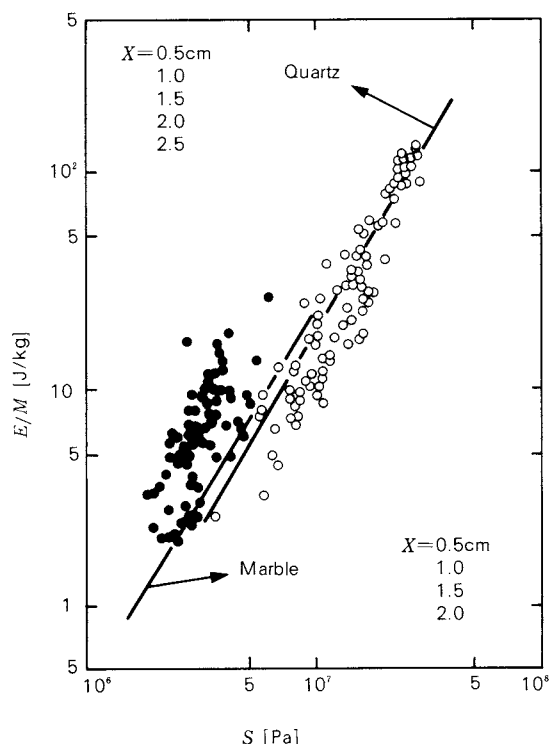


Fig. 3 Relationships between strength S and specific fracture energy E/M

the calculated solutions, though not schematically indicated here.

Summarizing the above discussion is that when the material has plastic characteristics, the fracture energy obtained experimentally is greater than the calculated solution. Therefore Eq. (5) will be available for estimating the fracture energy, only when the portion of plastic deformation energy and elastic strain energy can be determined in advance as stated in the previous paper¹²⁾.

3. 2 Relationship between particle size and fracture energy

By use of Eqs. (7) and (8), Weibull's coefficient of uniformity m yields the fracture energy of a single particle E and the specific fracture energy E/M . A typical relationship between the specimen volume and the strength presented in the previous paper¹³⁾ is indicated in Fig. 4, which shows a set of line segments obtained by the least squares method. Such a relation was found to be expressed as a single straight line with a constant slope for glass materials and as a set of line segments with plural slopes for natural materials[☆]. In any case, however, the results imply that the strength will increase with

decreasing particle volume or particle size.

The calculated solutions of E and E/M by use of Eqs. (7) and (8) and the values of m in the previous paper¹³⁾ are plotted against the particle size x in Figs. 5, 6 and 7. The values of E and E/M are expressed as a straight

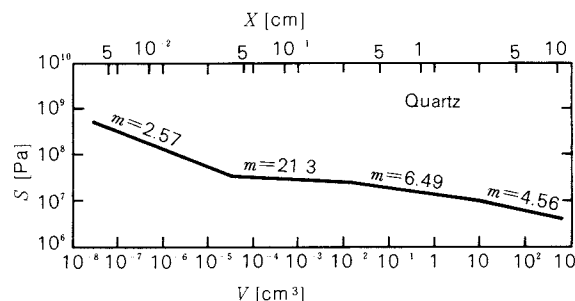


Fig. 4 Variation of strength S with volume of specimen V for quartz

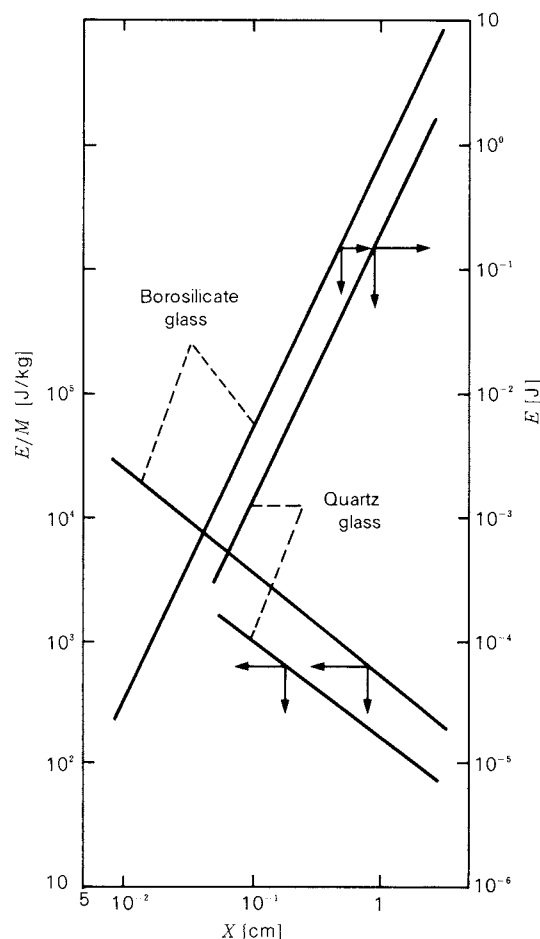


Fig. 5 Relationships between size x and specific fracture energy E/M or fracture energy E

☆ It seems that the relationship between volume and strength for glass material shows the similar tendency when the same manufacturing procedure as that of natural materials are employed. The detail of this is under examination.

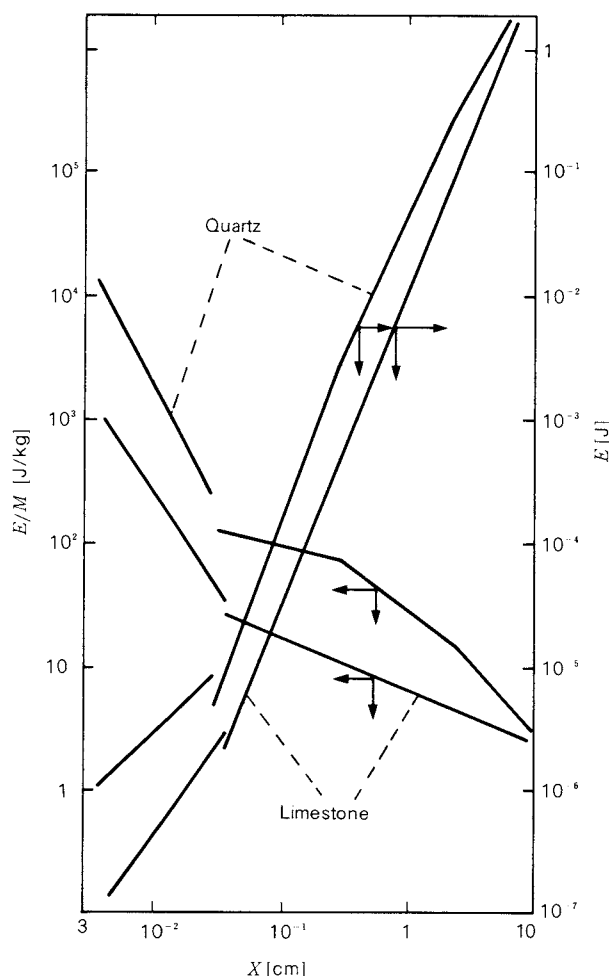


Fig. 6 Relationships between x and E/M or E

line for glass material as shown in Fig. 5. On the other hand, they are revealed as a set of line fragments with different slopes for the natural materials as indicated in Figs. 6 and 7. Such a discontinuous distribution is considered to result from the following procedure; first, the relationship between specimen volume and strength was determined in view of a representative straight line which indicates the most acceptable points in the fluctuated values obtained in this work. Then the line segments which were to result in the minimum probable error over each size range in question were determined. From this reason, the end points of each line segment were separated although the particle size distribution was continuous. In practice, however, the correlated line may pass continuously near these end points.

It is clear from Figs. 6 and 7 that the ratio E/M of natural materials remarkably increase

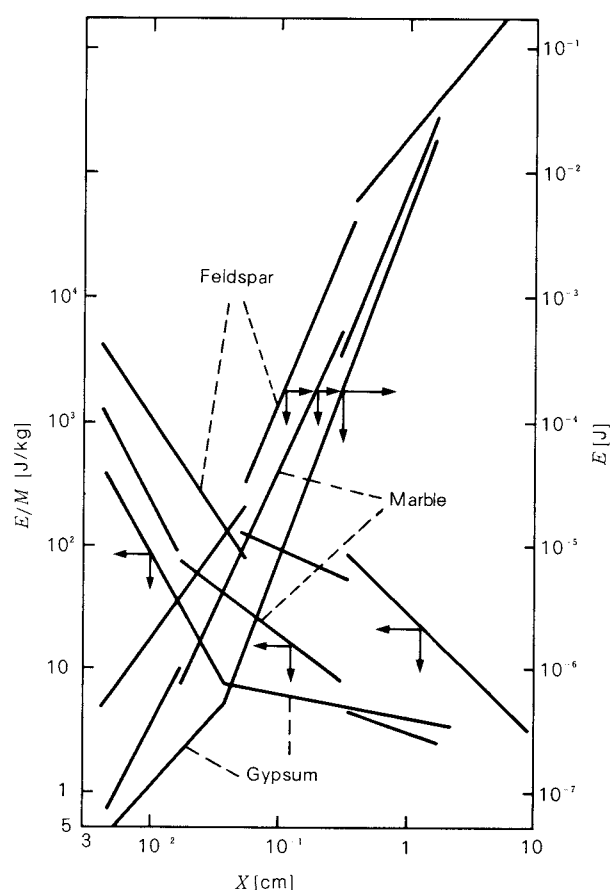


Fig. 7 Relationships between x and E/M or E

with a particle size less than $500 \mu\text{m}$, and this implies the large amount of energy required for producing fine particles.

The results obtained in this work are based on the ideal fracture experiment under static, compressive load. It should be noticed that a practical fine comminution is accompanied by a fracture of irregular shaped particles under dynamic or impact load and the values ν , Y and S in Eqs. (6), (7) and (8) are dependent upon the loading speed¹¹⁾. It should be also remarked that these results will be available for practical use only if the condition used is reasonably restricted.

Conclusion

The relationship between compressive strength of spheres and fracture energy was experimentally investigated under static compressive load by using 7 kinds of specimens of 0.5 to 3 cm in diameter. Furthermore, the values of fracture energy per a single particle and unit mass of the particles with a diameter range of 0.0030 to 10 cm were calculated by

use of the relationship between particle volume (particle diameter) and strength which had been previously reported. Summarizing the results of this study:

- 1) The fracture energies were larger than the values calculated from the theoretical equations for plastic-like materials such as limestone, marble and gypsum, while these values were in reasonable agreement for quartz glass, borosilicate glass, quartz, and feldspar.
- 2) For natural materials, the specific fracture energies rapidly increased with decreasing particle size within the range of particle size smaller than about $500\ \mu\text{m}$, and this implies the large amount of energy required for producing fine particles.

Although the results obtained in this work are based on the ideal fracture behavior and seem to differ from the actual one, the resultant tendency may be reasonably available for practical use.

Nomenclature

E : fracture energy	[J]
E/M : specific fracture energy	[J/kg]
m : Weibull's coefficient of uniformity	[—]
P : load	[N]
S : compressive strength of sphere	[Pa]
S_0 : compressive strength of sphere per unit volume V_0	[Pa]
V : volume of specimen	[cm ³] or [m ³]

W_i : Bond's work index	[kWh/t]
x : particle size	[cm] or [m]
Y : Young's modulus	[Pa]
Δ : deformation of specimen	[m]
ν : Poisson's ratio	[—]
ρ : density of specimen	[kg/m ³]

References

- 1) Epstein, B.: *J. Appl. Phys.*, **19**, 140 (1948).
- 2) Hiramatsu, Y., T. Oka and H. Kiyama: *J. Min. Inst., Japan*, **81**, 1024 (1965).
- 3) Kanda, Y., S. Yashima and J. Shimoizaka: *J. Min. Inst., Japan*, **85**, 1024 (1969).
- 4) Nakagawa, Y., K. Matsui and S. Okuda: *Kagaku Kōgaku*, **18**, 146 (1954).
- 5) Nishimatsu, Y., S. Ōkubo, T. Yamaguchi and S. Koizumi: *J. Min. Inst., Japan*, **97**, 1163 (1981).
- 6) Tanaka, T.: *Kagaku Kōgaku*, **18**, 180 (1954).
- 7) Weibull, W.: *Ing. Vetenskaps Akad. Handl*, No. 151 (1939).
- 8) Yamaguchi, U.: *J. Soc. Materials Sci., Japan*, **14**, 198 (1965).
- 9) Yashima, S., S. Morohashi, O. Awano and Y. Kanda: *Kagaku Kōgaku*, **34**, 210 (1970).
- 10) Yashima, S., Y. Kanda, T. Izumi and T. Shinozaki: *ibid.*, **36**, 1017 (1972).
- 11) Yashima, S., Y. Kanda, T. Sasaki, M. Iijima and F. Saito: *ibid.*, **27**, 1218 (1973).
- 12) Yashima, S., F. Saito, T. Sagawa, T. Numata, S. Sano and Y. Kuwabara: *J. Min. Inst., Japan*, **91**, 535 (1975).
- 13) Yashima, S. and F. Saito: *J. Res. Assoc. Powder Tec., Japan*, **16**, 714 (1979).
- 14) Yokobori, T.: "*Zairyo Kyōdogaku*", Gihōdō, Tokyo, 86 (1955).

Process of Forming Seamless Capsules by Concentric Nozzle System[†]

Toshiyuki Suzuki, Hideki Sunohara
and Ryosei Kamaguchi

Morishita Jintan Co., Ltd.*

Abstract

Adaptation of the natural phenomenon of drop formation has resulted in the development of forming seamless capsules.

The encapsulation behavior of gelatine in coolant fluid has been studied using a concentric nozzle. The major assumption was that capsules were formed through a wave-like instability in the concentric streams of extruded core, shell, and coolant fluids.

Predictions of flow rates and fluid properties were compared with experimental results and were shown to be in reasonably good agreement. It was found that for a given set of flow rates and fluid properties optimum conditions could result in forming uniform size capsules.

1. Introduction

One of the advantages of a capsule is to apparently treat formless liquid as a solid form. A soft capsule which is formed by concentric nozzle system based on an orifice method is called a seamless mini-capsule, and has been widely used for a variety of industries such as food, pharmacy, and so on. This capsule shows excellent powder characteristics of fluidity and packing behavior since it is formed to have spherical shape. However, the influence of physical property on capsule formation process has been scarcely investigated. This paper presents experimental findings on this influence with the aid of a fundamental model concept.

2. Experimental equipment

The experimental equipment used in this work is schematically illustrated in Fig. 1.

Shell liquid and core liquid stored in each

tank ① and ② respectively were introduced quantitatively into a concentric nozzle ⑤ by gear pumps ③ and ④ and discharged out of the tip of the nozzle so that a jet flow ⑧ could be formed in a guide tube ⑦. When the flow of coolant oil filled in this guide tube was laminar, the stable elongation of the jet flow would be permitted to make sequential formation of resultant capsules. In this process, moreover, a vibration ring ⑪ was equipped to form uniform size capsules.

On the other hand, the coolant oil to be used for forming capsules by cooling was introduced into the guide tube ⑦ mounted at the center of a cooling cylinder ⑥, after being cooled in a heat exchanger ⑰. This liquid accompanied by formed capsules was transported through a cooling tube ⑫, before being made to be separated from the capsules by separator ⑬ placed at the outlet of the tube. After this separation, the liquid was stored in a coolant oil tank ⑭ and returned to the heat exchanger through a pipe ⑮ by gear pump ⑯.

3. Experimental procedure and results

In this work, the influence of each liquid flow rate and shell liquid viscosity on capsule formation process was experimentally investigated. For simplification, the core liquid, the shell liquid, and the coolant oil will be called

* 1-30 Tamatsukuri, 1-chome, Higashi-ku, Osaka, 540
TEL. 06 (761) 1131

† This report was originally printed in *J. Soc. Powder Tech., Japan*, 20, 723-727 (1983) in Japanese, before being translated into English with the permission of the editorial committee of the Soc. Powder Tech., Japan.

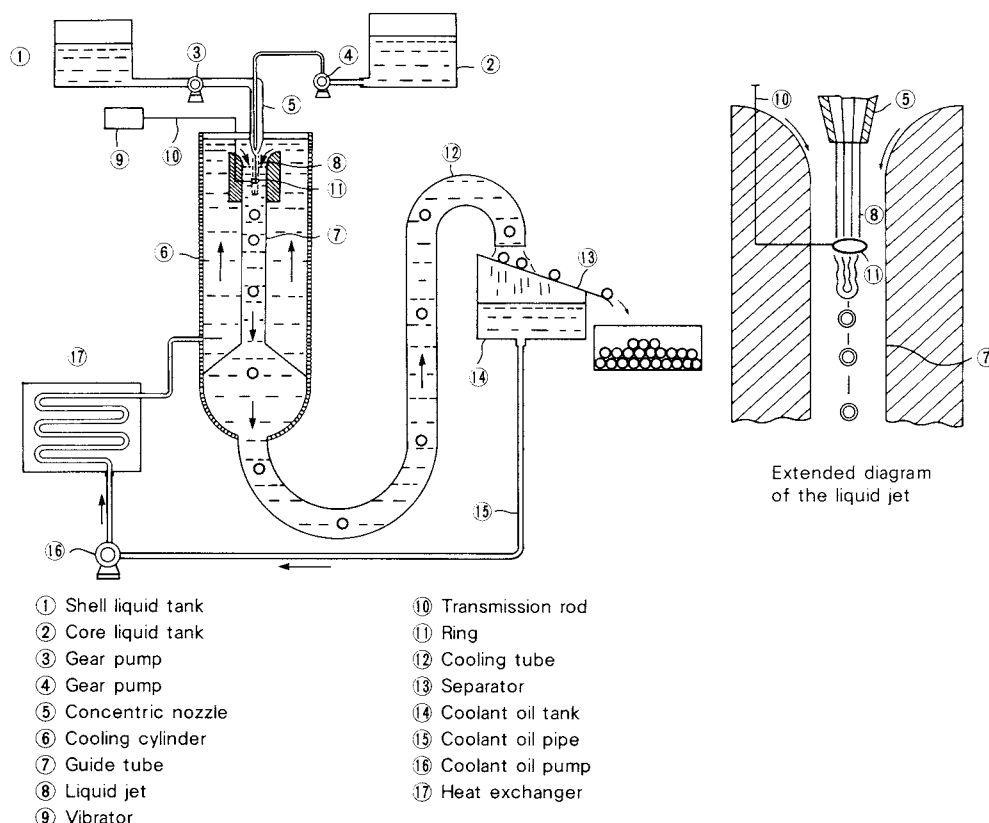


Fig. 1 Schematic diagram of apparatus

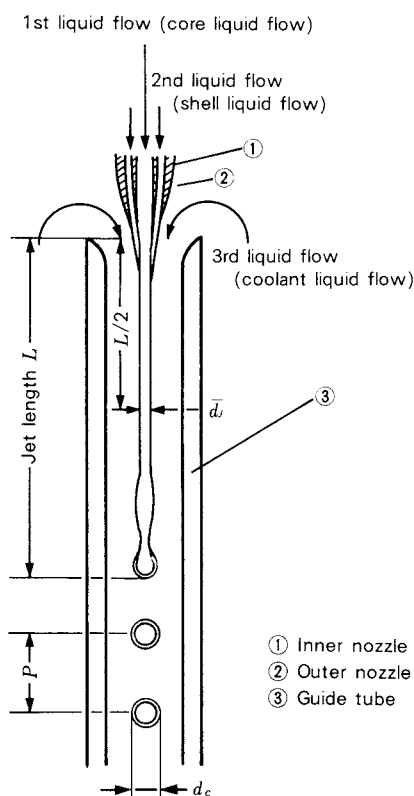


Fig. 2 Schematic of capsulation

liquids 1, 2, and 3, respectively, in this paper.

The formation of capsules is schematically outlined in Fig. 2. The jet length L is considered to be a distance where the jet flow of liquids 1 and 2 is capable of maintaining its stability. In this case, the diameter of this jet flow at the point which is $L/2$ distant from the tip of the nozzle may be reasonably regarded as a standard dimension of the flow; however it should be noticed that the diameter at an arbitrary point is dependent upon the vertical distance in the flow.

Relationship between jet diameter \bar{d}_j and capsule diameter d_c

The influence of jet diameter \bar{d}_j on capsule diameter d_c was experimentally studied under the conditions listed in Table 1. As shown in Fig. 3, plots of the results hardly deviated from the single straight line which demonstrated that d_c would be twice as large as \bar{d}_j . It is found that this result might be in good agreement with the solution derived from the Rayleigh theory for instability of liquid jets¹⁾.

Table 1 Experimental conditions

Condition	1st liquid flow rate q_1 [g/s]	2nd liquid flow rate q_2 [g/s]	3rd liquid flow rate q_3 [g/s]
1	0.653	0.531	16.6
2	0.557	0.531	26.3
3	0.477	0.531	36.0
4	0.374	0.531	45.7
5	0.281	0.531	55.4
6	0.194	0.531	

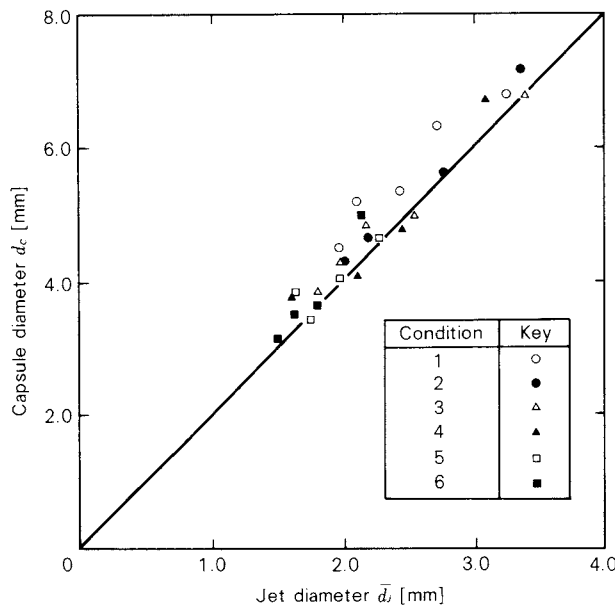


Fig. 3 Correlation of capsule diameter d_c and jet diameter d_j

Capsule formation

Consider a typical capsule model during its successive formation as illustrated in Fig. 4. Provided that the distance between the successively formed two capsules (pitch P) is assumed to be the length of the cylindrical jet flow required to make one capsule, the following equation is given:

$$\pi \left(\frac{\bar{d}_j}{2} \right)^2 P = \frac{4}{3} \pi \left(\frac{d_c}{2} \right)^3 \quad (1)$$

As shown in Fig. 5, the experimental results based on the conditions presented in Table 1 seem to be little apart from the linear relation of Eq. (1). It follows that Eq. (1) could reasonably relate the jet diameter \bar{d}_j and the capsule diameter d_c , which was also confirmed by Dabora²⁾. From Eq. (1), the capsule diameter d_c can be rewritten as a function of pitch P as well as jet diameter d_c as follows.

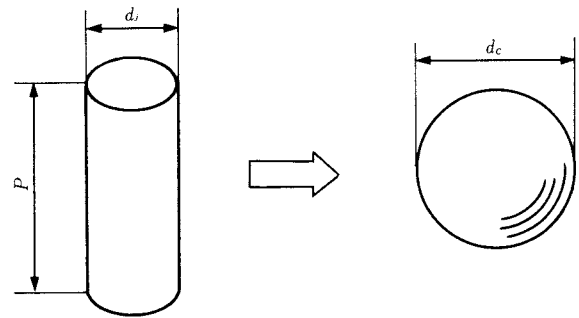


Fig. 4 Equality of volume between jet and capsule

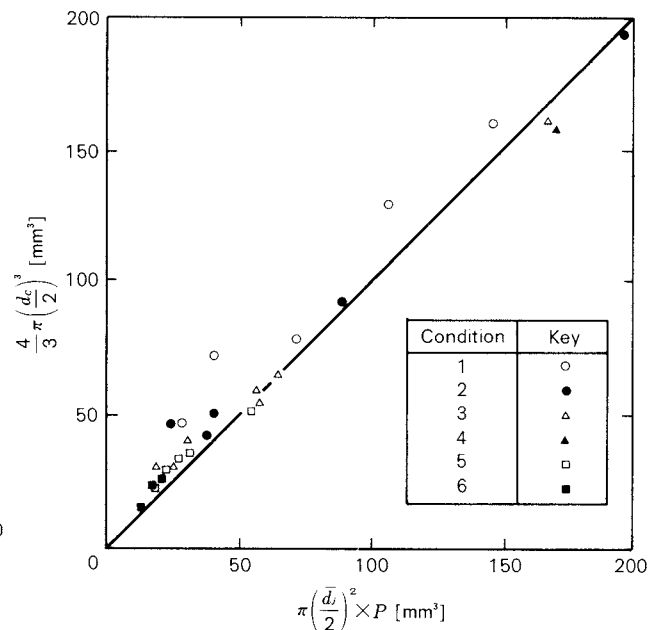


Fig. 5 Correlation of capsule volume and jet volume

$$d_c = \left(\frac{3}{2} \bar{d}_j^2 P \right)^{1/3} \quad (2)$$

This equation states that capsule diameter d_c can vary with jet diameter \bar{d}_j alone, if pitch P is held constant. Pitch P may be held constant, if vibration is applied to the jet flow. By the way, under the conditions listed in Table 1 the encapsulation processes observed is schematically illustrated in Fig. 6; the capsule diameter decreased with increasing the value of q_3 . On the other hand, it was found that the jet diameter \bar{d}_j increased with increasing the values of q_1 and/or q_2 .

Relationship between flow rate ratio $(q_1 + q_2)/q_3$ and jet diameter \bar{d}_j

From the facts mentioned above, it can be known that liquids 1 and 2 might be positive factors for rising the jet diameter \bar{d}_j and liquid 3 might be a negative one. Figure 7 shows the

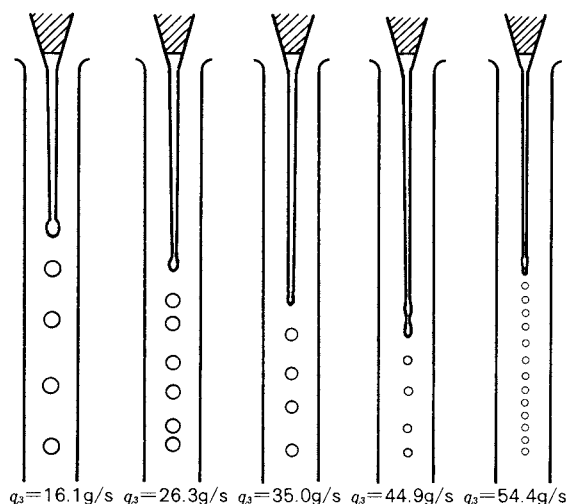


Fig. 6 Effect of 3rd liquid flow rate on capsulation

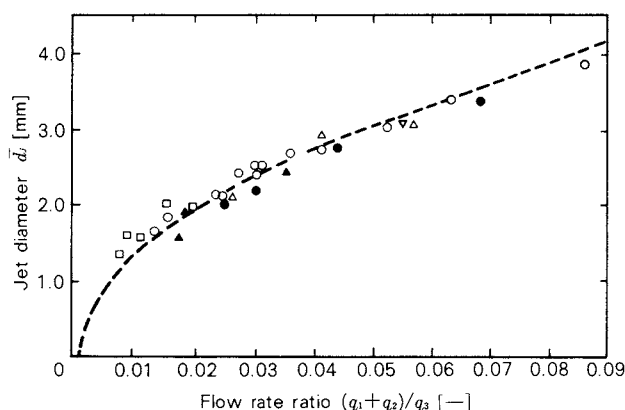


Fig. 7 Correlation of jet diameter \bar{d}_j and flow rate ratio $(q_1 + q_2)/q_3$

dependence of the flow rate ratio $(q_1 + q_2)/q_3$ upon the jet diameter \bar{d}_j .

When it is assumed that all the liquids are Newtonian and flow at the same rate, the following equation can be given:

$$\frac{q_1}{\gamma_1} + \frac{q_2}{\gamma_2} = \frac{\pi}{4} \bar{d}_j^2 V_{3max} \quad (3)$$

where γ_i is the specific weight in g/cm^3 for the i -th liquid. The maximum flow rate of liquid 3 is expressed as

$$V_{3max} = \frac{8q_3}{\pi \gamma_3 d_3^2} \quad (4)$$

The experimental condition employed in this work was that $\gamma_1 = \gamma_2 = 1 \times 10^{-3} \text{ g/mm}^3$, $\gamma_3 = 0.94 \times 10^{-3} \text{ g/mm}^3$, and $d_3 = 20 \text{ mm}$. Thus Eqs. (3) and (4) can be rewritten as the following relation:

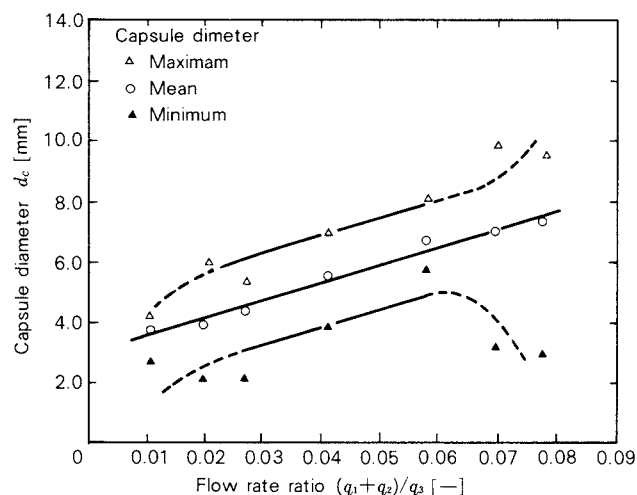


Fig. 8 Relation between capsule diameter d_c and flow rate ratio $(q_1 + q_2)/q_3$

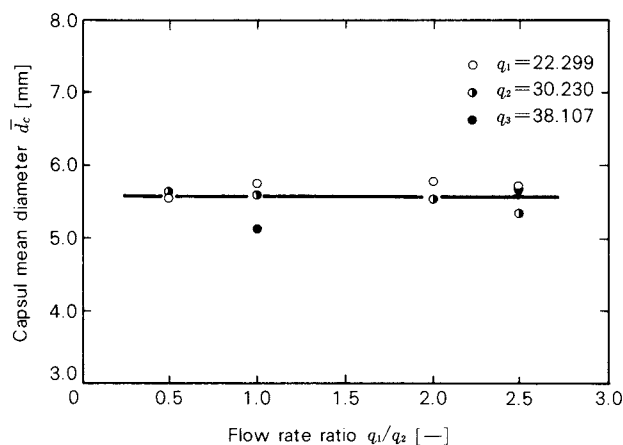


Fig. 9 Relation between capsule mean diameter d_c and flow rate ratio q_1/q_2

$$\bar{d}_j^2 = 188 \frac{q_1 + q_2}{q_3} \quad (5)$$

It is obvious from Fig. 7 that the plots obtained experimentally in this work is in good agreement with the solution of Eq. (5) indicated as the dotted curve. This suggests that the assumption in the above was consistent with the result of this work.

Relationship between flow rate ratio $(q_1 + q_2)/q_3$ and capsule diameter d_c

To find the dependence of the flow rate ratio $(q_1 + q_2)/q_3$ upon the capsule diameter d_c , another encapsulation experiment was carried out under the condition of the temperatures of 22, 80, and 10°C for liquids 1, 2, and 3 respectively and the concentration of 25% for liquid 2. The experimental condition and the result are indicated in Table 2 with the

Table 2 Flow rate ratio $(q_1 + q_2)/q_3$ and capsule diameter d_c

Liquid flow rate			Flow rate ratio	Capsule diameter d_c [mm]		
1st liquid q_1 [g/s]	2nd liquid q_2 [g/s]	3rd liquid q_3 [g/s]	$(q_1 + q_2)/q_3$ [-]	Minimum	Mean	Maximum
0.1473	0.3057	38.107	0.01189	2.70	3.80	4.30
0.3180	0.3057	30.203	0.02065	2.10	3.90	5.95
0.4318	0.4151	30.203	0.02804	2.10	4.35	5.25
0.3180	0.3057	14.395	0.04332	3.95	5.49	7.00
0.4318	0.4151	14.395	0.05883	5.75	6.71	8.10
0.5171	0.4972	14.395	0.07046	3.25	7.01	9.85
0.5740	0.5519	14.395	0.07821	3.00	7.35	9.50

schematic illustration of Fig. 8. It is found from this figure that the flow rate ratio $(q_1 + q_2)/q_3$ was approximately proportional to the capsule diameter d_c with a region of $0.02 < (q_1 + q_2)/q_3 < 0.06$. This implies that there could be an optimum flow rate ratio for formation of the capsule with a uniform diameter.

Influence of flow rate ratio q_1/q_2 on mean capsule diameter \bar{d}_c

As shown in Fig. 9, the mean capsule diameter \bar{d}_c was almost independent of the ratio of the flow rate of liquid 1 to that of liquid 2, q_1/q_2 .

Influence of liquid 2 concentration on mean capsule diameter

The mean capsule diameters are plotted against the concentration of liquid 2 as a function of $(q_1 + q_2)/q_3$ in Fig. 10. It is found that the diameter decreased with increasing the concentration and this tendency became more remarkable as $(q_1 + q_2)/q_3$ increased. This is probably because the spherical formation of the capsules was enhanced both by the increase in the surface tension of liquid 2 due to the rise of its concentration and by increase in the flow rate of liquid 3 which resulted in reduced jet diameter.

The physical factors investigated in this work were the flow rate of the liquids and the viscosity of liquid 2 and they might be also dependent on a more fundamental factor, i.e. temperature. Therefore further study on the influence of temperature should be required to control the capsule formation process more precisely, although only the restricted range of the temperature effect was investigated in this work.

4. Conclusion

It has been little known how the two kinds of liquid are discharged out of the concentric nozzle into another liquid in a jet flow. In this work, we investigated the influence of these three liquids on the diameter of capsule formed in this solidification process in order to elucidate such a complicated fluid dynamic behavior. The results of experiments and observations are summarized below.

- 1) The capsule diameter d_c is about twice as large as the jet diameter \bar{d}_j .
- 2) The capsule diameter d_c is dependent upon the pitch P as well as the jet diameter \bar{d}_j , and thus d_c may be held constant if vibration is applied on the flow to fix the value of P .
- 3) There is an optimum flow rate ratio $(q_1 + q_2)/q_3$ which yields the capsules with a uniform diameter.
- 4) The capsule diameter d_c decreases with an increase in the viscosity of the shell liquid.
- 5) The diameter of stabilized capsules may be determined when the velocity of the jet flow coincides with that of the coolant oil.

Based on this work, we intend to investigate the influence of other physical factors such as temperature, specific weight, and so on.

Acknowledgement

We wish to express our gratitude to Professor Akira Horikawa and his staff in Osaka University for their kind suggestion and cooperation.

Nomenclature

d_c	: capsule diameter	[mm]	q_3	: flow rate of coolant oil	[g/s]
\bar{d}_c	: mean capsule diameter	[mm]	V_{3max}	: maximum velocity of coolant oil	[mm/s]
\bar{d}_j	: jet diameter	[mm]	γ_1	: specific weight of core liquid	[g/cm ³]
d_3	: inner diameter of guide tube	[mm]	γ_2	: specific weight of shell liquid	[g/cm ³]
L	: jet length	[mm]	γ_3	: specific weight of coolant oil	[g/cm ³]
P	: pitch	[mm]			
q_1	: flow rate of core liquid	[g/s]			
q_2	: flow rate of shell liquid	[g/s]			

References

- 1) Rayleigh: *Proc. London Math. Soc.*, **10**, 4 (1878)
- 2) Dabora: *Rev. Sci. Instr.*, **38**, 502 (1967).

Numerical Simulation of Pneumatic Conveying in a Horizontal Pipe

**Yutaka Tsuji, Takao Oshima
and Yoshinobu Morikawa**

*Department of Mechanical Engineering
for Industrial Machinery
Osaka University**

Abstract

A numerical simulation was attempted for pneumatic conveying of solids in a horizontal pipe. Trajectories of individual particles were calculated using equations of motion. In this simulation, the fluid drag, lift force due to particle rotation and torque on the rotating particles were taken into consideration. The friction loss due to collision of particles with a pipe wall was also calculated using impulsive equations. The pressure drop due to the presence of particles was obtained from the fluid drag acting on the particles through the momentum theorem. To avoid sliding motion of particles on a pipe bottom wall, a model of abnormal bouncing was newly proposed. Several parameters concerning the abnormal bouncing were determined empirically. It was found that the particle flow predicted by the present simulation agreed with measurements regarding particle distribution, pressure drop and particle velocities including angular velocities. In addition, this method was applied to find the effects of particle size, pipe diameter, particle density and so forth. Since particle diffusion due to the air turbulence was neglected in this analysis, the case of fine particles was not investigated.

1. Introduction

Technology of pneumatic conveying was developed in the middle of the 19th century for transportation of grains. Although a number of investigations have been carried out by many workers to improve facilities and refine design procedure, appropriate prediction of pressure drops is not still easy. This is because development of various industries has been increasing the number of solid materials to be conveyed and their properties of friction against a pipe wall depend largely upon each material. Therefore, it is very difficult to establish a unified theory quantitatively predicting the phenomena.

The methods of analysis for pneumatic conveying system may be classified into the follow-

ing three stages.

- (1) One-dimensional analysis (highly empirical)
- (2) Numerical analysis based on individual particle trajectories, by neglecting the interaction between the particles and fluid.
- (3) Numerical analysis based on individual particle trajectories, by taking the interaction into consideration.

The first method

The analysis based upon the first method has been conducted by experiment depending upon the material and the condition. Although many monographs and papers describing this approach have been presented and various empirical factors have been introduced into the equations for pressure drop, the mechanism of friction between particle and wall is not directly considered.

The second method

A trajectory of each particle is calculated numerically by computer simulation, where the

* 2-1, Yamada-oka, Suita, Osaka, 565
TEL. 06 (877) 5111

Received March 3, 1985

values of mean particle velocity and pressure drop can be obtained as an ensemble average value.

It should be noticed that this method assumes that fluid motion is not affected by the presence of particles except for the loss of pressure energy; that is, the relationship between particle and fluid is a "one way path". This assumption is contradictory to the measurements by Laser Doppler anemometer even in a dilute-phase conveying^{2,3)}. Fortunately it is known, however, that the assumption of the one way path causes no serious errors in pressure loss.

The third method

The analysis based upon the third method can also be carried out by computer simulations. As one of the simulations for single phase flows, the Navier-Stokes equation is usually used, by taking momentum exchange between particles and fluid into consideration. Although this method has been already used for several analyses of two-phase flows, more research will be necessary before it is applicable to pneumatic conveying. This is because there are several barriers to be overcome.

First, the situation of pneumatic conveying which differs from other types of two-phase flows is that collision of the particles against the wall should be dealt with. The collision reduces kinetic energy of the particles. The particles which lose the kinetic energy are accelerated by fluid through the drag force which results in the loss of pressure energy of the fluid. If the problem of the collision remains unsolved, the numerical solution of the Navier-Stokes equation pursued in detail will be meaningless. Therefore it is a pre-requisite to clear up the collision problem in the second method.

Secondly, the pipe flow used in pneumatic conveying is usually turbulent, and turbulence is also greatly influenced by the presence of particles. The problem how to deal with the interaction between turbulence and particle motion is beyond the scope of the present knowledge of pneumatic conveying, though it is interesting from the viewpoint of fluid mechanics. The difficulty due to turbulence could be avoided, if some convenient assumptions and models would be adopted in analyses. However, the third method based on such

simple assumptions is not regarded superior to the first or second one.

The object of the present paper is to apply the second method to particle flow in pneumatic conveying. For convenience of computer simulation, the discussion is limited within the condition; particles used are assumed to be spherical because calculation becomes simplified, and large because they are little affected by fluid turbulence.

2. Outline of the present simulation

The behavior of particles transported in a pipeline is simple in a sense that particles are discharged from a feeder to a pipeline and travel under the influence of fluid-dynamic and gravitational forces with occasional collision against the wall. This is all that should be taken into consideration in the simulation. However, each particle shows a different trajectory, because the initial position and velocity have different values and the collision also causes a kind of randomness even in the case of spherical particles. This problem will be discussed in the later section. In the present simulation, the initial conditions of particle motion are given by random numbers. When equations of motion are given as well as equations of energy loss due to collision, the whole motion of each particle can be calculated. Practical data required for design works such as mean particle velocity, distribution of particles and pressure drop are obtainable by averaging the results of the calculation for many particles.

Fluid-dynamic forces acting on the particles are drag, lift and viscous dissipation of particle rotation. Existing knowledge of fluid mechanics gives sufficient information on these forces and thus one has no difficulty in estimating them. On the other hand, the effects of collision are difficult to estimate. If the particle size is much smaller than the pipe diameter, it can be assumed that the particle collides with a flat plate instead of the curved plane of a pipe wall. Change in particle velocity due to such collision can be estimated by using impulsive equations with the coefficients of restitution e and kinetic friction f . The coefficients of restitution and kinetic friction are dependent upon both the materials of particles and pipe wall. These values are obtained in an experiment where a particle falls on a plate if the material

of the test plate and the pipe wall is the same. On the other hand, friction factors used in an one-dimensional analysis must be determined by the actual data of experiments.

The similar calculation was already applied to the simulation of pneumatic conveying including pipe bends⁵⁾. The results were satisfactory with respect to the effects of bends. However, this simulation neglected a factor which was necessary to enable the particles to continue bouncing motion. Therefore when a particle repeats the bouncing motion many times in a horizontal and long pipe with the coefficient of restitution e less than unity, the incidence angle of the particle against the wall decreases till the particle begins to slide on the wall. In the present work, artificial irregularity is assumed in the bouncing motion to prevent such sliding so that the simulation is applicable to a long pipe.

3. Collision between a single particle and wall

Consider a three dimensional collision of a spherical particle with a flat plate as shown in Fig. 1. When the coefficients of restitution and kinetic friction are given, particle motions before and after the collision can be estimated by solving impulsive equations. This may be based upon classical dynamics. To solve the collision problem, the following assumptions were used.

- (1) Plastic deformation and fracture are neglected.
- (2) There exists a period when the particle slides on the plate.
- (3) Once the particle stops sliding motion, it slides no longer.
- (4) The friction between the particle and plate obeys Coulomb's law.

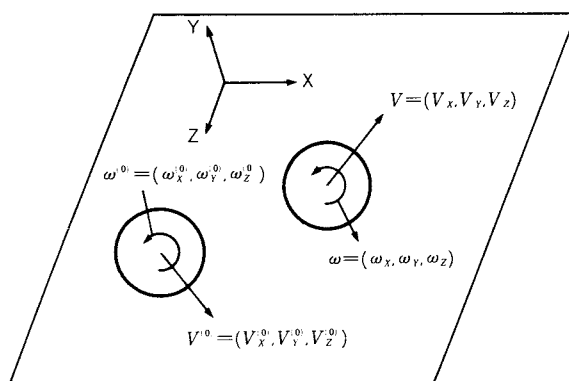


Fig. 1 Collision of a spherical particles with a flat plate

- (5) The distance between the center of particle mass and contact point is kept constant a throughout the process of collision.

The process of collision is divided into two periods: the period during which the material in collision is compressed and the period during which this compression is released. The former and the latter are called the compression and recovery periods, respectively. The coefficient of restitution e is defined by

$$e = J_n^{(2)} / J_n^{(1)} \quad (1)$$

where $J_n^{(1)}$ is the normal component of the impulse of the force which acts on a particle in the compression period and $J_n^{(2)}$ is the one in the recovery period. Coulomb's law says that the impulse of the friction force is the product of the impulse of the normal force and the coefficient of kinetic friction f . Thus when the particle slides on the X - Z plane, the impulse J_t of the friction force is expressed as

$$J_t = -\epsilon_X f J_Y i - \epsilon_Z f J_Y k \quad (2)$$

where i and k are unit vectors corresponding to X and Z directions, satisfying the following relation

$$\epsilon_X^2 + \epsilon_Z^2 = 1 \quad (3)$$

Signs of ϵ_X and ϵ_Z are defined to be equal to those of $V_X^{(0)} + a\omega_X^{(0)}$ and $V_Z^{(0)} - a\omega_X^{(0)}$, respectively.

In general, the particle comes into collision incorporated with particle rotation. Thus $U^{(0)}$, the velocity of the point, on which the particle is in contact with the wall is the sum of the velocities of translation and rotation, that is,

$$\begin{aligned} U^{(0)} &= V^{(0)} + r \times \omega \\ &= (V_X^{(0)} + a\omega_Z^{(0)})i + V_Y^{(0)}j + (V_Z^{(0)} - a\omega_X^{(0)})k \end{aligned} \quad (4)$$

The impulsive equations have different forms according to the following three cases.

- (1) Case I: the particle stops sliding in the compression period
- (2) Case II: the particle stops sliding in the recovery period.
- (3) Case III: the particle continues to slide throughout the collision.

The procedure to obtain the solution of Case I alone is shown in the following.

Table 1 Collision of Case I

(0) before the collision	(1) compression period		(2) recovery period	after the collision
	<div style="display: flex; align-items: center; justify-content: center;"> <div style="text-align: center; margin-right: 10px;"> \leftarrow the particle slides (s) </div> <div style="text-align: center; margin-right: 10px;"> \rightarrow (r) </div> </div>			
velocity	$V^{(0)}$	$V^{(s)}$	\widehat{V}	V
angular velocity	$\omega^{(0)}$	$\omega^{(s)}$	$\widehat{\omega}$	ω
impulse	$J^{(s)}$		$J^{(r)}$	$J^{(2)}$

Table 1 shows the velocities, angular velocities and impulses for each moment and period which must be considered in Case I. The known variables are only $V^{(0)}$ and $\omega^{(0)}$. All the velocities have three components corresponding to X , Y and Z directions, and thus there are 18 unknowns regarding these velocities. Furthermore, the impulses $J^{(s)}$, $J^{(r)}$ and $J^{(2)}$ are expressed as

$$J^{(s)} = -\epsilon_X f J_Y^{(s)} i + J_Y^{(s)} j - \epsilon_Z f J_Y^{(s)} k \quad (5)$$

$$J^{(r)} = J_X^{(r)} i + J_Y^{(r)} j + J_Z^{(r)} k \quad (6)$$

$$J^{(2)} = J_X^{(2)} i + e(J_Y^{(s)} + J_Y^{(r)})j + J_Z^{(2)} k \quad (7)$$

The above equations means that there are 6 unknowns regarding the impulses. Therefore, unknown variables of Case I total 26 at the beginning, since ϵ_X and ϵ_Z are added as unknowns.

Considering the momentum exchange at each moment, we have the following equations.

$$M(V^{(s)} - V^{(0)}) = J^{(s)} \quad (8)$$

$$M(\widehat{V} - V^{(s)}) = J^{(r)} \quad (9)$$

$$M(V - \widehat{V}) = J^{(2)} \quad (10)$$

$$I(\omega^{(s)} - \omega^{(0)}) = -r \times J^{(s)} \quad (11)$$

$$I(\widehat{\omega} - \omega^{(s)}) = -r \times J^{(r)} \quad (12)$$

$$I(\omega - \widehat{\omega}) = -r \times J^{(2)} \quad (13)$$

The boundary conditions are

$$[V^{(s)} + r \times \omega^{(s)}]_t = 0 \quad (14)$$

$$\widehat{V} + r \times \widehat{\omega} = 0 \quad (15)$$

$$[V + r \times \omega]_t = 0 \quad (16)$$

It is found that there are 26 equations (Eq. (3) and the three components of Eqs. (8) to (16)) are given for 26 unknowns, and then the problem can be solved if $V^{(0)}$ and $\omega^{(0)}$ are known.

The solutions of Case I are shown in the column (1) of Table 2. The condition that the particle stops sliding in the compression period is also shown in terms of the inequality in the same column which is deduced from the following condition,

$$J_Y^{(s)} > 0, \quad J_Y^{(r)} > 0 \quad (17)$$

The solutions of Case II and Case III, which are the same to each other, are shown in the column (2) of Table 2.

4. Determination of the coefficients of restitution and kinetic friction

Table 2 also provides a method of estimating the coefficients of restitution and kinetic friction if the particle velocities before and after collision are known. Consider a particle falling from a certain height to a plate inclined at the angle of α to the vertical line as shown in Fig. 2. That is, a two-dimensional collision with zero $\omega^{(0)}$ is dealt with. Velocity ratios $V_X/V_X^{(0)}$ and $V_Y/V_Y^{(0)}$ can be measured by using photographic method such as a camera or others. The coefficient of restitution is given by

$$e = -V_Y/V_Y^{(0)} \quad (18)$$

The ratio $V_X/V_X^{(0)}$ depends on α , e and f , i.e.

$$\tan \alpha < \frac{2}{7f(1+e)}, \quad V_X/V_X^{(0)} = 1 - f(1+e) \tan \alpha$$

$$\tan \alpha > \frac{2}{7f(1+e)}, \quad V_X/V_X^{(0)} = \frac{5}{7} \quad (19)$$

The velocity ratios calculated by Eqs. (18) and (19) using assumed values of e and f are indicated in **Fig. 3** to be compared with experimental results of other workers. **Figure 3 (a)**

presents the results of collision between a steel ball and plastic plate⁶⁾. It is found that e and f in this case take the following values,

$$e = 0.932, \quad f = 0.09 \quad (20)$$

Table 2 Solutions of the impulsive equations

	condition	velocity	angular velocity
(1)	$\frac{V_Y^{(0)}}{ V } < \frac{-2}{7f(e+1)}$	$V_X = \frac{5}{7} (V_X^{(0)} - \frac{2a}{5} \omega_Z^{(0)})$ $V_Y = -e V_Y^{(0)}$ $V_Z = \frac{5}{7} (V_Z^{(0)} + \frac{2a}{5} \omega_X^{(0)})$	$\omega_X = \frac{V_Z}{a}$ $\omega_Y = \omega_Y^{(0)}$ $\omega_Z = -\frac{V_X}{a}$
(2)	$\frac{-2}{7f(e+1)} < \frac{V_Y^{(0)}}{ V } < 0$	$V_X = V_X^{(0)} + \epsilon_X f(e+1) V_Y^{(0)}$ $V_Y = -e V_Y^{(0)}$ $V_Z = V_Z^{(0)} + \epsilon_Z f(e+1) V_Y^{(0)}$	$\omega_X = \omega_X^{(0)} - \frac{5}{2a} \epsilon_Z f(e+1) V_Y^{(0)}$ $\omega_Y = \omega_Y^{(0)}$ $\omega_Z = \omega_Z^{(0)} + \frac{5}{2a} \epsilon_X f(e+1) V_Y^{(0)}$

$$|V| = \sqrt{(V_X^{(0)} + a \omega_Z^{(0)})^2 + (V_Z^{(0)} - a \omega_X^{(0)})^2}$$

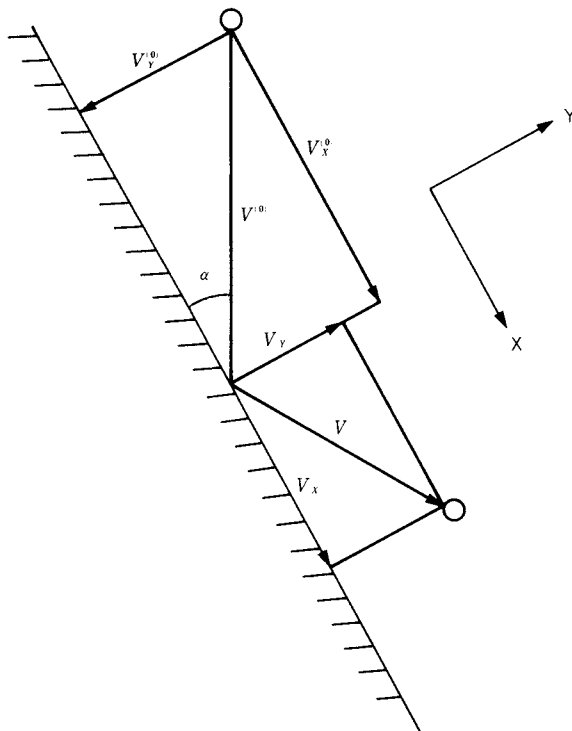
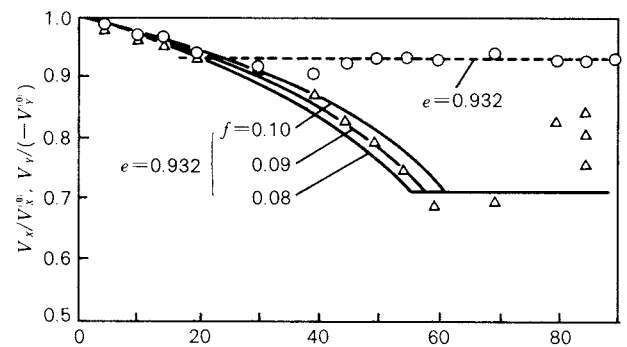
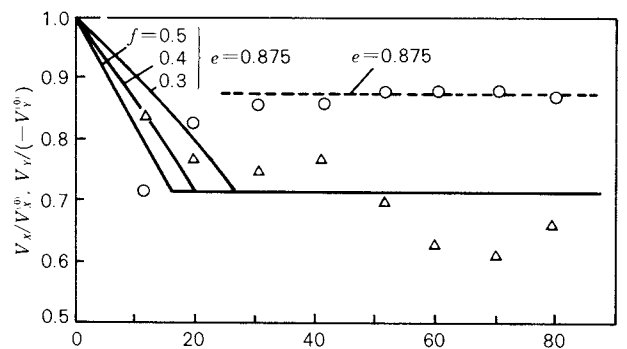
$$\epsilon_X = (V_X^{(0)} + a \omega_Z^{(0)})/|V|, \quad \epsilon_Z = (V_Z^{(0)} - a \omega_X^{(0)})/|V|$$


Fig. 2 A particle colliding with an inclined plate



(a) Steel ball (Brauer, 1980)



(b) Polyethylene pellet (Yamamoto, 1974)

Fig. 3 Velocity ratios

Figure 3 (b) shows that e and f of a polyethylene pellet and plastic plate are

$$e = 0.875, \quad f = 0.4 \quad (21)$$

In general, there have been very few reports on measurements of e and f for conveyed materials. Therefore, the values of e and f given by Eq. (21) are used in this work.

5. Equations of motion

5. 1 Coordinate system and initial condition

For practical pneumatic lines, particles are usually supplied downward from a hopper to a pipeline. Thus, the coordinate system shown in Fig. 4 is chosen in the present paper. In this system, x is the axial distance along the pipe, y , the horizontal axis normal to x , and z , the vertical axis in which the upward direction is taken positive.

Initial conditions of each particle were specified as follows. Although both actual falling velocities and positions are considered to be random, it is sufficient to take only the falling position as a random variable for the simulation. The initial position of a particle is given by r_0 and θ as shown in Fig 4 (b).

$$x = r_0 \sin \theta \quad (22)$$

$$y = r_0 \cos \theta \quad (23)$$

$$z = \sqrt{(D/2)^2 - r_0^2 \cos^2 \theta} \quad (24)$$

Values of r_0 and θ are given by the random numbers distributed uniformly within allowable ranges. The initial velocity of the particle $\dot{z} = (dz/dt)$ depends on the method of feeding. Fortunately, some empirical formulas are avail-

able for such falling velocities when the particles are discharged from the hopper⁸⁾.

5. 2 Fluid-dynamic forces and equations of motion

The equation of particle motion is written by

$$M\ddot{\chi} = F_D + F_L + F_G \quad (25)$$

where χ is the radius vector expressed as $x\mathbf{i} + y\mathbf{j} + z\mathbf{k}$. The values of F_D , F_L and F_G are forces due to drag, lift and gravity, respectively. Viscous dissipation due to rotation of the particle must be also taken into account. The assumptions used in the calculation of particle trajectories are as follows.

- (1) Existing results obtained in a uniform and stationary flow field are applied to the fluid-dynamic forces acting on the particle.
- (2) The velocity distribution of the air obeys the 1/7 power law, and it is not affected by the presence of particles. Also, particle motion is not influenced by air turbulence.
- (3) Collision between particles is neglected.

The magnitude of the drag force is expressed as

$$|F_D| = C_D A \left(\frac{1}{2}\right) \rho U^2 \quad (26)$$

where C_D is the drag coefficient, A , cross sectional area of the particle, ρ , fluid density and U is the relative velocity defined by

$$U = \sqrt{(u - \dot{x})^2 + \dot{y}^2 + \dot{z}^2} \quad (27)$$

In the above equation, u is the time averaged local velocity of air. The coefficient C_D can be given as a function of the Reynolds number Ud/ν , formulas of which have been proposed

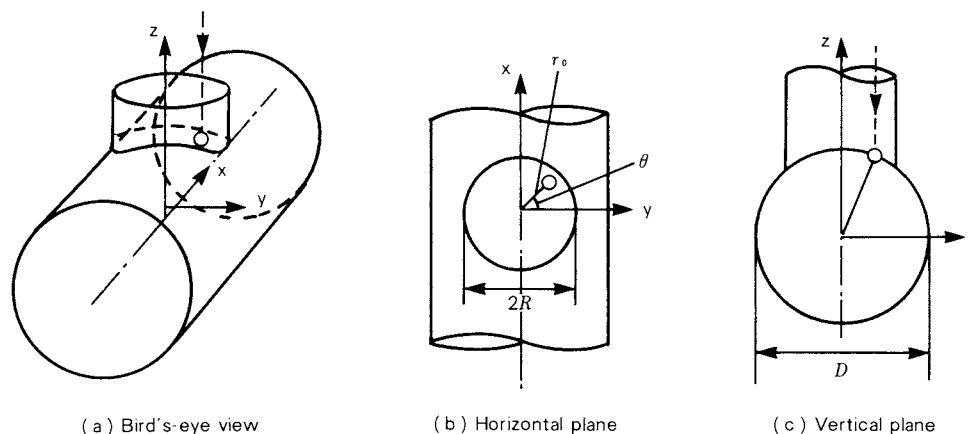


Fig. 4 Coordinate system

by many workers.

Next, let us consider the lift force due to the particle rotation. Collision of a particle against the wall causes the particle to rotate at a considerably high rate of rotation, for instance, $10^3 \sim 10^4$ rad/sec in the case of a coarse particle, which was confirmed in an experiment by Matsumoto, et al.⁹⁾. Therefore calculated trajectories are different whether the particle rotation is taken into account or not. When a particle rotates with translational velocity U as shown in Fig. 5, the magnitude of the lift force is expressed as

$$|F_L| = C_L A \left(\frac{1}{2}\right) \rho U^2 \quad (28)$$

where C_L is the lift coefficient given as a function of the velocity ratio σ ,

$$\sigma = a \omega / U \quad (29)$$

The following equations are assumed for the relation between C_L and σ ,

$$C_L = \begin{cases} 0.5 \sigma & (\sigma \leq 1.0) \\ 0.5 & (\sigma > 1.0) \end{cases} \quad (30)$$

by referring to the results of Maccol¹⁰⁾. The vector U of the relative velocity as well as ω has three components of x , y and z directions, but taking all the components is so complicated that the following approximation is used. For the relative velocity, only one component

$$U = (u - \dot{x}) i \quad (31)$$

is considered. The vector of angular velocity ω is given as

$$\omega = \omega_y j + \omega_z k \quad (32)$$

This suggests that the lift force is assumed to be applied only in the (y, z) plane.

As a result of the above approximation, the magnitude of the lift and velocity ratio σ can

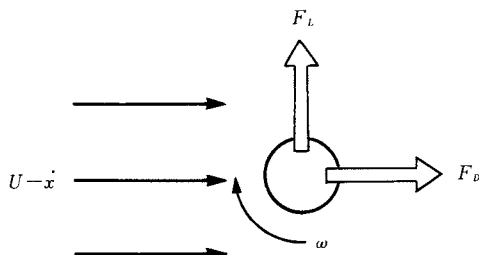


Fig. 5 Lift due to particle rotation

be written as

$$|F_L| = C_L \pi a^2 \left(\frac{1}{2}\right) \rho (u - \dot{x})^2 \quad (33)$$

$$\sigma = \frac{|\omega_y j + \omega_z k| a}{(u - \dot{x})} \quad (34)$$

The direction of the lift force agrees with that of $U \times \omega$, and therefore the vector of lift is given by

$$F_L = |F_L| e_y j + |F_L| e_z k \quad (35)$$

where

$$e = e_y j + e_z k \quad (36)$$

$$e_y = \frac{(u - \dot{x}) \omega_z}{|u - \dot{x}| \sqrt{\omega_y^2 + \omega_z^2}} \quad (37)$$

$$e_z = \frac{(u - \dot{x}) \omega_y}{|u - \dot{x}| \sqrt{\omega_y^2 + \omega_z^2}} \quad (38)$$

By substituting Eq. (33) into Eq. (35), each component of lift becomes

$$\left. \begin{aligned} F_{Lx} &= 0 \\ F_{Ly} &= C_{Ly} k M (u - \dot{x})^2 \\ F_{Lz} &= C_{Lz} k M (u - \dot{x})^2 \end{aligned} \right\} \quad (39)$$

where

$$k = 3\rho / (4\rho_s d) \quad (40)$$

$$\left. \begin{aligned} C_{Ly} &= C_L e_y \\ C_{Lz} &= C_L e_z \end{aligned} \right\} \quad (41)$$

The gravity force F_G is given by

$$F_G = -g M k \quad (42)$$

Finally, one obtains the equations of motion in the following form.

$$\begin{pmatrix} \ddot{x} \\ \ddot{y} \\ \ddot{z} \end{pmatrix} = \begin{pmatrix} k C_D U (u - \dot{x}) \\ -k C_D U \dot{y} \\ -k C_D U \dot{z} \end{pmatrix} + \begin{pmatrix} 0 \\ k C_{Ly} (u - \dot{x}) \\ k C_{Lz} (u - \dot{x}) \end{pmatrix} + \begin{pmatrix} 0 \\ 0 \\ -g \end{pmatrix} \quad (43)$$

5. 3 Pressure drop

If the purpose of the present simulation were to obtain only the particle trajectories, it would not be of value from the viewpoint of industry, because what design workers really want to know is the pressure drop rather than the particle trajectories. The pressure drop can

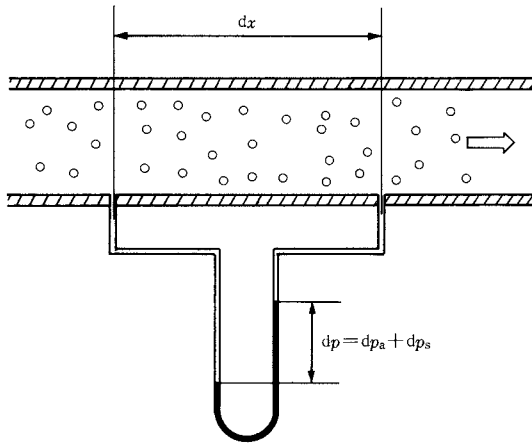


Fig. 6 Pressure drop in the region dx

be calculated by the momentum theorem as described below.

Consider the region dx shown in Fig. 6, where dx is the distance that particles travel during the time period dt , i.e.

$$dx = \dot{x} dt \quad (44)$$

The total pressure drop which occurs in the region dx is assumed to be the sum of the pressure drop due to air, dp_a , and the additional one, dp_s .

$$dp = dp_a + dp_s \quad (45)$$

We can use some empirical equations such as Blasius' or Plandtl's formula to estimate the pressure drop dp_a . The pressure drop dp_s is caused by the drag force exerted by fluid on particles. Hence, the equation of momentum balance in the region dx becomes

$$dp_s S = -F_{Dx} N \quad (46)$$

where S is the cross sectional area of the pipe and N is the number of particles contained in the region dx . Definition of the mass flow ratio of particle to air gives

$$m = \frac{MN}{S\bar{u}dt} \quad (47)$$

Substituting the expression of the drag force and Eq. (47) into Eq. (46), one obtains

$$\frac{dp_s}{dt} = -k\rho\bar{u}C_D U(u - \dot{x})m \quad (48)$$

Trajectories and pressure distributions are obtained by integrating Eqs. (43) and (48) simultaneously. In order to make the averaged dp_s

converge to a certain value, calculations must be made for many particles with different initial conditions.

5. 4 Change in particle rotation due to viscous dissipation

First, the authors explain the reason to consider the viscous dissipation for particle rotation. As was mentioned before, particles conveyed in the pipe rotate at high angular velocities. Obviously, the increase in the angular velocity is limited to a certain level in actual pneumatic conveying; however when a factor which suppresses the rotation is not considered in the simulation, the angular velocity continuously increases along the flow owing to repeated collision against the wall. This tendency is marked particularly when the particle-wall collision takes place in the lower half of the pipe section. As shown in Section 3, the longitudinal velocity after the collision is influenced by the rotation before the collision. In the simulation where a factor of the dissipation is ignored, the longitudinal velocity increases with increasing rotation so that the relative velocity between the air and particle decreases. As a result, calculated pressure drops become smaller than measurements at a point far from the feeder.

In order to avoid the above contradiction, viscous dissipation is estimated by using the result obtained by Dennis et al.¹¹⁾,

$$I\dot{\omega} = -T$$

$$T = \frac{1}{2}\rho_a a^5 \omega^2 (6.45 R^{-1/2} + 32.1 R^{-1}) \quad (49)$$

where T is the torque exerted on the rotating particle and R is the Reynolds number defined by $a^2\omega/\nu$. When the dissipation is taken into consideration, the angular velocity settles asymptotically to a certain value as shown later.

5. 5 Abnormal bouncing of particle against the wall

What are necessary for the simulation are almost explained in the foregoing section except for one thing that is "abnormal bouncing". If a spherical particle repeats bouncing motion according to the relationship shown in Table 2, the height of the particle rebounded from the wall gradually decreases and it can not rebound

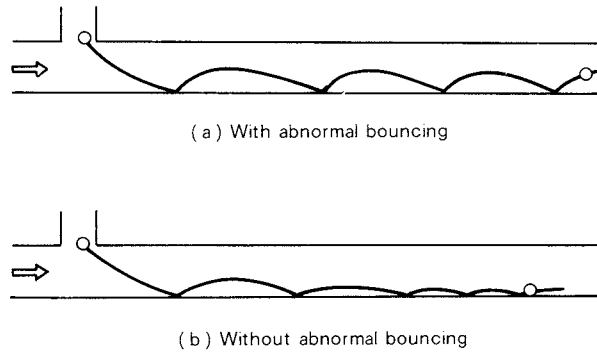


Fig. 7 Bouncing motion in the pipe

at last even at a high velocity of air, as shown in Fig. 7(b). For a practical pneumatic conveying, however, one finds that particles repeat bouncing motion steadily as shown in Fig. 7(a). At least for large particles, the Magnus force, air turbulence and lift force due to velocity shear can not be the causes which prevent the particles from settling on the bottom wall. The reason why the particles continue the bouncing motion in a long horizontal pipe is that the normal component of the velocity of the particle rebounded from the wall does not diminish. Such bouncing motion is defined as abnormal bouncing in this paper.

There have been several models describing the abnormal bouncing proposed, for example, the pipe wall has a slight roughness¹²⁾ or particle shape deviates from that of a sphere. In the present work, the authors propose newly a virtual wall model. This model states that when the incidence angle becomes smaller than a certain value, the wall is replaced by a virtual one with the angle α against the true wall, as shown in Fig. 8. The velocity after collision with this virtual wall must be determined by the impulsive equations, the results of which are shown in Table 2. In this model, the energy conservation principle holds. Although the particle gains more energy in the normal direction, it loses much more energy in the longitudinal direction due to the collision against the inclined wall.

The relation between the angle α and incidence angle θ is assumed as

$$\begin{aligned} \alpha &= -\delta(\theta - \beta), \quad (\theta \leq \beta) \\ \alpha &= 0, \quad (\theta > \beta) \end{aligned} \quad (50)$$

This model was qualitatively justified by the experiment of the particle bouncing on a rotat-

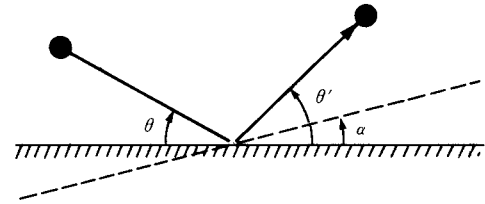


Fig. 8 Virtual wall model of abnormal bouncing

ing disc¹³⁾. It is further assumed that the virtual wall makes an angle against the tangential plane of the pipe wall. The angle γ , which is called “yaw angle” in this paper, varies in the range

$$-\gamma_0 \leq \gamma \leq \gamma_0 \quad (51)$$

and the value of γ is given by random numbers. The reason why the yaw angle is needed is that without a randomness due to the yaw angle particles tend to concentrate on the same vertical line in a long pipe and so particle distribution becomes unrealistic.

The next step is to determine the parameters β , δ and γ_0 . These parameters were determined in a purely empirical way at the present stage of analysis. What the authors aim at in the present simulation is to explain satisfactorily all the quantities such as translational particle velocity, angular velocity, particle distribution and pressure drop. Good agreements between simulation and experiment can be obtained by choosing proper values of β , δ and γ_0 . However, it is almost impossible to adjust the parameters to every possible condition of conveying. Hence the values of parameters were determined empirically by comparing simulated results with test data. The same parameter were applied to other cases under different conditions. The experiment to determine the parameters was made under the following conditions:

- Pipe diameter $D = 42$ mm
- Bulk air velocity $\bar{u} = 7 \sim 20$ m/s
- Particle diameter $d = 1.1$ mm
- Particle density $\rho_s = 923$ kg/m³ (polyethylene)
- Mass flow ratio $m < 10$

The values given by Eq. (21) were used for the coefficients of restitution and kinetic friction. The parameters determined finally are

$$\left. \begin{aligned} \beta &= 7^\circ \\ \delta &= 2.3/F_r - 91/F_r^2 + 1238/F_r^3 \\ \gamma &= 10^\circ \end{aligned} \right\} \quad (52)$$

where F_r is defined as $F_r = \bar{u}/\sqrt{gD}$.

6. Results

6. 1 Particle trajectory

Particle trajectories calculated for polyethylene pellets with 1.1 mm and 50 μm ($\rho_s = 923 \text{ kg/m}^3$) are presented in **Fig. 9**. It is seen in **Fig. 9** that a particle constantly repeats bouncing on the wall and that a free path increases with increasing air velocity. On the other hand, the particle with 50 μm does not show the bouncing motion or if any, it bounces with very short steps. At a high air velocity it does not touch the wall within the distance shown in **Fig. 9**. This means that abnormal bouncing is not enough to make a small particle suspended in the horizontal flow. Diffusion due to air turbulence must be taken into account in order to avoid such contradiction. The minimum size of particle with the density of the order 10^3 kg/m^3 to which the present simulation is applicable is about 0.5 mm.

6. 2 Particle distribution and angular velocity

Figure 10 presents particle distributions at various longitudinal sections. The Magnus lift force is taken into account in **Fig. 10 (b)**, while it is not in **Fig. 10 (a)**. The results of **Fig. 10 (b)** are more realistic than those of **Fig. 10 (a)**. However, one should notice that the Magnus force is not only the factor to give a good agreement with experimental distributions, because the calculated distribution is easily changed by the parameter β , δ and γ_0 . What is meant in **Fig. 10** is that the Magnus force clearly affects the particle distribution even for large particle although it is not enough to make the particles being suspended.

To show the state of distribution quantitatively, the pipe section is divided into 24 sub-sections as shown in **Fig. 11**, and the height of the distribution center is defined by

$$Z_g = \frac{1}{D} \frac{\sum_{i=1}^{24} f_i z'_{gi}}{\sum_{i=1}^{24} f_i} \quad (53)$$

where f_i is the number of particles contained in the i th divided section and z'_{gi} is the height of gravity center of the i th sub-section measured from the bottom line y' . Variations of Z_g along the pipeline are shown in **Fig. 12** in which plotted points represent the results of

the simulation and three curves represent measurements. It is found that agreements between the simulations and experiments are satisfactory, although there are some differences observed if one compares the results in detail.

Figure 13 indicates that the angular velocity settles at an asymptotic value owing to viscous dissipation of particle rotation.

6. 3 Pressure drop

As mentioned before, the authors place a priority of this work on predicting the pressure drop, because the pressure drop has been always investigated as a central subject for pneumatic conveying. Many workers have been seeking a similarity law of the pressure drop like that of the single phase flow. Generally, the situation in the two-phase flows is so complicated that it is hard to establish the similarity law to the same preciseness as the single phase flow. However it has been found¹⁵⁾ that the following coefficient λ_s plotted against the Froude number $F_r^* = c/\sqrt{gD}$ provides a comparatively good similarity in the pressure drop data of coarse particles.

$$\frac{dp_s}{dx} = \frac{\lambda_s}{D} \left(\frac{1}{2}\right) \rho_{ds} c^2 \quad (54)$$

where ρ_{ds} is the dispersed density of the particles. Hence the results of pressure drops are shown in the form of λ_s vs F_r^* in this paper.

The values of λ_s are indicated in **Fig. 14** where plotted points represent the simulated result and the dashed curves show the range of corresponding measurements. It is seen that agreement between them is fairly good.

All the foregoing results are limited to the condition that the particle diameter is 1.1 mm and the pipe diameter is 52 or 42 mm. The results predicted by the simulation are presented in the following section, where the effects of various factors such as particle and pipe diameters and particle density are shown. The following results are mainly described about the coefficient of the additional pressure drop λ_s .

6. 4 Effects of particle and pipe diameters

Figure 15 shows the relation between λ_s and F_r^* calculated for various particle sizes. The

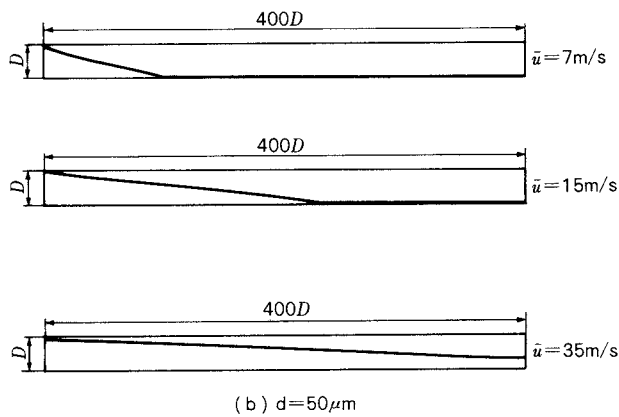
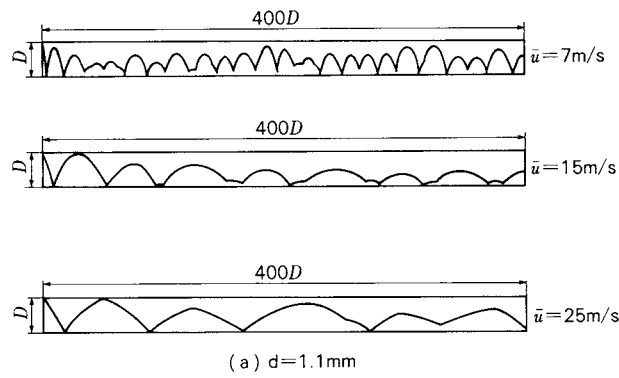


Fig. 9 Particle trajectory ($D = 52 \text{ mm}$, $\rho_s = 923 \text{ kg/m}^3$)

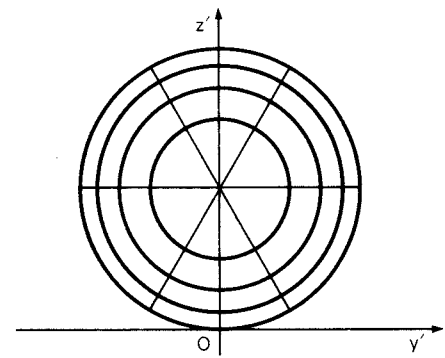


Fig. 11 Cross section of the pipe

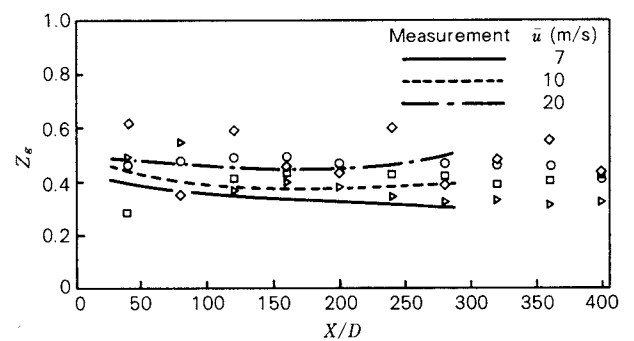


Fig. 12 Variation of distribution centre ($d = 1.1 \text{ mm}$, $D = 42 \text{ mm}$, $\rho_s = 923 \text{ kg/m}^3$, \square ; $\bar{u} = 7 \text{ m/s}$, \circ ; $\bar{u} = 10 \text{ m/s}$, \triangleright ; $\bar{u} = 15 \text{ m/s}$, \diamond ; $\bar{u} = 27 \text{ m/s}$)

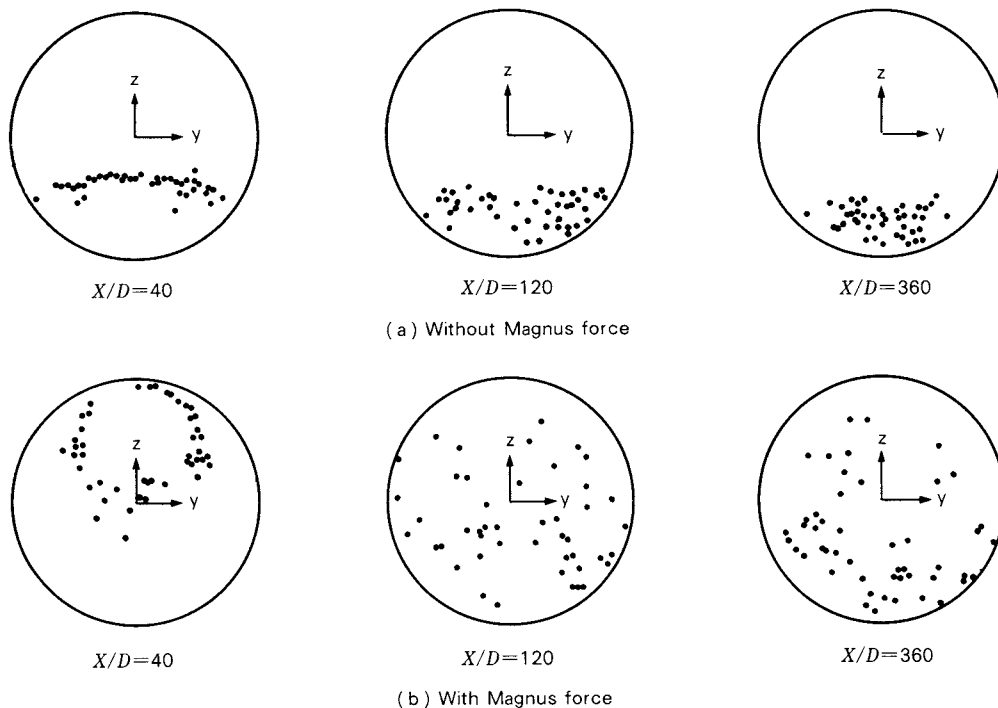


Fig. 10 Particle distribution ($d = 1.1 \text{ mm}$, $D = 52 \text{ mm}$, $\rho_s = 923 \text{ kg/m}^3$, $\bar{u} = 20 \text{ m/s}$)

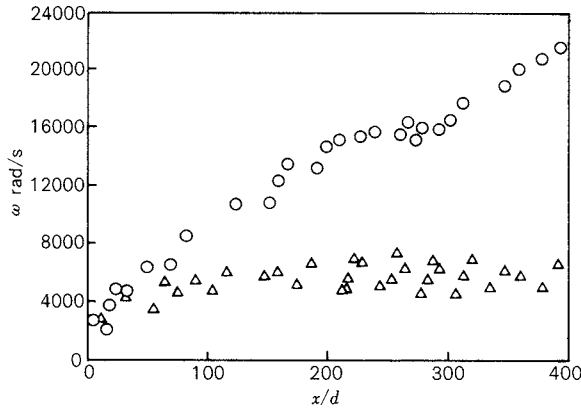


Fig. 13 Variation of angular velocity ($d = 1.1$ mm, $D = 42$ mm, $\rho_s = 923$ kg/m³, $\bar{u} = 10$ m/s)
 \circ ; Without viscous dissipation,
 \triangle ; With viscous dissipation

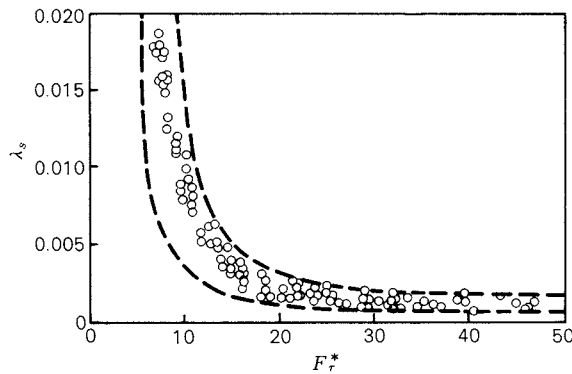


Fig. 14 Relation of λ_s vs. F_r^* ($d = 1.1$ mm, $D = 42$ mm, $\rho_s = 923$ kg/m³)

dashed curves given for comparison are the same ones that are shown in Fig. 14. The results of the simulation are within the range between the curves. As the particle size becomes larger, the calculated results tend to deviate from the range of the curves.

The effects of the pipe diameter are shown in Fig. 16, under the condition that pipe diameters are considerably different. Although the difference of the diameters of the two pipes with 27 and 200 mm is about one figure, the simulation indicates that there is little influence of the pipe diameter on the relation of λ_s and F_r^* . As mentioned before, the pressure drop data plotted in the form of λ_s and F_r^* showed a comparatively good similarity. The present results support such an experimental fact to some extent.

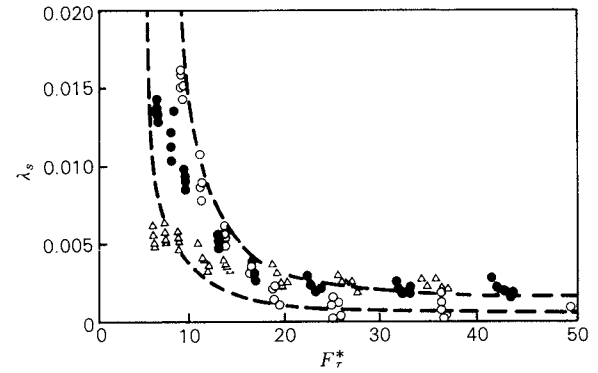


Fig. 15 Relation of λ_s vs. F_r^* ($D = 52$ mm, $\rho_s = 923$ kg/m³) \circ ; $d = 0.5$ mm, \bullet ; $d = 2$ mm, \triangle ; $d = 5$ mm

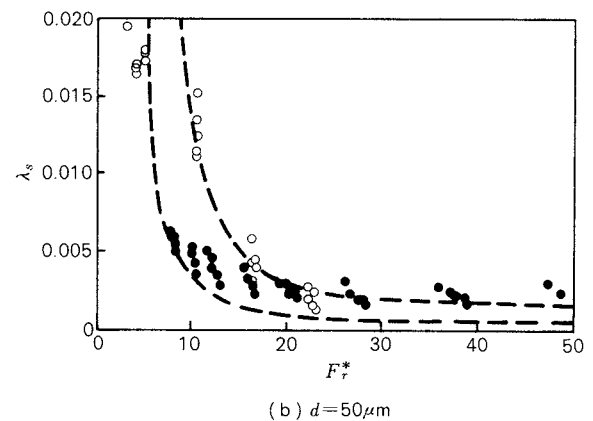
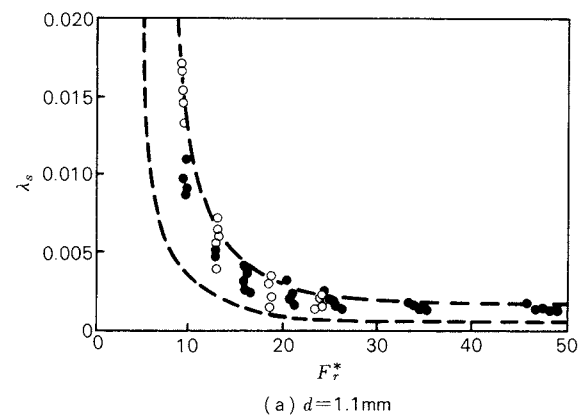


Fig. 16 Relation of λ_s vs. F_r^* ($\rho_s = 923$ kg/m³) \bullet ; $D = 27$ mm, \circ ; $D = 200$ mm

6. 5 Effects of particle density and kinetic friction

Results of the cases of $\rho_s = 500$ kg/m³ and 2500 kg/m³ are compared to see the effects of particle density. Figure 17 shows the variation of particle to air velocity ratios. The particle and pipe diameters used are 1.1 and 52 mm,

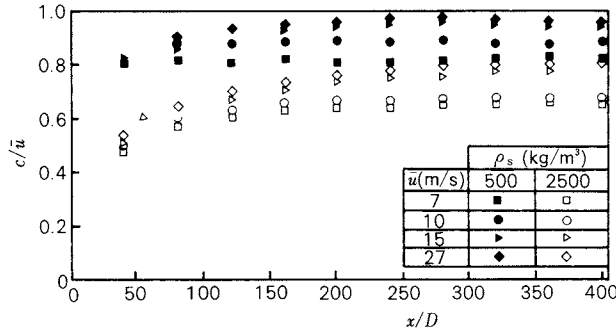


Fig. 17 Variation of velocity ratio ($d = 1.1$ mm, $D = 52$ mm)

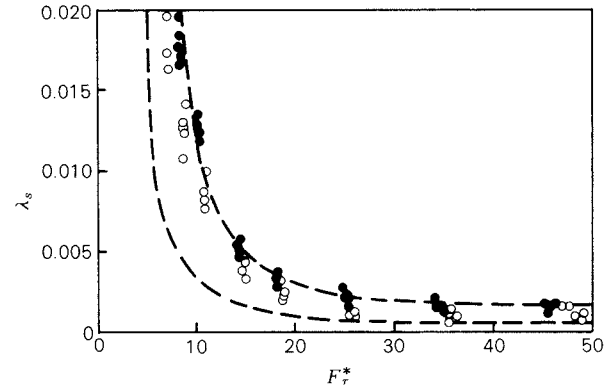


Fig. 19 Relation of λ_s vs. F_r^* ($d = 1.1$ mm, $D = 52$ mm, $\rho_s = 923$ kg/m³) ●; $f = 0.5$, ○; $f = 0.4$

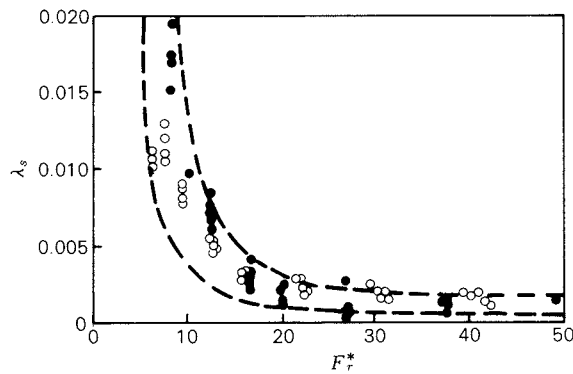


Fig. 18 Relation of λ_s vs. F_r^* ($d = 1.1$ mm, $D = 52$ mm) ●; $\rho_s = 500$ kg/m³, ○; $\rho_s = 2500$ kg/m³

respectively. As is expected, velocities of heavy particles are much smaller than those of light particles.

The relation of λ_s and F_r^* is shown in Fig. 18. Most of the calculated points are included in the region between the dashed curves. This result also means again that λ_s vs. F_r^* plot produces a good similarity. If the coefficient of pressure drop defined by

$$\frac{dp_s}{dx} = m \frac{\lambda'_s}{D} \frac{1}{2} \rho \bar{u}^2 \quad (54)$$

are plotted against the Froude number $F_r = \bar{u}/\sqrt{gD}$, as has been done previously¹⁶⁾ the results do not show a similar relation. The coefficient λ'_s of heavy particles becomes larger than that of light particles for the same value of F_r .

Figure 19 shows the effects of friction coefficient f on the relation of λ_s and F_r^* . It is found that the higher value of f (for instance $f = 0.5$) gives slightly higher values of λ_s for the same F_r^* .

7. Conclusion

Trajectories and pressure drop coefficient in pneumatic conveying for large spherical particles could be predicted successfully by the present simulation.

Nomenclature

a	: particle radius	[m]
A	: projected cross sectional area of a particle	[m ²]
c	: mean particle velocity	[m/s]
C_D	: drag coefficient	[—]
C_L	: lift coefficient	[—]
d	: particle diameter	[m]
D	: pipe diameter	[m]
e	: coefficient of restitution	[—]
f	: coefficient of kinetic friction	[—]
F_r^*	: Froude number, c/\sqrt{gD}	[—]
F_r	: Froude number, \bar{u}/\sqrt{gD}	[—]
g	: gravitational constant	[m/s ²]
I	: moment of inertia about the axis of diameter, $Md^2/10$	[kg m ²]
J	: impulse vector, (J_X, J_Y, J_Z)	[kg·m/s]
k	: constant, $3\rho/(4\rho_s d)$	[1/m]
m	: particle to air mass flow ratio	[—]
M	: particle mass, $\pi d^3 \rho_s/6$	[kg]
dp	: pressure drop	[Pa]
dp_a	: pressure drop due to air	[Pa]
dp_s	: pressure drop due to particles	[Pa]
u	: local mean velocity of air	[m/s]
\bar{u}	: bulk air velocity	[m/s]
V	: vector of translation velocity, (V_X, V_Y, V_Z)	[m/s]
x, y, z	: coordinates shown in Fig. 4	[m]
X, Y, Z	: coordinates shown in Fig. 1	[m]
Z_g	: height of distribution center defined by Eq. (53)	[—]
α	: angle between a virtual and true walls	[°]

β	: angle below which abnormal bouncing is taken into consideration	[°]
γ	: yaw angle	[°]
δ	: parameter of the abnormal bouncing model	[-]
λ_s	: coefficient of additional pressure drop	[-]
ρ	: density of air	[kg/m ³]
ρ_s	: density of particle	[kg/m ³]
ρ_{ds}	: dispersed density of particles	[kg/m ³]
ω	: vector of angular velocity, ($\omega_X, \omega_Y, \omega_Z$)	[rad/s]

Suffix

(0)	: value before collision
\wedge	: value at the end of compression period (beginning of recovery period)
n	: normal component
(r)	: value in the period after the period (s)
(s)	: value in the period during which a particle sides
t	: tangential component

References

- 1) Weber, M.: "Stromungsfordertechnik", Krausskopf-Verlag, Mainz (1974).
- 2) Tsuji, Y. and Y. Morikawa: *J. Fluid Mech.*, **120**, 385 (1982).
- 3) Tsuji, Y., Y. Morikawa and H. Shiomi: *J. Fluid Mech.*, **139**, 417 (1984).
- 4) Crowe, C. T.: *J. Fluids Engineering*, **104**, 297 (1982).
- 5) Tsuji, Y. and Y. Morikawa: *Proc. Pneumotransport*, **4**, Paper B1, BHRA, Cranfield, England, (1978).
- 6) Brauer, H.: *Powder & Bulk Solids Technology*, **4**, 3 (1980).
- 7) Yamamoto, A.: *Thesis M.E. Osaka University*, (1974) (in Japanese).
- 8) Zenz, F. A. and D. F. Othmer: "Fluidization and fluid-particle systems", Reinhold, New York, 140 (1960).
- 9) Matsumoto, S. and S. Saito: *J. Chem. Eng. Japan*, **3**, 83 (1970).
- 10) Maccoll, J.H.: *J. Roy. Aero. Soc.*, **32**, 777 (1928).
- 11) Dennis, S.C.R., S.N. Singh and D.B. Ingham: *J. Fluid Mech.*, **101**, 257 (1980).
- 12) Matsumoto, S. and S. Saito: *J. Chem. Eng. Japan*, **3**, 223 (1970).
- 13) Muschelknautz, E.: *VDI-Forsch.-Heft*, 476 (1959).
- 14) Takegawa, T. et al.: *Trans. Japan Soc. Mech. Engrs.*, **44**, 4225 (1978) (in Japanese).
- 15) Welschhof, G.: *VDI-Forsch.-Heft* 492 (1962).
- 16) Boothroyd, R.G.: "Flowing gas-solids suspensions", Chapman & Hall, London, 141 (1971).

Simulation of Moving Granular-Bed Type Heat Exchanger[†]

Tadayuki Minoura and Shun-ichi Mizukami

*Mechanical Engineering Research Laboratory
Kobe Steel, Ltd.**

Hiroyuki Kohama

*Chemical Industry Research Laboratory
Kobe Steel, Ltd.**

Takayoshi Asami

*Engineering Division
Kobe Steel, Ltd.**

Abstract

A simulation of the moving granular-bed type heat exchanger, in which heat is transferred from the hot gas through granular materials and heat pipes to the cold gas, has been performed. A numerical simulation model was made by dividing each part of the heat exchanger into small elements, and heat balance was calculated using the finite difference method. The heat transfer coefficients and effective thermal conductivities of the granular bed in each part of the heat exchanger were estimated from a general theory, while the heat transfer coefficient between the granular bed and heat pipes was determined from the experiment.

The steady characteristics of the heat exchanger from the calculations were compared with the data obtained from the experiment. The calculation results coincided well with the experimental results. The method of modeling and simulation was confirmed to be accurately applicable to the estimation of the performance of the heat exchanger using granules as heat transferring media and heat pipes.

1. Introduction

Various types of heat exchangers consisting of heat pipes combined with a fluidized bed or a packed bed have been proposed. Since 1976, our company has been engaged in research and development on "A Moving Granular-Bed Type Heat Exchanger", which consists of corrosion-resisting heat pipes combined with a moving granular-bed type dust collector, as one of the research contracts on a large-scale project entitled "Research and Development of Technical

Systems for Utilization of Waste Heat" sponsored by the Agency of Industrial Science and Technology of the Ministry of International Trade and Industry. In the moving granular-bed type heat exchanger, heat is transferred through the heat pipes with a moving bed as a heat carrier. In the present research, we performed a simulation, solving the fundamental equations obtained through modeling a moving granular-bed type heat exchanger by the finite difference method in order to evaluate the thermal efficiency of the heat exchanger. Furthermore, a comparison of the calculation results with the experimental ones showed that the constants used for the simulation, such as heat transfer coefficients, are appropriate in addition to the propriety of the proposed model.

* 1-chome, Wakinocho, Chuo-ku, Kobe, 651
TEL. 078 (251) 1551

† This report was originally printed in *J. Soc. Powder Tech., Japan*, 20, 185-193 (1983) in Japanese, before being translated into English with the permission of the editorial committee of the Soc. Powder Tech., Japan.

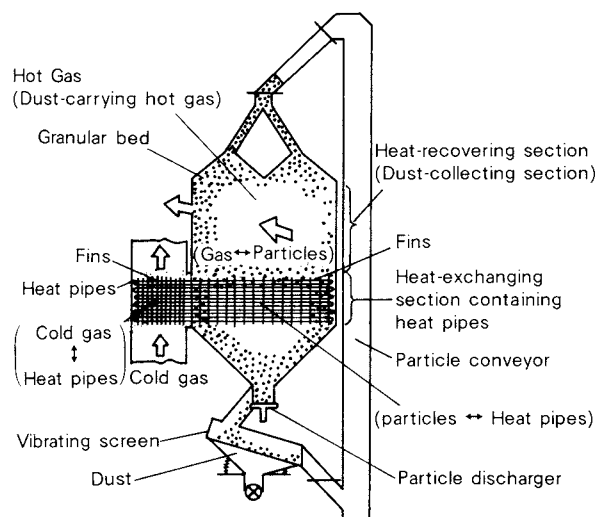


Fig. 1 Principle of moving granular-bed type heat exchanger

2. Operational principle of moving granular-bed type heat exchanger

The moving granular bed is, as shown in Fig. 1, so designed that the heat is exchanged between the hot and the cold gases through particles as a heat carrier. Namely at first, in the heat-recovering section, heat is transferred from the hot gas to the particles when it flows through the granular bed. The particles, having received heat from the hot gas, move downward due to gravitational force toward a constant discharger. In the heat-exchanging section containing the heat pipes, heat is transferred from the particles to the cold gas through heat pipes and is recovered for further utilization.

3. Modeling

3. 1 Fundamental equations

In order to simplify the complicated heat transferring phenomena in the moving granular-bed type heat exchanger, the following assumptions are made regarding the simulation model shown in Fig. 2.

- The particles move downward in the tower at a constant velocity in the z -direction.
- The hot gas flows through the granular bed cross-currently to the movement of the particles and diffusion of the hot gas in the z -direction is negligible.
- In the heat-recovering section, temperature distribution in the granular bed is two-dimen-

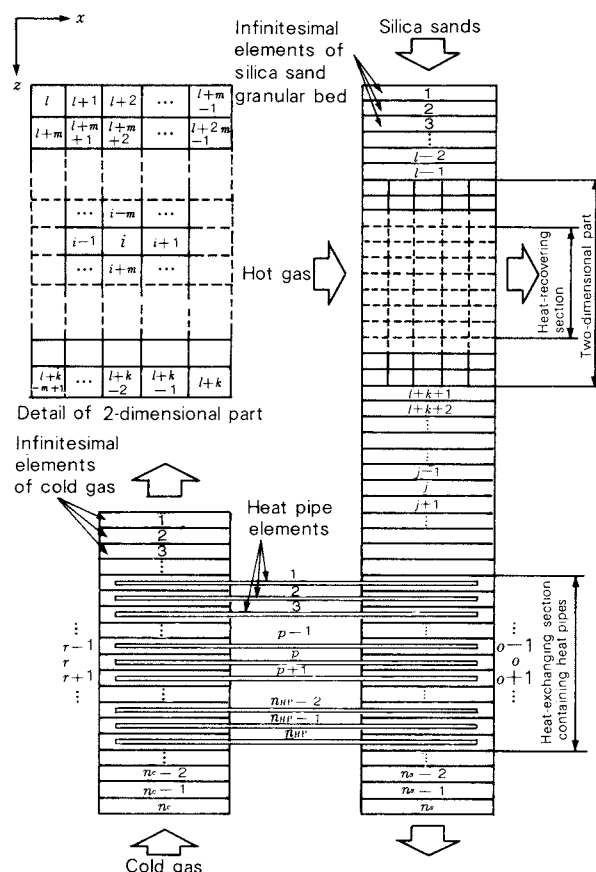


Fig. 2 A Model for simulation of the heat exchanger

sional, i.e. in the directions of particle movement and hot gas flow. In some parts of the upper and lower parts of the heat-recovering section, however, it can be regarded as one-dimensional, neglecting the variation in the x -direction.

- In the heat-exchanging section of the heat pipes, the temperature of the granular bed in the x -direction is regarded to be uniform.
- The temperature inside the particles is uniform[☆].
- The heat pipes in the same row have the same temperature.

The heat resistance of these heat pipes them-

[☆] The particles used in the present research (Silica Sands having a mean diameter of 1.75 mm, thermal conductivity of 1.16 W/m°C, specific heat of 0.921 kJ/kg°C, density of 2620 kg/m³) has a Biot number of 0.0035, when it is set in a fluid flow under the assumption of spherical particles having uniform temperature and a heat transfer coefficient of 0.465 W/m²°C having the same order of that between the hot gas and the granular bed. In this way, the temperature distribution within the particles can be regarded as uniform, since the temperature difference between the surface and the center of the particles is always less than 1% of that between the particle center and the fluid¹⁾.

selves is negligibly small compared with that between the heat pipes and the particles as well as that between the heat pipes and the cold gas^{*}.

(g) Conductive heat transfer of the hot gas in the z - and x - directions is negligible.

With the above-mentioned assumptions, heat balances produce the following equations. Regarding the hot gas in the heat-recovering section,

$$\begin{aligned} \rho_h u_h c_h \frac{\partial T_h}{\partial x} + a_s h_{hs} (T_h - T_s) \\ + a_{hw} U_{hw} (T_h - T_a) = 0 \end{aligned} \quad (1)$$

Regarding the granular bed in the heat-recovering section,

$$\begin{aligned} k_{sII} \frac{\partial^2 T_s}{\partial z^2} + k_{sII} \frac{\partial^2 T_s}{\partial x^2} - \rho_s \epsilon_s u_s c_s \frac{\partial T_s}{\partial z} + q_s \\ - a_{sw} U_{sw} (T_h - T_a) = 0 \end{aligned} \quad (2)$$

Though q_s in Eq. (2) is equivalent to the second term of Eq. (1), they are written in different ways because of independent numerical calculations of T_s and T_h , as described later. For the granular bed in the heat-exchanging section including heat pipes,

$$\begin{aligned} k_{sI} \frac{\partial^2 T_s}{\partial z^2} - \rho_s \epsilon_s u_s c_s \frac{\partial T_s}{\partial z} - a_{sHP} h_{sHP} (T_s - T_{HP}) \\ - a_{sw} U_{sw} (T_s - T_a) = 0 \end{aligned} \quad (3)$$

For the heat pipe elements,

$$\begin{aligned} a_{sHP} V_s h_{sHP} (T_s - T_{HP}) \\ - a_{cHP} V_c h_{cHP} (T_{HP} - T_c) = 0 \end{aligned} \quad (4)$$

For the cold gas in the heat-exchanging section including heat pipes,

$$\begin{aligned} k_c \frac{\partial^2 T_c}{\partial z^2} + \rho_c u_c c_c \frac{\partial T_c}{\partial z} + a_{cHP} h_{cHP} (T_{HP} - T_c) \\ - a_{cw} U_{cw} (T_c - T_a) = 0 \end{aligned} \quad (5)$$

* The temperature difference at both ends of the heat pipes of the experimental apparatus for the simulation can be estimated to be 1.5°C from the transferred heat of about 174.5 W per each heat pipe and the total thermal resistance of about 10⁻² °C/W. The difference in temperature at the both ends of the heat pipes with small thermal resistance can be neglected, since the temperature difference between the heat pipes and the granular bed as well as that between the heat pipes and the cold gas are in the range of 10 to 15°C.

The boundary conditions are set to be as follows:

$$\text{At the inlet of particles: } T_s = T_{si}, \frac{\partial T_s}{\partial z} = 0 \quad (6)$$

$$\text{At the inlet of the hot gas: } T_h = T_{hi} \quad (7)$$

$$\text{At the inlet of the cold gas: } T_c = T_{ci} \quad (8)$$

3. 2 Estimation of heat transfer coefficient

The following equations were applied to estimate heat transfer coefficients for the simulation.

(a) Heat transfer coefficient between the hot gas and the granular bed

In order to estimate this, the following equation for the heat transfer coefficient between the particles and the fluid flowing through the fixed-bed was used²⁾:

$$\frac{h_{hs} d_p}{k_h} = 2.0 + 1.8 P_r^{1/3} R_{ep}^{1/2} (P_r R_{ep} > 10^2) \quad (9)$$

Additionally, the measured values shown in Kunii's "Thermal Unit Operation (I)" were expressed by the following equation:

$$\frac{h_{hs} d_p}{k_h} = 10^{[1.33 \log(P_r R_{ep}) - 1.67]} (P_r R_{ep} \leq 10^2) \quad (10)$$

where

$$R_{ep} = \frac{\rho_h u_o d_p}{\mu_h}$$

(b) Effective thermal conductivity of the granular bed

For the calculation of effective thermal conductivity of the fixed bed with fluid flow, the term caused by conduction in the solid phase k_{sII} and the ones in the fluid phase k_{hx} , k_{hz} which denote effective thermal conductivity in the parallel and vertical direction to the flow respectively, were considered separately applying the following equation:

$$\frac{k_{sII}}{k_h} = \frac{k_{sI}}{k_h} - \epsilon \quad (11)$$

The effective thermal conductivity of the fixed bed without fluid flow k_{sI} was calculated by the following equation²⁾:

$$\frac{k_{sI}}{k_h} = \epsilon \left(1 + \beta \frac{h_{rv} d_p}{k_h} \right)$$

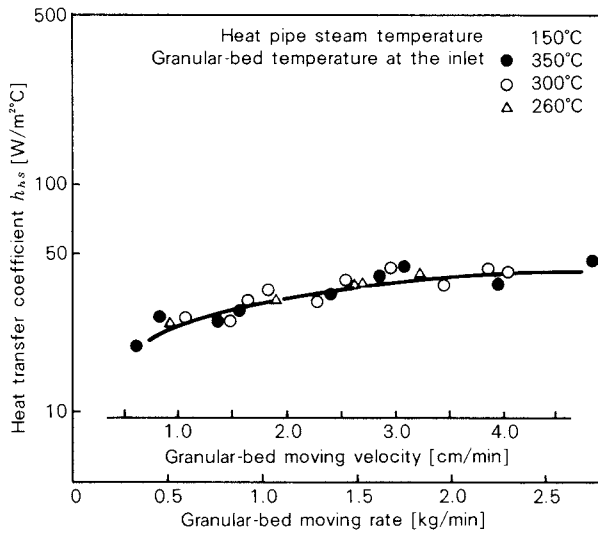


Fig. 3 Variation of the heat transfer coefficient between silica sands and heat pipes with the moving rate of silica sand granular bed

$$+ \frac{1 - \epsilon}{\frac{1}{\phi} + \frac{d_p}{k_h} (h_{rs} + h^*)} + \gamma \left(\frac{k_h}{k_s} \right) \quad (12)$$

The heat transfer by conduction of the hot gas to be determined with k_{hx} , k_{hz} ,

$$k_{hx} = c_h \rho_h D_h \quad (13)$$

$$k_{hz} = k_h (\alpha \beta) P_r R_{ep} + \epsilon k_h \quad (14)$$

was neglected according to the assumption(g).

(c) Heat transfer coefficient between the granular bed and the heat pipes

This coefficient was obtained from the experiments described in the Appendix, the results of which, shown in Fig. 3, were used for the simulation.

(d) Heat transfer coefficient between the heat pipes and the cold gas

The heat transfer coefficient in the case where fluid flows vertically to the pipes with fins was calculated by the following equation³⁾.

$$\begin{aligned} \frac{h_{cHP} D_e}{k_c} &= 0.251 \left(\frac{D_e G_{max}}{\mu_c} \right)^{0.67} \left(\frac{S_1 - D_r}{D_r} \right)^{-0.2} \\ &\quad \times \left(\frac{S_1 - D_r}{Y} + 1 \right)^{-0.2} \left(\frac{S_1 - D_r}{S_2 - D_r} \right)^{0.4} \\ D_e &= \frac{A_r D_r + A_r \sqrt{A_f / (2n_f)}}{A_r + A_f} \end{aligned} \quad (15)$$

4. Numerical analysis method

The fundamental equations concerning the heat transfer in a moving granular-bed have been solved differently in a large number of reports since the research by Amundson⁴⁾. Lately, as a result of the remarkable spread of computers, numerical analysis has come to be a principal method and has made the consideration of complicated shapes and detailed boundary conditions possible. As the heat exchanger concerned in our present work has heat-recovering and heat-exchanging parts which have different mechanisms of heat transfer, we have developed original procedures and methods for numerical calculation based on the finite difference method corresponding to each mechanism.

4. 1 Division into infinitesimal elements and difference equations⁵⁾

As mentioned above for modeling, there are two types of sections where the heat transferring mechanisms should be handled in one- or two-dimensions. Therefore, they were divided into the infinitesimal elements as shown in Fig. 2. The thermal difference equations are obtained as follows for individually numbered elements.

For the two-dimensional element i ,

$$\begin{aligned} \left(\frac{\partial T}{\partial z} \right)_i &= \frac{T(i+m) - T(i-m)}{2\Delta z} \\ \left(\frac{\partial T}{\partial x} \right)_i &= \frac{T(i+1) - T(i-1)}{2\Delta x} \\ \left(\frac{\partial^2 T}{\partial z^2} \right)_i &= \frac{T(i+m) - 2T(i) + T(i-m)}{(\Delta z)^2} \\ \left(\frac{\partial^2 T}{\partial x^2} \right)_i &= \frac{T(i+1) - 2T(i) + T(i-1)}{(\Delta x)^2} \end{aligned} \quad (16)$$

For the one-dimensional element o ,

$$\begin{aligned} \left(\frac{\partial T}{\partial z} \right)_o &= \frac{T(o+1) - T(o-1)}{2\Delta z} \\ \left(\frac{\partial^2 T}{\partial z^2} \right)_o &= \frac{T(o+1) - 2T(o) + T(o-1)}{(\Delta z)^2} \end{aligned} \quad (17)$$

When it comes to the elements on the boundary, forward and backward difference equations are applied.

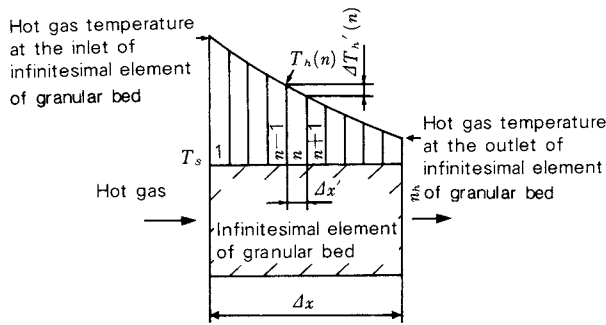


Fig. 4 Temperature distribution of the hot gas within an infinitesimal element of the granular bed

4. 2 Difference equations for the two-dimensional heat-recovering section

(a) Determination of hot gas temperature

Near the inlet of the particles and the hot gas into the heat-recovering section, the temperature gradient of the hot gas in the x -direction is extremely steep. Therefore, the hot gas temperature was obtained by solving Eq. (1), for each infinitesimal element of the granular bed independent of the temperature of the granular bed. Namely, regarding T_s to be constant in each element of the granular bed assigned in Fig. 2, Eq. (1) was modified to the following equation by dividing the elements into smaller subelements as shown in Fig. 4.

$$\Delta T_h'(n) = - \frac{1}{\rho_h u_h c_h} \left\{ a_s h_{hs} (T_h(n) - T_s) + a_{hw} U_{hw} (T_h(n) - T_a) \right\} \Delta x' \quad (18)$$

$\Delta x'$ and $\Delta T_h'(n)$ denote a length of subdivision in the x -direction within the infinitesimal element of granular bed and the temperature change of the hot gas in the n -th subdivision.

The amount of heat transferred from the hot gas to the infinitesimal element of the granular bed per unit volume is calculated by numerical integration of the following equation:

$$q_s \Delta x = - \sum_{n=1}^{nh} \rho_h u_h c_h \Delta T_h'(n) \quad (19)$$

(b) Determination of granular-bed temperature

Substituting the difference equation (16) for Eq. (2), the following difference equations are obtained for each infinitesimal element.

$$E_{s,i} T_s(i-m) + A_{s,i} T_s(i-1) + B_{s,i} T_s(i) + C_{s,i} T_s(i+1) + F_{s,i} T_s(i+m) = G_{s,i} \quad (20)$$

where $E_{s,i}$, $A_{s,i}$, $B_{s,i}$, $C_{s,i}$, $F_{s,i}$, $G_{s,i}$ are the coefficients or the constants consisting of the operational variables like velocity and of the characteristic properties such as heat transfer coefficient, specific heat and so on. The heat-balance equations concerning the infinitesimal elements of the granular bed which do not come into contact with the hot gas become difference equations of fundamentally the same form as Eq. (18), since the term of q_s drops in Eq. (1).

4. 3 Difference equations in the heat-exchanging section of heat pipes

(a) Determination of granular-bed temperature

Substituting the difference equation (17) for Eq. (3), difference equations for each infinitesimal element are obtained as below.

For the element o ,

$$A_{o,s} T_s(o-1) + B_{s,o} T_s(o) + C_{s,o} T_s(o+1) = G_{s,o} \quad (21)$$

The heat-balance equation for the infinitesimal element of the granular bed which does not exchange heat with heat pipes comes to be the difference equation having basically the same form as Eq. (21) with the term $a_{sHP} h_{sHP} (T_s - T_{HP})$ being removed in Eq. (3).

At the junction part of one- and two-dimensional sections, the average temperature of the two-dimensional infinitesimal elements, which, for example, are in contact with element $l-1$, is used as the temperature of the infinitesimal element which is in contact with element $l-1$ in the z -direction.

$$A_{s,l-1} T_s(l-2) + B_{s,l-1} T_s(l-1) + C_{s,l-1} \times \left\{ T_s(l) + T_s(l+1) + \dots + T_s(l+m-1) \right\} / m = G_{s,l-1} \quad (22)$$

A similar procedure is undertaken for the element $l+k+1$.

(b) Determination of heat pipe temperature

The reformation of Eq. (4) gives the following equation for the element p .

$$T_{HP}(p) = \frac{1}{a_{sHP} V_s h_{sHP} + a_{cHP} V_c h_{cHP}} \times (a_{sHP} V_s h_{sHP} T_s(o) + a_{cHP} V_c h_{cHP} T_c(r)) \quad (23)$$

$$\begin{aligned}
 & \left[\begin{array}{cccc} A_{s,1} & B_{s,1} & C_{s,1} & D_{s,1} \\ A_{s,2} & B_{s,2} & C_{s,2} & \\ A_{s,3} & B_{s,3} & C_{s,3} & \\ \vdots & \vdots & \vdots & \vdots \end{array} \right] \left[\begin{array}{ccccccc} E_{s,t} & A_{s,t} & B_{s,t} & C_{s,t} & D_{s,t} & F_{s,t} & \\ E_{s,t-1} & A_{s,t-1} & B_{s,t-1} & C_{s,t-1} & & F_{s,t-1} & \\ & \vdots & \vdots & \vdots & \vdots & \vdots & \vdots \\ E_{s,t-1} & A_{s,t-1} & B_{s,t-1} & C_{s,t-1} & & F_{s,t-1} & \\ E_{s,t} & A_{s,t} & B_{s,t} & C_{s,t} & & F_{s,t} & \\ E_{s,t+1} & A_{s,t+1} & B_{s,t+1} & C_{s,t+1} & & F_{s,t+1} & \\ & \vdots & \vdots & \vdots & \vdots & \vdots & \vdots \\ E_{s,t+k-1} & A_{s,t+k-1} & B_{s,t+k-1} & C_{s,t+k-1} & & F_{s,t+k-1} & \\ E_{s,t+k} & A_{s,t+k} & B_{s,t+k} & C_{s,t+k} & D_{s,t+k} & F_{s,t+k} & \\ & \vdots & \vdots & \vdots & \vdots & \vdots & \vdots \\ A_{s,ns-1} & B_{s,ns-1} & C_{s,ns-1} & & & & \\ A_{s,ns} & B_{s,ns} & C_{s,ns} & D_{s,ns} & & & \end{array} \right] \left[\begin{array}{c} T_s(1) \\ T_s(2) \\ T_s(3) \\ \vdots \\ T_s(i-1) \\ T_s(i) \\ T_s(i+1) \\ \vdots \\ T_s(ns-1) \\ T_s(ns) \end{array} \right] = \left[\begin{array}{c} G_{s,1} \\ G_{s,2} \\ G_{s,3} \\ \vdots \\ G_{s,i-1} \\ G_{s,i} \\ G_{s,i+1} \\ \vdots \\ G_{s,ns-1} \\ G_{s,ns} \end{array} \right]
 \end{aligned}$$

(a) For the granular-bed elements

$$\left[\begin{array}{cccc} A_{c,1} & B_{c,1} & C_{c,1} & D_{c,1} \\ A_{c,2} & B_{c,2} & C_{c,2} & \\ & \vdots & \vdots & \vdots \\ A_{c,nc-1} & B_{c,nc-1} & C_{c,nc-1} & \\ A_{c,nc} & B_{c,nc} & C_{c,nc} & D_{c,nc} \end{array} \right] \left[\begin{array}{c} T_c(1) \\ T_c(2) \\ \vdots \\ T_c(nc-1) \\ T_c(nc) \end{array} \right] = \left[\begin{array}{c} G_{c,1} \\ G_{c,2} \\ \vdots \\ G_{c,nc-1} \\ G_{c,nc} \end{array} \right]$$

(b) For the cold gas elements

Fig. 5 Equation systems for the temperature of infinitesimal elements

Using the above equation, the temperature of the heat pipe element can be obtained from temperatures of infinitesimal elements of the granular bed containing the heat pipe element and those of the cold gas.

(c) Determination of cold gas temperature

Substituting difference equation (17) for Eq. (5), difference equations for each infinitesimal element are obtained as below.

For the element r ,

$$A_{c,r}T_c(r-1) + B_{c,r}T_c(r) + C_{c,r}T_c(r+1) = G_{c,r} \quad (24)$$

The equation of heat balance regarding infinitesimal elements of the cold gas which do not exchange heat with the heat pipes is equivalent to Eq. (5) with the term $a_{cHP}h_{cHP}(T_{HP} - T_c)$ being removed, and comes to have basically the same form as Eq. (24).

Using the above-mentioned difference equations, the temperatures of each part of the moving granular-bed type heat exchanger can be obtained for various operational conditions by repetition of the calculation.

The procedure for the calculation is as follows. First, the hot gas temperature and the amount of heat exchanged between the hot gas and the granular bed are obtained from Eqs. (18) and (19) with the assumed temperatures of the

granular bed. Then the temperature of the granular bed is calculated from the equation system for the temperature of all the infinitesimal elements of the granular bed consisting of Eqs. (20), (21), etc. with the amount of exchanged heat (ref. to Fig. 5(a)). On the other hand, the cold gas temperature is calculated from the equation system for the temperature of all the infinitesimal elements of the cold gas consisting of Eq. (24) etc. (ref. to Fig. 5(b)). Furthermore, making use of the temperatures of the granular bed and the cold gas obtained in this way, the heat pipe temperature is obtainable from Eq. (23). The calculation is to be continued until the temperatures of each part converge. The whole calculation flow for the simulation is shown in Fig. 6.

5. Experimental apparatus

For the research and development of the moving granular-bed type heat exchanger, an experimental apparatus as shown in Fig. 7 was constructed. The hot gas treated with this type of heat exchanger usually contains a large amount of dust, the collection of which by the particles is one of the advantages of this type in addition to the recovery of the sensible heat of the gas. In the present work, however, the dust-free gas was used for an experiment concentrating on investigation of the thermal char-

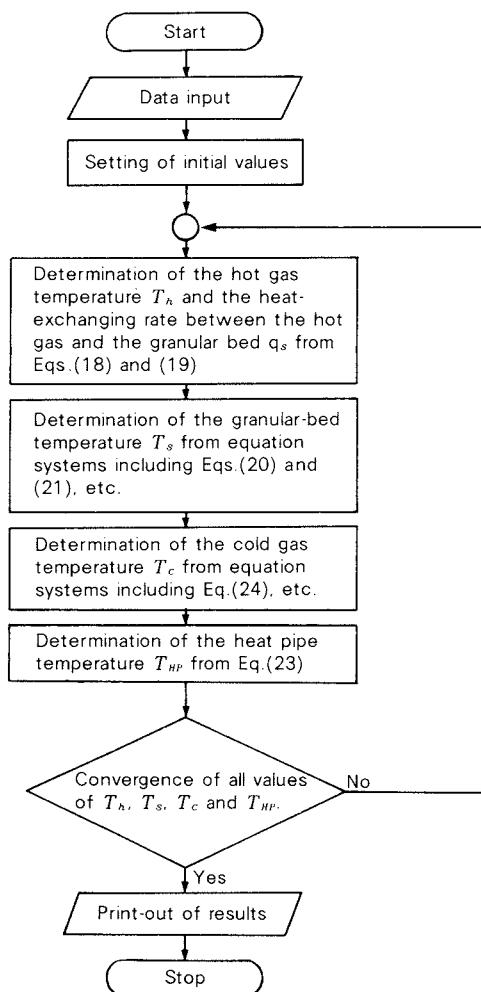


Fig. 6 Flow chart of calculation procedures

acteristics. In this experimental apparatus, silica sands having an average diameter of 1.75 mm and the air were used as the particles and the hot and the cold gas respectively. The heat pipes were made of clad pipes with inner and outer surfaces of copper and steel respectively operated with water as a heat carrier. The heat-recovering section of the experimental apparatus measured 1340mm by 500mm by 200mm deep. The heat-exchanging section contained 6 units of heat pipes, one unit of which consisted of 14 pipes (in the arrangement of 4, 3, 4, 3 in a row) of 25.4 mm in outer diameter and 900 mm in length resulting in a total of 84 pipes. The maximal flow rates of the hot and the cold gas were 300 Nm³/h, and 400 Nm³/h respectively. The moving rate of the granular bed was in the range from 150 to 350 kg/h.

The measurement of temperature was conducted with C-A thermocouples at the following points:

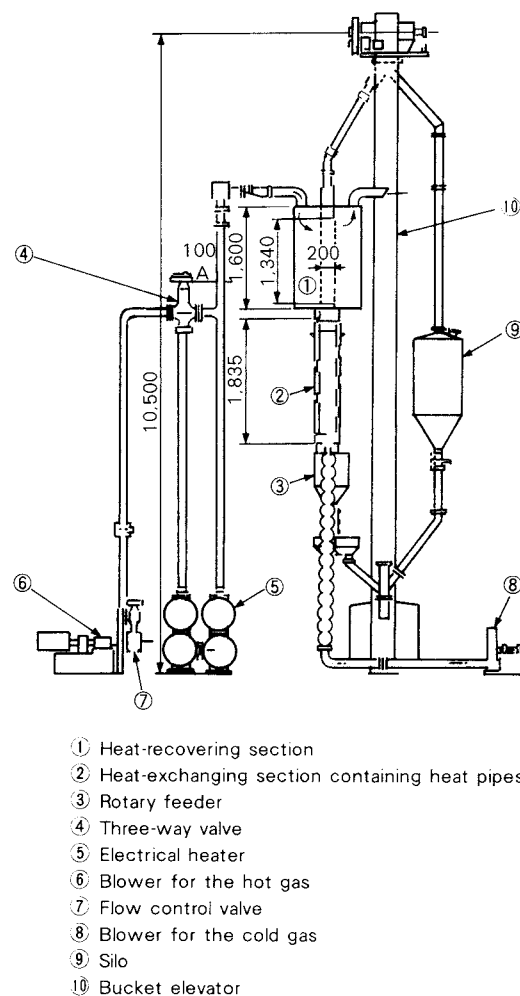


Fig. 7 Overall view of the experimental apparatus of a moving granular-bed type heat exchanger

For the hot gas	
inlet	3 points
outlet	5 points
For the cold gas	
inlet	1 point
in the middle	2 points
outlet	1 point
For silica sands	
in the heat-recovering section	10 points
in the heat-exchanging section	
containing heat pipes	14 points
For steam inside the heat pipes	21 points

The mass flow rate of the hot gas was kept constant automatically with a data processor independent of frequent variation of the temperature through the measurement of the static pressure and the temperature at the measuring points as well as the pressure difference of the orifice flow meter. Additionally, the hot gas temperature at the inlet was made adjustable

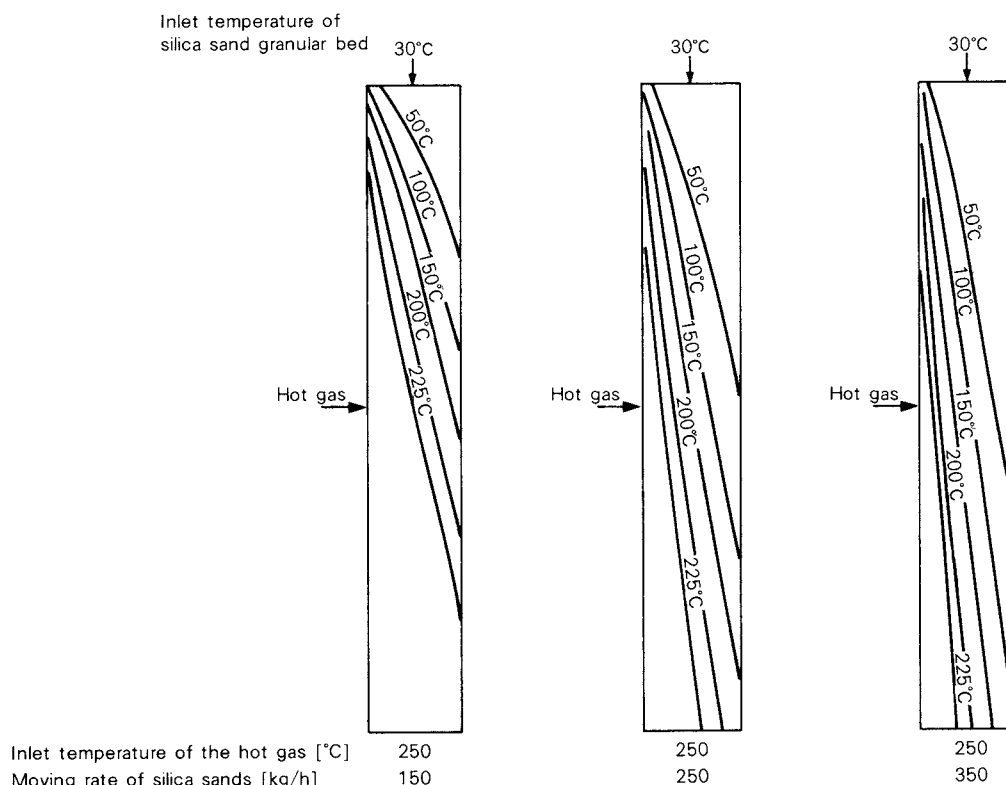


Fig. 8 Temperature distribution of silica sand granular bed within the heat-recovering section

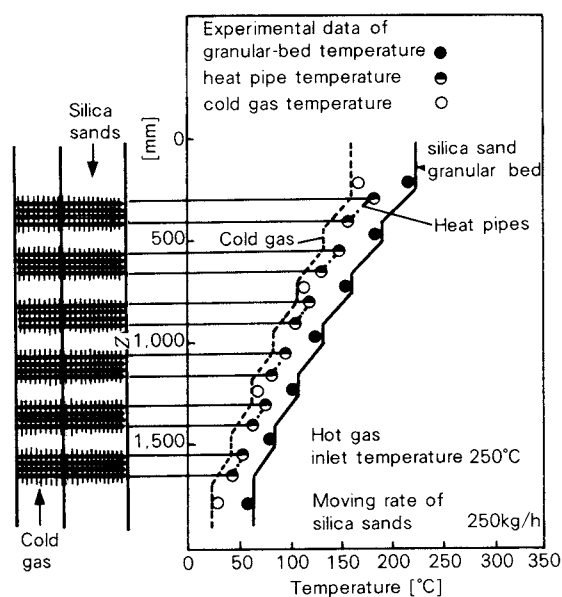


Fig. 9 Temperature distribution of the heat-exchanging section containing heat pipes

arbitrarily in the range from ambient temperature to 400°C by means of the control of the current to an electrical heater combined with a three-way valve. The flow rate of the cold gas was adjusted manually corresponding to the indication of an orifice flow meter.

6. Comparison of the calculation results with the experimental ones

The simulation was conducted according to the conditions of the experimental apparatus. It could give the temperature distribution of each part of the apparatus in a steady state under arbitrary operational conditions. For example, Fig. 8 shows the temperature distribution of silica sands in the heat-recovering section with a variation of their moving rate, keeping the inlet temperature and the flow rate of the hot gas constant. This figure gives information about the characteristics of the temperature rise of the silica sands in relation to their moving rate.

Figure 9 shows an example of the calculated temperature distribution of the silica sand bed, the heat pipes and the cold gas in the heat-exchanging section containing the heat pipes together with plots of experimental results. The results obtained from calculation coincided well with the experimental ones quantitatively as well as qualitatively, which confirms the high accuracy of the calculation.

As an example to demonstrate the perform-

Table 1 Comparison of the calculation results with the experimental ones

	Item	CASE 1		CASE 2		CASE 3	
Conditions	Hot gas inlet temperature ($^{\circ}\text{C}$)	250		350		250	
	Hot gas flow rate (Nm^3/h)	200		200		200	
	Silica sand inlet temperature ($^{\circ}\text{C}$)	30		30		30	
	Silica sand moving rate (kg/h)	250		250		350	
	Cold gas inlet temperature ($^{\circ}\text{C}$)	20		20		20	
	Cold gas flow rate (Nm^3/h)	200		200		200	
		Calculated	Experimental	Calculated	Experimental	Calculated	Experimental
Results	Hot gas outlet temperature ($^{\circ}\text{C}$)	76.8	80.7	99.1	95.2	48.3	57.2
	Granular-bed temperature at the outlet of heat-recovering section ($^{\circ}\text{C}$)	227.7	228.4	319.2	319.6	195.2	187.1
	Granular-bed outlet temperature ($^{\circ}\text{C}$)	56.9	55.3	78.4	69.7	79.1	73.1
	Top heat pipe temperature ($^{\circ}\text{C}$)	176.6	182.3	249.8	255.0	169.3	173.1
	Bottom heat pipe temperature ($^{\circ}\text{C}$)	35.0	39.2	43.7	46.4	45.2	47.5
	Cold gas outlet temperature ($^{\circ}\text{C}$)	158.9	166.5	226.7	232.2	158.9	164.4

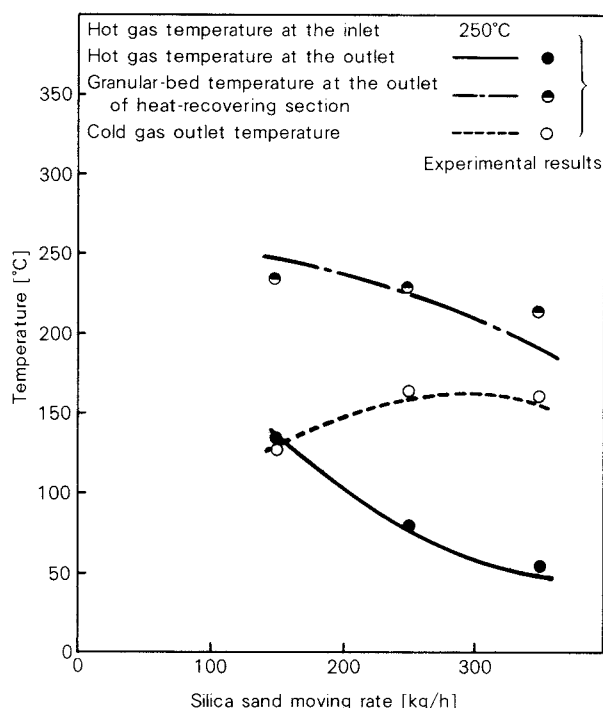


Fig.10 Variation of temperatures at some parts of the heat exchanger with the moving rate of silica sands

ance of the moving granular-bed type heat exchanger, theoretically obtained variations of the hot gas outlet temperature, the mean outlet temperature of the silica sand* bed from the heat-recovering section and the outlet temperature of the cold gas with the moving rate of the silica sand bed are shown together with some experimental results in Fig. 10, with the other conditions constant. From this figure, it is seen that the results obtained from both calculation and experiments coincide well quantitatively as well as qualitatively. It is also possible to detect the optimal moving rate of the silica sands

which gives the highest outlet temperature of the cold gas. For a quantitative comparison of the calculation results with the experimental ones, the values of each of the properties are shown in Table 1 in three cases of different operational conditions for the experimental apparatus. From the table it is affirmed that the theoretical and experimental results coincide well, allowing a difference of 8°C at most in each case. Furthermore, both results showed a consistency of similar degree under other operational conditions.

7. Conclusion

A simulation for the investigation of the thermal characteristics of the moving granular-bed type of heat exchanger in the steady state was conducted solving difference equations using the numerical analysis method. In the simulation model, the calculation was performed two-dimensionally in the heat-recovering section in contact with the hot gas and some adjacent parts of the granular bed where the temperature varied in the z - and x - directions, while the other parts were handled in one dimension.

The heat transfer coefficients between the hot gas and the granular bed and between the granular bed and the heat pipes were obtained from the general theoretical equations for packed beds with experimental data and from our experiments respectively. Furthermore, for the heat transfer coefficient between the heat pipes and the cold gas, we used an experimental equation which has been used to evaluate the heat transfer coefficient between pipes with fins and the fluid which flows vertically to

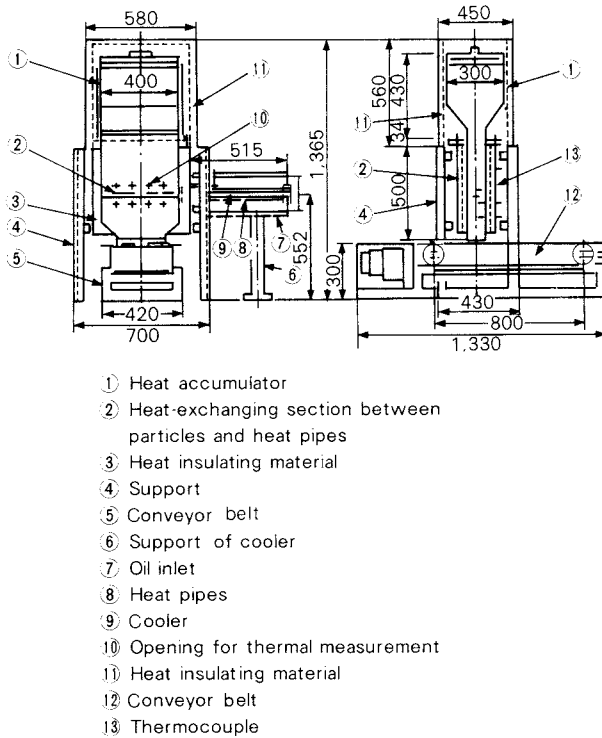


Fig. 11 Overall view of experiment apparatus of moving granular-bed type heat exchanging elements

rows of pipes.

The results from the simulation showed good agreement with those from the experiments, which confirmed that the thermal characteristics of the moving granular-bed type heat exchanger can be obtained with high accuracy by means of the method of the present research.

Appendix

Measurement of heat transfer coefficient between the granular bed and the heat pipes

An experimental apparatus of heat-exchanging elements of a moving granular bed shown in Fig. 11 was constructed for the purpose of measurement of the heat transfer coefficient between the granular bed and the heat pipes. This apparatus consisted of a heat-accumulating section at the top, the heat-exchanging section of heat pipes in the middle and the discharging device of particles of the moving bed at the bottom. The particles having a uniform temperature after being heated in an electrical oven for a long time were fed in the heat accumulator and were discharged from the bottom with a belt conveyor at a constant rate, so that they moved through the heat-exchanging sec-

tion at a constant speed. The heat transfer coefficient between the granular bed and the heat pipes was obtained by measuring the temperature difference and the heat transferred between the granular bed and the outer surface of the heat pipes. Silica sands having a mean diameter of 1.75 mm were used as the particles. The experiments were conducted at three thermal settings of 350°C, 300°C and 260°C in the speed range of the moving granular bed in the heat-exchanging section from 0.5 to 5.0 cm/min. The results shown in Fig. 3 were made use of for the simulation.

Nomenclature

A_r	: surface area per unit length of a heat pipe without fins	[m ² /m]
A_f	: surface area of fins per unit length of a heat pipe	[m ² /m]
a_{cHP}	: effective heat transferring area of heat pipes with fins per unit volume on the side of cold gas	[m ² /m ³]
a_{cw}	: contact area of wall with cold gas per its unit volume	[m ² /m ³]
a_{hw}	: contact area of wall with hot gas per its unit volume	[m ² /m ³]
a_s	: contact area of particles with hot gas per unit volume of granular bed	[m ² /m ³]
a_{sHP}	: effective heat transferring area of heat pipes with fins per unit volume on the side of granular bed	[m ² /m ³]
a_{sw}	: contact area of granular bed with wall per unit volume	[m ² /m ³]
c_c	: specific heat of cold gas	[J/kg°C]
c_h	: specific heat of hot gas	[J/kg°C]
c_s	: specific heat of particles	[J/kg°C]
D_h	: mixing diffusivity of hot gas	[m ² /s]
D_r	: inner diameter of fins	[m]
d_p	: particle diameter	[m]
G_{max}	: maximum mass velocity of fluid between heat pipes	[kg/m ² s]
h_{cHP}	: heat transfer coefficient between cold gas and heat pipes with fins	[W/m ² °C]
h_{hs}	: heat transfer coefficient between hot gas and granular bed	[W/m ² °C]
h_{rv}	: radiant heat transfer coefficient in granular bed	[W/m ² °C]
h_{sHP}	: heat transfer coefficient between granular bed and heat pipes	[W/m ² °C]
h^*	: conductive heat transfer coefficient between particles	[W/m ² °C]
k_{sI}	: effective thermal conductivity of granular bed with stationary gas	[W/m°C]
k_{sII}	: effective thermal conductivity of	

	granular bed with gas flow	[W/m ² °C]		
k_c	: thermal conductivity of cold gas	[W/m ² °C]	Δx	: length of infinitesimal element of granular bed in x-direction [m]
k_{hx}	: thermal conductivity of hot gas in x-direction	[W/m ² °C]	Δy	: length of infinitesimal element of granular bed in y-direction [m]
k_{hz}	: thermal conductivity of hot gas in z-direction	[W/m ² °C]	Δz	: length of infinitesimal element of granular bed in z-direction [m]
n_f	: number of fins per unit length of a heat pipe	[-]	α	: a constant, equal to 0.179 at the closest packing [-]
q_s	: heat transferred from hot gas per unit volume of granular bed per unit time	[W/m ³]	β	: ratio of mean distance between centers of two adjacent particles to particle diameter [-]
S_1, S_2	: pitch in arrangement of heat pipes	[m]	γ	: ratio of mean thickness of granular bed to particle diameter [-]
T_a	: atmospheric temperature	[°C]	ϵ	: void fraction [-]
T_c	: cold gas temperature	[°C]	ϵ_s	: $1 - \epsilon$ [-]
T_{ci}	: cold gas temperature at the inlet	[°C]	μ_h	: hot gas viscosity [Ns/m ²]
T_{HP}	: heat pipe temperature	[°C]	ρ_c	: cold gas density [kg/m ³]
T_h	: hot gas temperature	[°C]	ρ_h	: hot gas density [kg/m ³]
T_{hi}	: hot gas temperature at the inlet	[°C]	ρ_s	: particle density [kg/m ³]
T_s	: granular-bed temperature	[°C]	ϕ	: ratio of effective thickness of fluid film in granular bed to particle size [-]
T_{si}	: granular-bed temperature at the inlet	[°C]	τ	: time [s]
U_{cw}	: overall heat transfer coefficient between the atmosphere and cold gas in the duct	[W/m ² °C]		
U_{hw}	: overall heat transfer coefficient between the atmosphere and hot gas in the duct	[W/m ² °C]		
U_{sw}	: overall heat transfer coefficient between granular bed and the atmosphere	[W/m ² °C]		
u_c	: cold gas velocity	[m/s]		
u_o	: superficial velocity of hot gas in granular bed	[m/s]		
u_s	: moving velocity of granular bed	[m/s]		
V_s	: volume of infinitesimal element of granular bed	[m ³]		
V_c	: volume of infinitesimal element of cold gas	[m ³]		

References

- 1) The Japan Society of Mechanical Engineers: "Materials for Heat Transfer Engineering (The third edition)", 172 (1975).
- 2) Kunii, D.: "Thermal Unit Operation (I)", Maruzen Co., Ltd., 132-133 and 136-150 (1976).
- 3) Vampola, J.: *Chem. Techn.*, **27**, 26 (1965).
- 4) Amundson, N.R.: *Ind. and Eng. Chem.*, **48**, 26-50 (1965).
- 5) Togawa, H.: "Numerical Calculation of Differential Equations", Ohmsha Ltd. (1973).

Toshio Oshima and Mitsuaki Hirota

Department of Chemical Engineering
Himeji Institute of Technology*

1. Introduction

It is well known that a powder bed is sheared in one of the following three ways¹⁾:

- 1) Powder bed reaches the steady flow state after yielding with expansion.
- 2) Powder bed reaches the steady flow state at the start of yielding without volume change.
- 3) Powder bed reaches the steady flow state after yielding with contraction.

To experimentally examine the above yielding phenomena, the accurate measurement of expansion and contraction of the powder bed is essential. Although cell-type direct shear testers are widely used for the shear test, it is difficult to uniformly load the shear stress on these testers and the accurate measurement of volume change in the powder bed is impossible because of the effect of the cell wall especially for fine powders with high void fraction. Therefore, the results measured by a single tester for the whole yield locus over the range of expansion and contraction on yielding of the powder bed have been scarcely obtained.

In this experiment, a direct shear tester with parallel plates is used. This tester has been made by modifying the testers originally designed by Hiestand^{2,3)} or Budny⁴⁾. It is suitable for the accurate measurement of expansion and contraction in the shear process because the powder bed is not restricted by the cell wall. The data obtained by the tester are discussed on Roscoe condition diagram. Moreover, the bed consolidated by pre-shearing on the basis of Jenike's method⁵⁾ and the bed consolidated uniaxially without pre-shearing are tested to examine the effect of the pre-shearing on the powder yield locus.

2. Experimental apparatus and procedures^{6,7)}

The outline of the direct shear tester with parallel plates is shown in Fig. 1. In the present shear test, calcium carbonate (mass median diameter $D_p = 3.5 \mu\text{m}$) and silica powder ($D_p = 5.5 \mu\text{m}$) were used as test materials after drying at 120°C for 48 hours and removing the agglomerate with a 32 mesh sieve. These materials were consolidated in two ways: the uniaxial consolidation for the examination of the shear process with expansion or contraction of powder beds and the shear consolidation for comparison with the shear test due to Jenike's method.

For the uniaxial consolidation test, a sample powder bed of 1 mm thickness was packed on a fixed plate ①, and then gently twisted by a movable plate ② mounted on the bed. After pre-consolidation under the normal stress σ_p for five minutes, the bed was sheared under the normal stress σ by weight placed on the movable plate. The shear test was conducted under the tensile force by motor ⑩ under the condition that the normal stress was less than the stress due to the movable plate or was negative (including the tensile strength). It became possible by using this tester to conduct not only the shear test under slight stress but also the tensile strength test which produced the same failure plane as the shear plane.

For the shear consolidation, on the other hand, the same procedure as Jenike's method was adopted. The powder bed under the normal stress σ_v on the movable plate was sheared until the steady state where the stress and the volume were constant was achieved. Then this powder bed was sheared under the normal stress σ less than σ_v . Furthermore, Jenike's tester was also used for comparison with these results.

In both tests, the displacement in the direction of the normal stress was measured within an error of about $0.5 \mu\text{m}$ by a noncontacting

* 2167 Shosya, Himeji, Hyogo, 671-22
TEL. 0792 (66) 1661

Received May 7, 1985

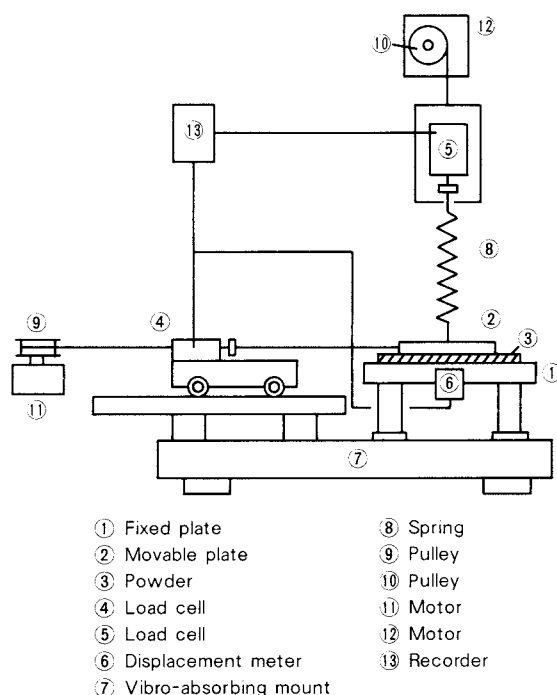


Fig. 1 Schematic diagram of apparatus

displacement meter ⑥ plugged into the fixed plate.

3. Shear process and yield locus⁸⁾

Figure 2 shows Roscoe condition diagram which represents yielding characteristics of the powder bed. Consider the shear process of the powder bed with a void fraction $\epsilon = \epsilon_b$. At the normal stress $\sigma = \sigma_b$, the shear stress τ increases from the point C to the point E until the powder bed becomes the steady flow state at the point E. When $\sigma = \sigma_a$ ($\sigma_a < \sigma_b$), τ increases from the point H to the point P at which point the yielding starts with expansion, and then τ decreases gradually along PpZ with increasing the void fraction from ϵ_b to ϵ_a until the powder bed becomes the steady flow state at the point Z. When $\sigma = \sigma_c$ ($\sigma_c > \sigma_b$), τ increases from the point F to the point Q at which point

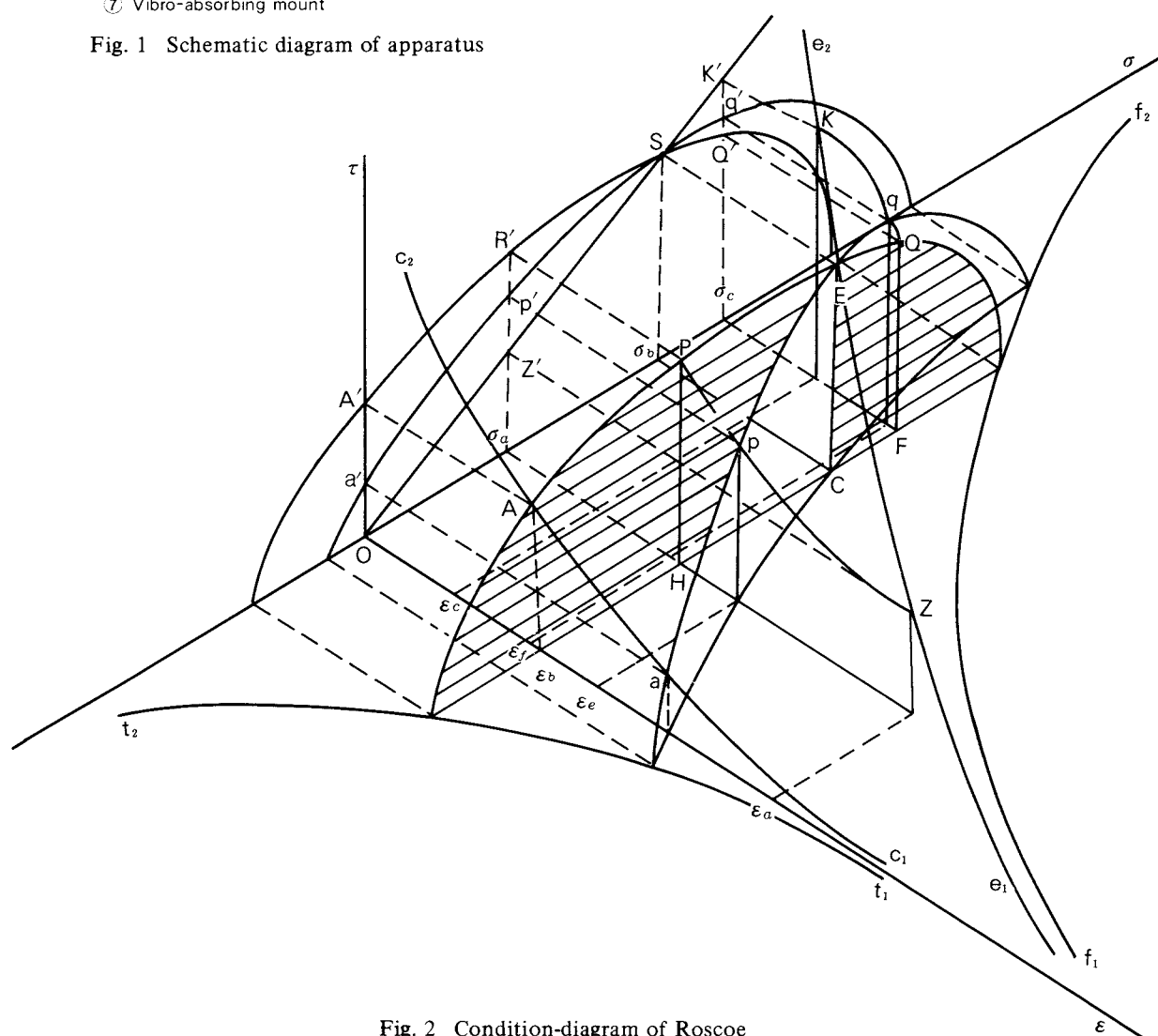


Fig. 2 Condition-diagram of Roscoe

the yielding starts with contraction, and then τ increases gradually along QqK with decreasing the void fraction from ϵ_b to ϵ_c until the powder bed becomes the steady flow state at the point K. As a result, the yield locus (Y.L.) which gives the correlation of τ and σ at the yield point of the powder bed is displayed by a line A'R'SQ' which is projected as a line APEQ on $\sigma - \tau$ plane. This line represents the yield locus for the powder bed with the void fraction ϵ_b characterized by pre-consolidation stress because τ and σ are obtained at the start point of yielding.

The yield locus obtained from τ and σ at the steady flow state becomes a line OZ'SK' which is projected as a line e_1 ZEKE₂ on $\sigma - \tau$ plane. This yield locus is the critical state line (C.S.L.) proposed by Schwedes¹⁾. The void fraction ϵ decreases as σ increases; that is, the specified values of τ and σ exist for a certain value of ϵ . If the yield locus is obtained from τ and σ at some shear displacement instead of at the start point of yielding, this locus becomes a line a'p'Sq' which is projected as a line apEq on $\sigma - \tau$ plane. In this line, the void fractions at the points p, E, q are expressed as ϵ_e , ϵ_b , ϵ_f , respectively. It is also shown in Fig. 2 that the yield locus approaches a C.S.L. with increasing the yield criterion which is defined by the volume change in the powder bed, since the void fraction increases with progress of shearing. Therefore, the shear stress at the start point of the yielding should be accurately measured to obtain the yield locus of the powder bed prepared under a given consolidation stress.

4. Results and discussion

4. 1 Measurement of yield locus by the shear tester with parallel plates^{7,8)}

Figure 3 shows the relation between the displacement of the powder bed in the direction of the normal stress, Δn (the sign is positive when expansion takes place), and the shear stress, τ , in the shear process of calcium carbonate pre-consolidated at 4.9 kPa. For the low normal stress in shearing ($\sigma_0 \sim \sigma_2$), the powder bed expanded and the shear stress decreased clearly with progress of yielding. In this case, the shear stress at the start of yielding could easily be obtained with high reproducibility. For the high normal stress in shear-

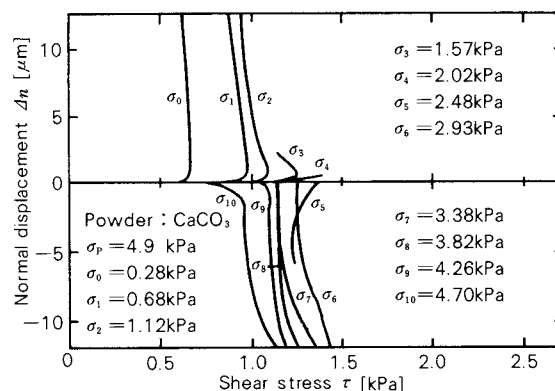


Fig. 3 Shear process diagram

ing ($\sigma_4 \sim \sigma_{10}$), the shear stress at the start of yielding was difficult to determine because the powder bed contracted gradually with increasing the shear stress. Therefore, the criterion of yielding of the powder bed based on the displacement in the direction of the normal stress Δn was adopted in this work because the definition of the yield of the powder bed should be clarified to obtain the accurate yield locus.

Figure 4 shows the effect of the yield criterion Δn on the powder yield locus. It is found from this figure that the yield locus approached to the critical state line with increasing the yield criterion Δn from 2 μm to 20 μm and this tendency would agree with the description in the previous section. The suitable value of the yield criterion Δn obtained in this experiment might be considered 2 μm that was about a half of the diameter of the sample powder because the consolidation yield locus showed reasonable shape. This implies that the value of Δn would be dependent on a particle size of the sample powder. Hence, the accurate measurement of the value of Δn up to the same

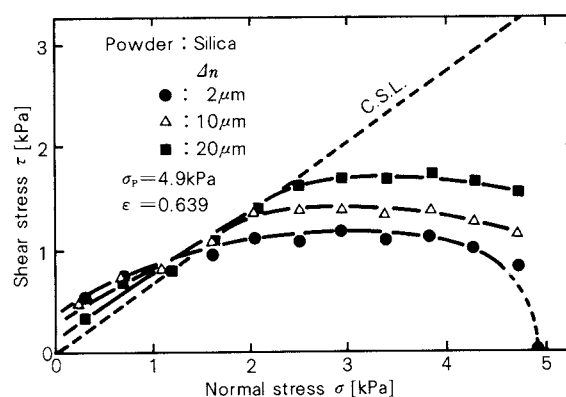


Fig. 4 Effect of yield criterion on Y.L.

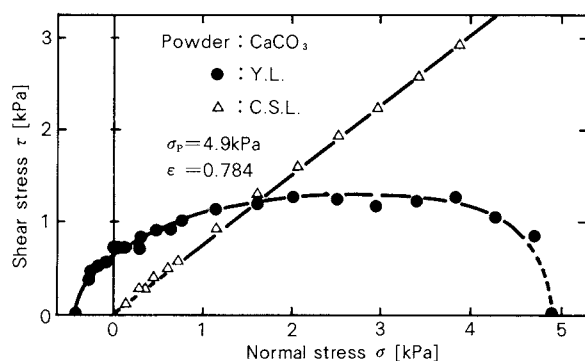


Fig. 5 Y.L. and C.S.L. of CaCO_3

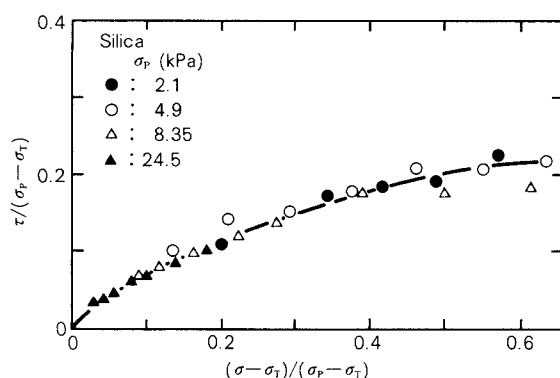


Fig. 6 Family of yield loci of silica rearranged using the reduced stress

size as that of a particle is required to obtain a satisfactory yield locus.

Figure 5 shows the yield locus and the critical state line of calcium carbonate which was pre-consolidated at $\sigma_p = 4.9$ kPa. As a consequence of using the yielding criterion based on the displacement in the direction of the normal stress Δn , the consolidation yield locus could be obtained experimentally. Therefore, the whole range of the powder yield locus including the tensile strength and the cohesion could be expressed as a single smooth curve, although there had been almost no powder yield locus given by a single tester over the whole range.

Recently, Williams et al.⁹⁾ reported the reduced yield locus based on the yield locus obtained from the shear test and the tensile strength test. In their method, the normal stress corresponding to the end point of the yield locus in the range accompanied by expansion of the powder bed must be determined; however, the decision of this point is very troublesome. In this paper, the pre-consolidation stress σ_p is used instead of the normal stress at the end point; the reduced yield locus

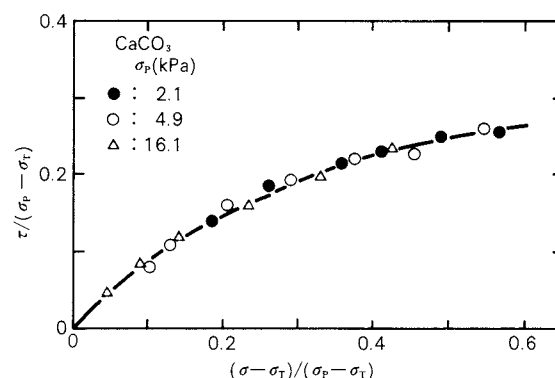


Fig. 7 Family of yield loci of CaCO_3 rearranged using the reduced stress

is obtained by assuming that the similarity can be held independently of σ_p for any yield locus. Figures 6 and 7 show that the relation between the reduced yield loci given by the dimensionless stress $\tau/(\sigma_p - \sigma_T)$ instead of τ and $(\sigma - \sigma_T)/(\sigma_p - \sigma_T)$ instead of σ . Although silica powder shown in Fig. 6 or calcium carbonate shown in Fig. 7 had its individual shear characteristics, each reduced yield loci of these two materials could be expressed as a nearly single curve, independently of σ_p . Therefore, if the reduced yield locus of the powder bed pre-consolidated at an arbitrary normal stress σ_p is known, a yield locus pre-consolidated at a normal stress other than σ_p can be estimated by only a measured value of the tensile strength σ_T .

4. 2 Effect of the consolidation method of the powder bed⁶⁾

In order to find how the yield locus was affected by the consolidation method of the powder bed, the shear test was performed concerning the two kinds of powder beds prepared by different methods: the powder bed pre-sheared on the basis of Jenike's method (shear-consolidated bed) and the powder bed consolidated uniaxially (uniaxially consolidated bed). The effect of the consolidation methods on the yield locus was examined for the both powder beds.

Experimental results of the shear-consolidated bed obtained by Jenike's tester were compared with those by the parallel plate-type tester. Figure 8 shows the critical state line and the yield loci after pre-sheared at the normal stress of 4.9 kPa for silica powder. The yield

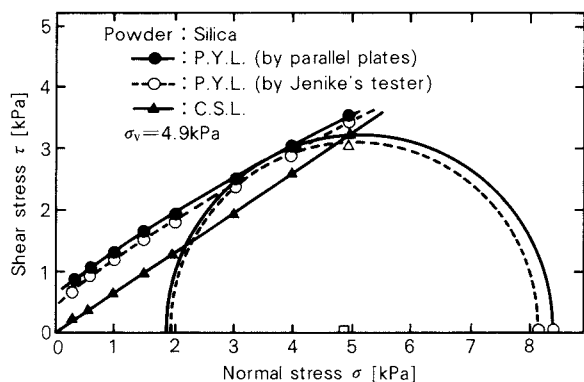


Fig. 8 Effect of shear tester on yield locus of silica

loci obtained by both the testers agreed well and C.S.L. agreed perfectly. This is probably because the shear plane would reach the steady flow as stated previously and a certain particle arrangement resulted from the normal stress would be formed during pre-shearing.

Figure 9 shows the experimental results of the uniaxially consolidated bed compared with those of the shear-consolidated bed ($\sigma_v = 4.9$ kPa). The yield locus of the bed uniaxially consolidated at the normal stress $\sigma_p = 4.9$ kPa was lower than that of the bed shear-consolidated at the shear-consolidation stress $\sigma_v = 4.9$ kPa. The uniaxially consolidated bed was consolidated only with the normal stress σ_p , while the shear-consolidated bed was consolidated with both the normal stress and the shear stress. Since the maximum principal stress obtained was 8.35 kPa as indicated in Fig. 8, the yield locus of the uniaxially consolidated bed pre-consolidated at $\sigma_p = 8.35$ kPa was compared with that of the shear-consolidated bed pre-sheared at $\sigma_v = 4.9$ kPa; the former was found to be still lower than the latter. So, further pre-consolidation stress for the uniaxially consolidated bed was applied by the method of trial and error and it was found that a yield locus of the uniaxially consolidated bed pre-consolidated at $\sigma_p' = 24.5$ kPa was nearly equal to that

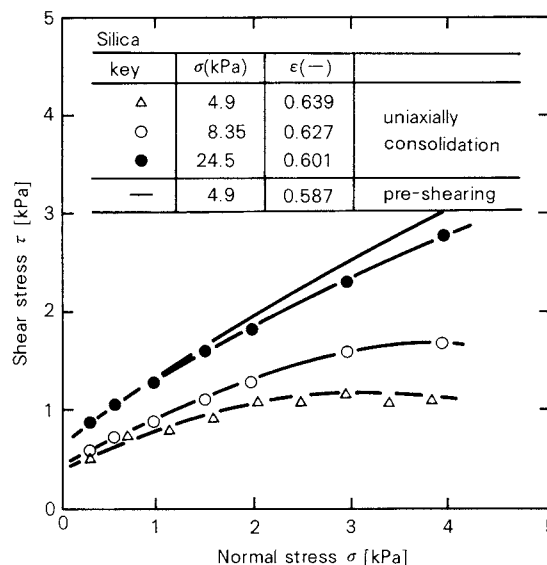


Fig. 9 Effect of consolidation method on Y.L. of silica

of the shear-consolidated bed pre-sheared at $\sigma_v = 4.9$ kPa. That stress σ_p' was five times as large as the pre-sheared stress σ_v and was three times as large as the maximum principal stress of the shear-consolidated bed. Thus, it became clear that the normal stress required for pre-consolidation of the uniaxially consolidated bed would be much larger than the pre-shear stress to obtain the same yield locus for the uniaxially consolidated bed and the shear-consolidated bed.

Average void fractions of the consolidated bed by Jenike's tester and of the uniaxially consolidated bed by a parallel plate-type shear tester are shown in Table 1. The void fractions of the shear-consolidated bed were much smaller than that of the uniaxially consolidated bed at the same consolidation stress, and they were close to that of the uniaxially consolidated bed pre-consolidated at σ_p' .

5. Conclusion

From the results of shear test using a parallel

Table 1 Effect of consolidation method on void fraction

	pre-shearing (by Jenike's tester)		uniaxially consolidation (by parallel plates)			
	σ_v [kPa]	ϵ [-]	σ_p [kPa]	ϵ [-]	σ_p' [kPa]	ϵ [-]
silica	4.9	0.587	4.9	0.639	24.5	0.601
CaCO ₃	4.9	0.725	4.9	0.784	32.5	0.735

plate-type shear tester, the relation between the shear characteristics and the yield locus was examined. By using a Jenike's shear tester as well as this tester, the effect of the consolidation method on the yield locus was also examined. The following results could be obtained by examining the experimental data.

- 1) The yield locus in the low normal stress range where the powder bed expanded with yielding could be determined reproducibly by a parallel plate-type shear tester. On the other hand, the yield locus in the high normal stress range where the powder bed contracted with yielding varied with the yield criterion. Therefore, it was considered to be essential to establish the clear yield criterion for determining an accurate yield locus. The yield criterion was defined by the displacement in the direction of the normal stress, and the suitable value of the displacement obtained in this experiment was about a half of the median diameter of the sample powders.
- 2) With increasing the yield criterion, the yield locus approached the critical state line. The determination of the shear stress at the start point of yielding was found to be important in order to obtain exactly the yield locus of the powder bed prepared at the fixed void fraction.
- 3) The reduced yield locus in terms of the two dimensionless stresses, that is, $\tau/(\sigma_p - \sigma_T)$ instead of τ and $(\sigma - \sigma_T)/(\sigma_p - \sigma_T)$ instead of σ , could be expressed as a single line for the powder beds under various pre-consolidation stresses. If the reduced yield locus of the powder bed pre-consolidated at an arbitrary normal stress σ_p is known, a yield locus of the powder bed pre-consolidated at a normal stress other than σ_p may be easily

estimated by only a measured value of the tensile strength σ_T .

- 4) The yield locus of the powder bed pre-sheared on the basis of Jenike's method was higher than that of the powder bed pre-consolidated uniaxially at the same normal stress. This implies that the uniaxially consolidated powder bed would require larger pre-consolidation stress than the maximum principal stress of the pre-sheared powder bed to obtain the same extent of yield locus.

Nomenclature

Δn	: displacement in the direction of the normal stress	[μm]
ϵ	: void fraction of powder bed	[—]
σ	: normal stress in shear process	[kPa]
σ_p	: pre-consolidation stress of uniaxially consolidated bed	[kPa]
σ_v	: normal stress at the steady shear state of shear-consolidated bed	[kPa]
σ_T	: tensile strength of powder bed	[kPa]
τ	: shear stress in shear process	[kPa]

References

- 1) Schwedes, H.: *Powder Technol.*, **11**, 59 (1975).
- 2) Hiestand, E.N. and C.J. Wilcox: *J. Pharm. Sci.*, **57**, 1421 (1968).
- 3) Hiestand, E.N. and C.J. Wilcox: *J. Pharm. Sci.*, **58**, 1403 (1969).
- 4) Budny, T.J.: *Powder Technol.*, **23**, 197 (1979).
- 5) Jenike, A.W., P.J. Elsey and R.H. Woolley: *Proceedings, Am. Soc. Test. Mat.*, 1168 (1960).
- 6) Hirota, M., T. Kobayashi, H. Tajiri, H. Murata, M. Wakabayashi and T. Oshima: *J. Soc. Powder Technol. Japan*, **22**, 144 (1985).
- 7) Hirota, M., T. Kobayashi and T. Oshima: *J. Soc. Powder Technol. Japan*, **22**, 271 (1985).
- 8) Hirota, M. T. Kobayashi, O. Sano and T. Oshima: *J. Soc. Powder Technol. Japan*, **21**, 137 (1984).
- 9) Williams, J.C. and A.H. Birks: *Powder Technol.*, **1**, 199 (1967).

Yasuo Kousaka

Department of Chemical Engineering
University of Osaka Prefecture*

1. Introduction

Submicron particles or ultrafine particles have been paid increasing attention in various fields, and attention seems to be shifted to smaller and smaller particles with the times. In fact, detection, characterization and control of particles of $0.1\ \mu\text{m}$ or smaller in size have become important in clean rooms for semiconductor production processes, in fine ceramics industries, in combustion processes, and in atmospheric or indoor environmental problems, and so on.

Some topics on submicron particles suspending in a gaseous or liquid medium will be briefly introduced in this paper. In the former section of this paper, typical size-dependent properties of a particle are looked through, and topics on coagulation and deposition which may play an important role in a particle dispersed system in industrial processes are introduced in the following sections.

2. Size-dependent properties of submicron particles

Typical size-dependent properties of particles suspending in air and in water are shown in Fig. 1 together with the corresponding equations. The solid lines in the figure are those in air, while the dashed lines in water and the one-point dashed line are in low-pressure air. The curves appearing in the figure are briefly explained in the following.

Terminal settling velocity in the gravity field, u_t , decreases both in air and in water with the decrease in particle size, as is expressed by Eq. (1). The distortion in the small size range of the solid line of u_t is caused by the

slip coefficient C_c which is size-dependent as shown in Eq. (2). The slip coefficient C_c increases with the decrease in size of particles suspending in a gaseous medium, but it is always unity for particles suspending in a liquid medium. It increases with the decrease of gas pressure p as shown in Eq. (3), an example of which is shown in Fig. 1 (C_c').

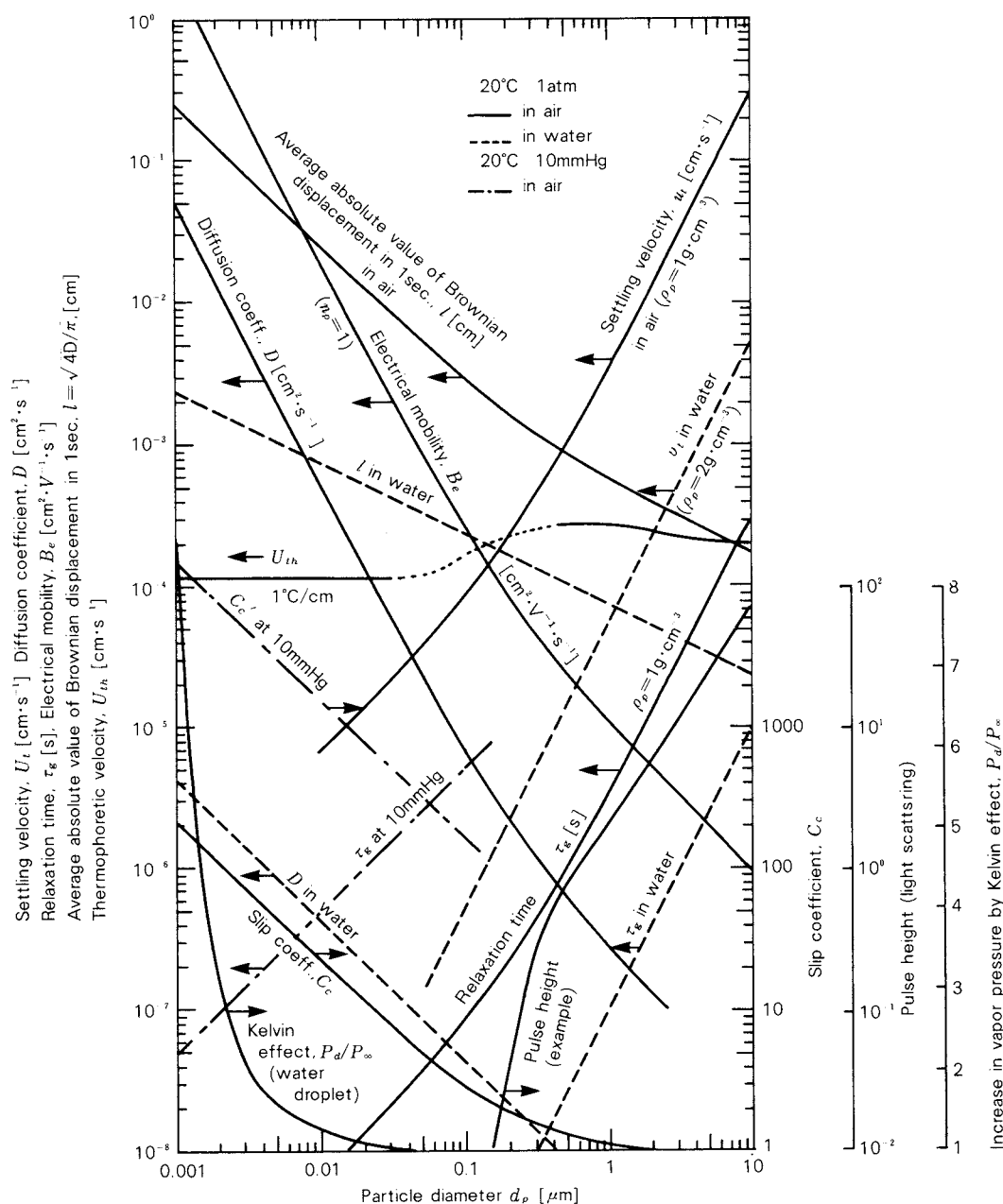
When a particle is small, Brownian motion which is caused by random variations in the incessant bombardment of molecules against the particle occurs. The average absolute value of Brownian displacement in one second, l , is shown in Fig. 1, which is obtained as $t = 1\ \text{sec}$ in Eq. (4). The intersections of the curves of l and u_t lie in around $0.5\ \mu\text{m}$ in air and $1\ \mu\text{m}$ in water. If one may observe the settling velocity of such a small particle in a short time, it will be a resultant velocity caused by both gravitational settling and Brownian motion. D in Eq. (4) is the particle diffusion coefficient which is given by Eq. (5). The larger values of D indicate that more vigorous Brownian motion and more rapid particle transfer in a particle concentration gradient occur. As is seen in Fig. 1, the particle diffusion coefficient in water is much smaller than that in air.

τ_g in Fig. 1 is called relaxation time and is given by Eq. (6). It has a unit of time and it characterizes the time required for a particle to relax its velocity to a new condition of forces. When a particle is projected into a stationary fluid with a velocity u_o , it will travel a finite distance before it stops. Such a distance is called stop-distance and is given by $u_o\tau_g$. So τ_g can be a measure of inertial motion of a particle in a fluid.

B_e in Fig. 1 is the electrical mobility which expresses the velocity of a charged particle in an electric field of unit strength. The steady particle velocity in an electric field E is given by EB_e . Since B_e depends upon the number of elementary charge which a particle carries,

* 4-804 Mozu-Umemachi, Sakai, Osaka, 591
TEL. 0722 (52) 1161

Received May 7, 1985



$$u_t = \frac{(\rho_p - \rho_f) g d_p^2 C_c}{18\mu} \quad (1) \quad C_c = 1 + 2.514 \frac{\lambda}{d_p} + 0.80 \frac{\lambda}{d_p} \exp\left(-0.55 \frac{d_p}{\lambda}\right) \quad (2)$$

$$C_c' = 1 + (2/pd_p)[6.32 + 2.01 \exp(-0.1095pd_p)] \quad p \text{ in cmHg, } d_p \text{ in } \mu\text{m} \quad (3)$$

$$l = \sqrt{\frac{4Dt}{\pi}} \quad (4) \quad D = \frac{\kappa T C_c}{3\pi\mu d_p} \quad (5)$$

$$\tau_g = \frac{\rho_p d_p^2 C_c}{18\mu} \quad (6) \quad B_e = \frac{n_p e C_c}{3\pi\mu d_p} \quad (7)$$

$$P_d/P_\infty = \exp\left(\frac{4M\sigma}{RT\rho_1 d_p}\right) \quad (8)$$

e = elementary charge, M = molecular weight,
 n_p = number of elementary charges that the
particle carries, p_d and p_∞ = vapor pressure
on droplet and on flat surface, R = gas
constant, T = temperature, κ = Boltzmann
constant, λ = mean free path, μ = viscosity
 ρ_f, ρ_1 and ρ_p = density of fluid, droplet and
particle, σ = surface tension, t = sec

Fig. 1 Size-dependent properties of a particle suspending in air and in water.

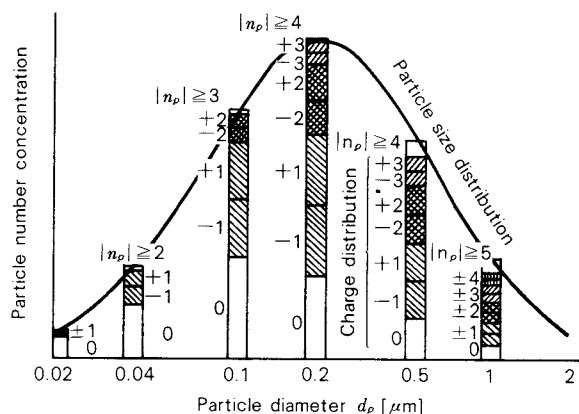


Fig. 2 Number of elementary charge, n_p , at an equilibrium state of diffusion charging of bipolar ions.

n_p , as seen in Eq. (7), n_p should be made clear to determine B_e . n_p is predictable with aerosol particles in most cases, where particles are charged by diffusion of ions¹⁾. An example where particles are charged in a large number of bipolar ions by diffusion is shown in Fig. 2. In a liquid, on the other hand, it is difficult to predict n_p in general because of the complex interaction between a particle and surrounding ions. Figure 3 shows the particle trajectories in air in a vertical parallel plate electrodes. The zigzag movement in the figure is caused by Brownian motion and the trajectories in the vertical direction indicate that the particles are electrically neutral, say, uncharged.

p_d/p_∞ in Fig. 1 is the ratio of the vapor pressure on a droplet surface to that on a flat surface of the same liquid. Vapor pressure on a droplet surface increases with the decrease of droplet diameter. This phenomenon is called Kelvin effect and is given by Eq. (8). If the supersaturation of water vapor S surrounding a single isolated water droplet is larger than p_d/p_∞ , the droplet grows by condensation of surrounding water vapor. If $S < p_d/p_\infty$, that is, the surrounding supersaturation lies in below the curve p_d/p_∞ in Fig. 1, the water droplet disappears by evaporation. Thus the curve p_d/p_∞ in Fig. 1 indicates the critical relationship between droplet diameter and the surrounding vapor pressure that the droplet can be stable. In the liquid phase, however, it is not clear that Eq. (8) can be applicable.

When a temperature gradient is established in a gas, the aerosol particles in that gas are

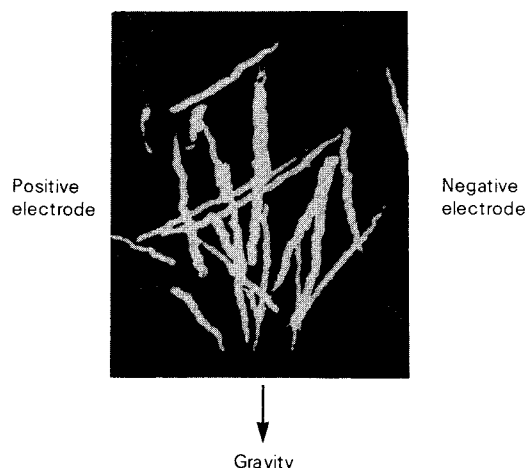


Fig. 3 Trajectories of particles in a DC electric field (particles were charged by bipolar ions)

driven from high to low temperature regions. This effect is called thermophoresis. The curve u_{th} in Fig. 1 is an example (NaCl particle in air) of thermophoretic velocity at a unit temperature gradient, that is, $1^\circ\text{C}/\text{cm}$. If the temperature gradient is $10^\circ\text{C}/\text{cm}$, u_{th} becomes ten times higher than that shown in the figure.

The curve denoted as pulse height illustrates a typical photomultiplier response of scattered light from a particle. The intensity of scattered light is proportional to six power of the particle diameter when particle size is smaller than the wave length of incident light. The curve demonstrates the steep decrease in intensity of scattered light from a particle.

3. Coagulation

Figure 4 illustrates the change in the number concentration of cigarette smoke particles with time by Brownian and turbulent coagulation. Initial particles (at $t = 0$ sec) have about $0.9 \mu\text{m}$ in geometric mean diameter, 1.4 in geometric standard deviation and 10^7 particles per cubic centimeter in concentration. Figure 4-(a) shows the number change due to Brownian coagulation in a closed chamber (vertical cylinder: 19 cm in diam. and 20 cm in height). Figures 4-(b) and (c) show the number change due to turbulent coagulation in the chamber with baffle plates stirred by six flat-bladed turbine (diameter is 9 cm)²⁾. The intensity of turbulence of Fig. 4-(c) is higher (average energy dissipation rate $\epsilon_o \approx 4 \times 10^7 \text{ cm}^2/\text{s}^3$) than that of Fig. 4-(b) ($\epsilon_o \approx 7 \times 10^6 \text{ cm}^2/\text{s}^3$). It is seen

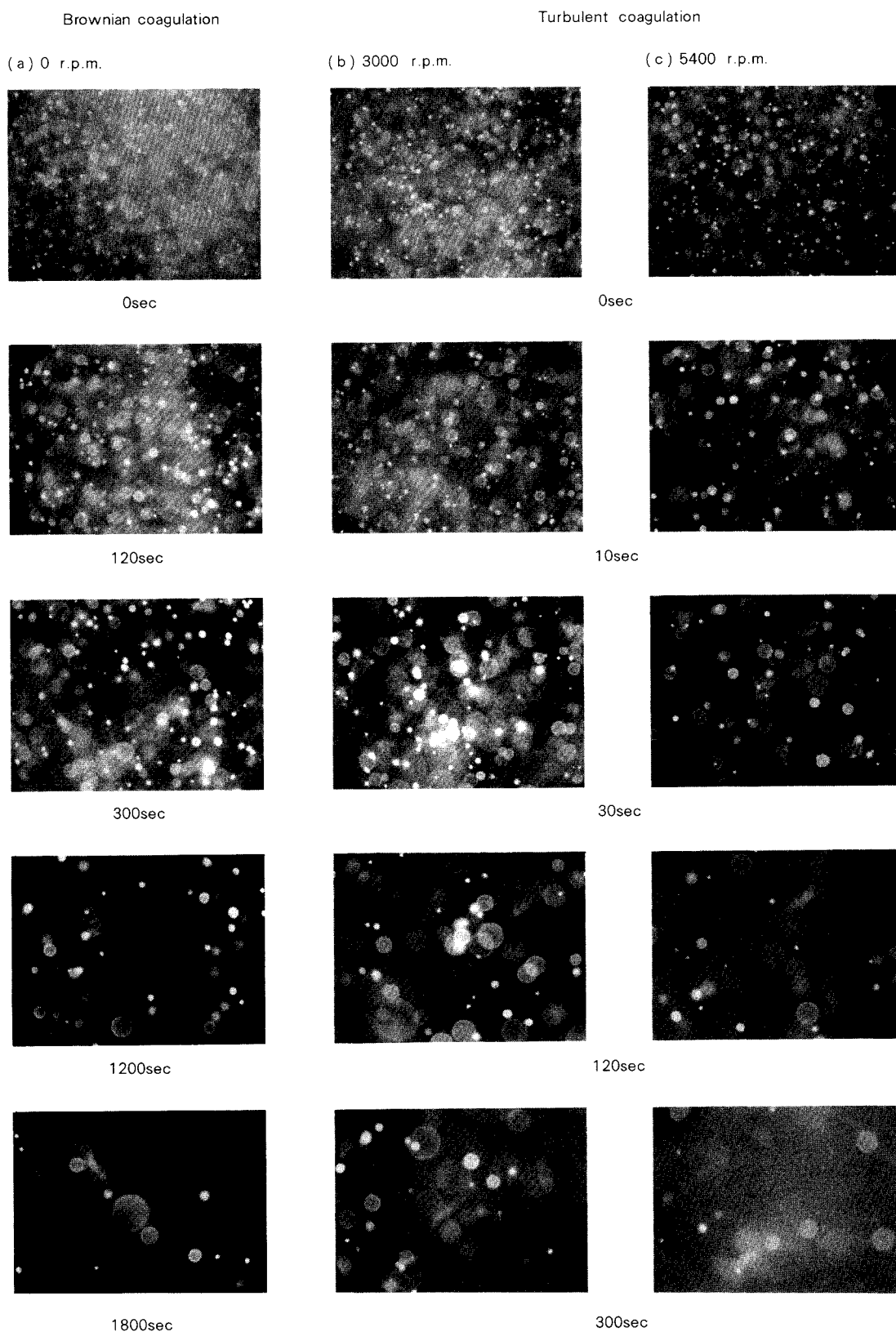


Fig. 4 Number change due to Brownian and turbulent coagulation of cigarette smoke particles.

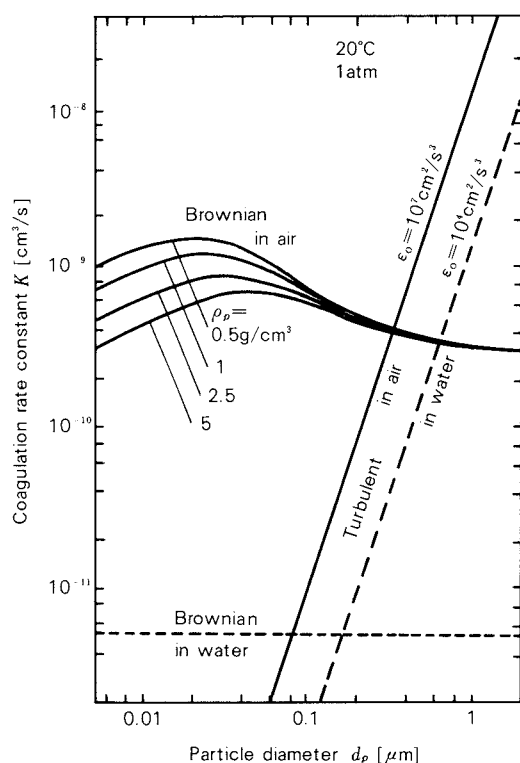


Fig. 5 Brownian and turbulent coagulation rate constants for monodisperse particles

that number change with time is significantly enhanced by turbulence.

Change in particle number concentration n with time t for monodisperse particles is expressed as follows,

$$\frac{dn}{dt} = -Kn^2 \quad (9)$$

where K is coagulation rate constant. The values of K for Brownian and turbulent coagulation in a gaseous and a liquid-phase is shown in Fig. 5. The time to reach half of the initial particle number concentration are illustrated in Table 1. The value of K for turbulent coagulation, on the other hand, is proportional to $d_p^3 \sqrt{\epsilon_0}$: this means that turbulent coagulation plays an important roll when particle size becomes large, which is illustrated in Fig. 5 for monodisperse particles and the given intensities of turbulence.

Coagulation in a liquid, mainly in water, is somewhat different from that in a gas because particles are highly charged in water in most cases. When particles are charged in the same polarity in water, the electrostatic repulsion

Table 1 Time to reach half of the initial particle concentration at 20°C due to Brownian coagulation ($d_p = 0.1 \mu\text{m}$ and $\rho_p = 1 \text{g/cm}^3$ are assumed for aerosol particles)

Particle number concentration, n_o [particle/cm³]	Time reach to $n = n_o/2$	
	in air	in water
10^{14}	14.3 μs	1.86 ms
10^{12}	1.43 ms	186 ms
10^{10}	143 ms	18.6 s
10^8	14.3 s	31 min
10^6	23.8 min	51 hr

between two particles, which is shown as the energy barrier in Fig. 6(b), prevents coagulation. The energy barrier as high as $20kT$ (k : Boltzmann constant, T : absolute temperature) is enough to prevent coagulation, which can be easily attained by adding appropriate dispersion agents in water. Submicron particles in a gaseous medium, on the other hand, can not be highly charged since ion concentration in a gaseous medium is generally low compared with that in water, and then electrical repulsion may hardly be expected, which is shown in Fig. 6(a). This means that submicron particles in a gas can not be held stable in a state of high concentration, which is one of the disadvantages of industrial particle production processes in a gaseous medium.

4. Deposition

Deposition of submicron particles suspending in a fluid onto surfaces exposed to that fluid is caused by particle diffusion, inertial motion and additional external forces such as gravitational, thermophoretic and electrostatic forces. Particle deposition caused by diffusion and electrostatic force becomes important in a submicron size range, whereas deposition by inertial and gravitational forces is less important in that range, which is obvious in Fig. 1 (see D , B_e , τ_g and u_t).

Decrease in particle number concentration of an aerosol flowing through a horizontal pipe in a laminar state, for an example, is shown in Fig. 7, where R is the pipe radius, u_{xav} the mean velocity of the flowing aerosol, x the tube length, and n_o and \bar{n} are, respectively, the particle number concentration at the pipe inlet

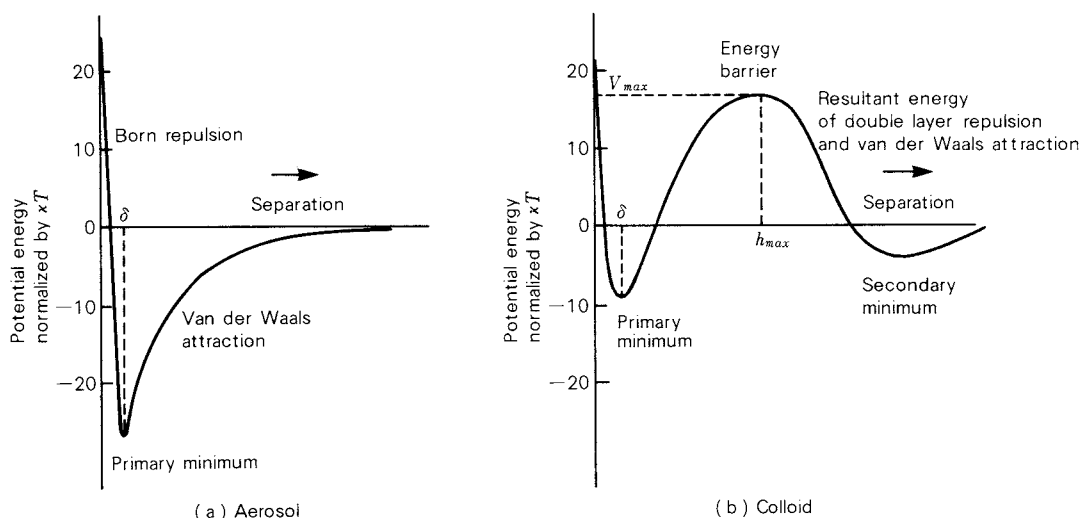


Fig. 6 Interaction energy vs. separation for combined London van der Waals attraction, double layer repulsion and Born repulsion

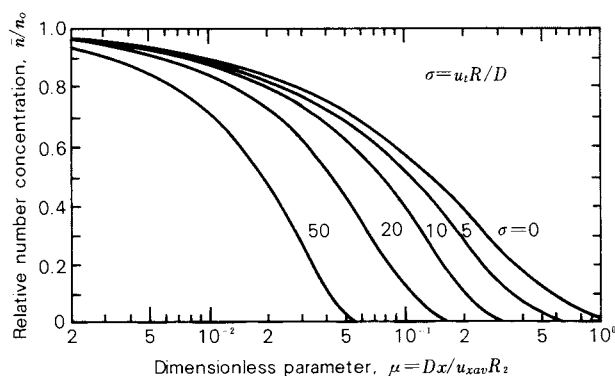


Fig. 7 Decrease in number concentration of an aerosol flowing through a horizontal pipe in a laminar state

and the pipe outlet. The curve of $\sigma = 0$ in the figure indicates the number decrease due to Brownian diffusion alone, and the other curves indicate those accompanied by gravitational sedimentation.

Another example which may be important for particle production processes in gaseous media is shown in Fig. 8. The plots are the experimental results obtained in a closed, cylindrical vessel similar to the former section. The abscissa β in the figure is deposition rate constant which is a measure of particle deposition rate, and is defined as follows,

$$\bar{n}/n_o = e^{-\beta t} \quad (10)$$

where n_o and \bar{n} in this case are the number

concentration of aerosol particles at time $t = 0$ and at time t , respectively. The dashed line and the corresponding plots are the particle deposition rate constant where a natural convective flow exists throughout the vessel. The other solid lines are for those turbulent flow existence.

N_s in the figure is the revolution of stirrer and ϵ_o the corresponding average energy dissipation rate. It is seen in the figure that turbulence clearly enhances particle deposition on walls and that Brownian deposition is predominant in the smaller size range whereas deposition due to gravitational settling is predominant in the larger size range. The plots in the figure are obtained by the present author and his co-workers³⁾, and the lines are those calculated from the theory proposed by Crump and Seinfeld⁴⁾.

If there exists a temperature gradient in the vicinity of a wall which has lower temperature than a fluid, thermophoresis shown in Fig. 1 enhances particle deposition on the wall.

Particle deposition is also enhanced if particles are charged in opposite polarity to a wall. If aerosol particles are charged in bipolarity, a wall charged in either polarity can enhance deposition of particles charged in opposite polarity to that wall.

The deposition mechanism of particles suspending in a liquid is essentially the same as that in a gas if the electrical repulsion

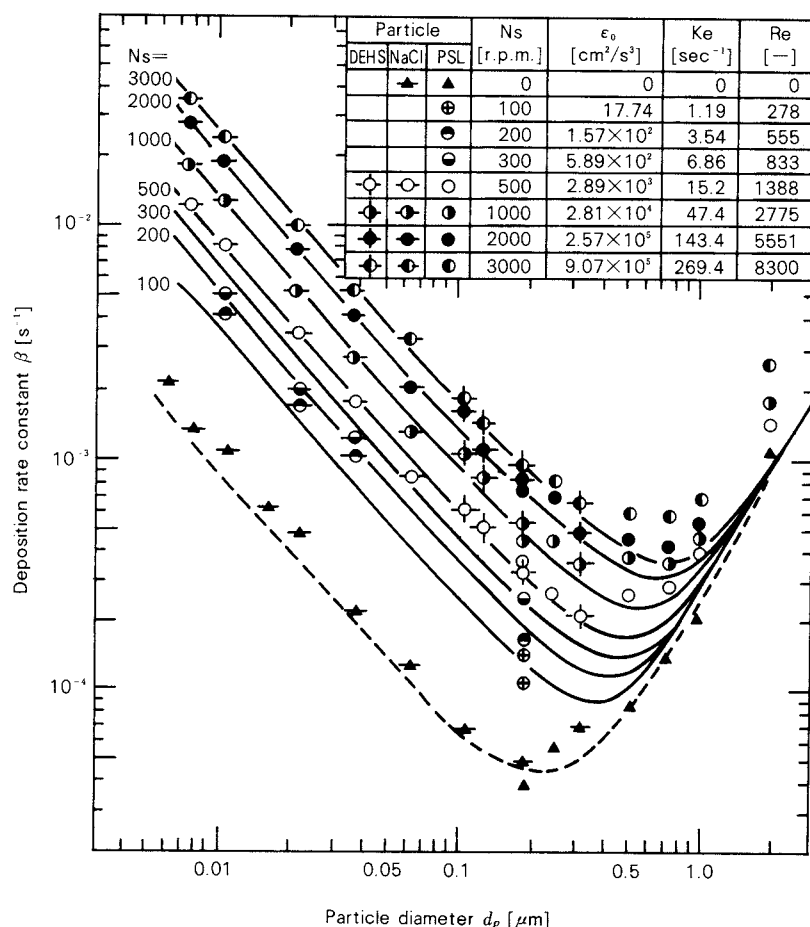


Fig. 8 Deposition rate constant of particles in a stirred vessel

shown in Fig. 6-(b) is not strong. However, particle deposition in a liquid medium is thought to be less important than in a gaseous medium, because, in a liquid medium, electric double layer repulsion is not neglected in most cases, particle diffusion coefficient, gravitational settling velocity and inertial effect are small, and because re-entrainment of particles once caught at walls takes place rather easily compared with that in a gaseous medium.

5 Conclusion

Size-dependent behavior, mainly dynamic behavior, of submicron particles suspending in a fluid has been summarized. And then the topics on coagulation and particle deposition on walls have been outlined. Another interest-

ing topics on submicron particles from an industrial point of view will be gas- or liquid-to-particle conversion, that is, particle production process, but unfortunately it is too complicated and has not well been understood for the time being.

References

- 1) Adachi, M., Y. Kousaka and K. Okuyama: *J. Aerosol Sci.*, **16**, 109 (1985).
- 2) Okuyama, K., Y. Kousaka, Y. Kida and T. Yoshida: *J. Chem. Eng. Japan*, **10**, 142 (1977).
- 3) Okuyama, K., Y. Kousaka and T. Hosokawa: "Aerosols" ed. by B.Y.H. Liu et al., 857 Elsevier (1984).
- 4) Crump, J.G. and J.H. Seinfeld: *J. Aerosol Sci.*, **12**, 405 (1981).

Yoshiro Funakoshi

Kyoto Institute of Powder Technology Ltd.*

1. Introduction

Granulating processes of pharmaceutical materials can be broadly classified into dry and wet processes. In the dry process, materials are densified and compressed in a confined space by application of external force, while in the wet process, they are agglomerated by coagulative force between particles. The performance of the former is significantly affected by the stress distribution in the compacts and that of the latter by the packing structure of solid and liquid, that is, the ratio of liquid to solid supplied and their distributions.

The author has been developing a tableting machine which can effectively reduce *capping* in actual production and a powder coating granulator which can provide comparatively uniform distribution of solid and liquid. By using these equipments, capping phenomena and solid-liquid packing structure have been investigated and analyzed. This paper describes the essentials of these results.

2. Stress distribution in tablets and capping phenomena

2. 1 Analysis of primary factors influencing capping

Capping phenomena have been studied by Train¹⁾, Long²⁾, Shotton³⁾, and other workers for many years. However, few of their fruits can be applied to practical production of a tablet which is performed by rotary tableting machine within such a short period of time as 0.02 to 0.1 seconds. The author has investigated the primary factors influencing capping which are listed in **Table 1**. A part of the results will be described below.

(a) Iterative compression

Compressive strength and capping generation of tablets were determined by two different compressing methods. Two tableting machines (A and B) were used which showed different characteristics in tableting. One comprises the iterative compressing formation which was carried out by A-equipment first and then by B-equipment, while the other comprises the converse procedure. The results obtained in this test are listed in **Table 2**. It can be estimated that capping would not take place in a compressing stage but in an ejecting one since the same operating conditions were employed in both stages. The difference in tableting performance between these two equipments might possibly result from the slight difference in mechanism of the ejecting stage.

(b) Ejection under pressure

The author has devised a specific rotary tableting machine with pressurized ejection mechanism, which is schematically illustrated in **Fig. 1**. This machine allows tablets to be discharged out of a die in keeping application of compression pressure from 1 to 10 MPa with upper and lower punches after the main compression. The compressing force during ejection can be adjusted by sliding *wedge-type pressure adjuster* and by moving *guide rail of the lower punch* up and down.

Figure 2 shows a drilling load measuring apparatus which consists of a load cell ①, a sample holder ②, elevating equipment ③, a drill bit ④, and a recorder ⑤. Typical drilling load distributions of the tablets obtained by the machine shown in **Fig. 1** are illustrated in **Fig. 3** where the result of the pressurized ejection is compared with that of the non-pressurized ejection. It is found that crack occurred at 2 mm depth from the surface.

Summarizing the results obtained from these findings:

1) The primary factors influencing capping of

* 21, Shichiku, Nishimonomoto-cho, Kita-ku, Kyoto, 603
TEL. 075 (491) 0502

Received April 17, 1985

Table 1 Factors related to capping in compressed tablets

Physical process	Capping factor	Binding force of powder	Crack of compact	
			included air	Residual stress
Compression stage	Pre-compression	Degree of compression	○	
		Pre-compressing period	○	
	Main compression	Maximum compressing force		○
		Compressing period		
		Increasing rate of compressing force	○	
		Decreasing rate of compressing force		○
Ejection stage	Ejection of compact	Stress distribution in compact		○
		Displacement and displacing speed of upper and lower punch		○
		Friction between compact and die wall		○

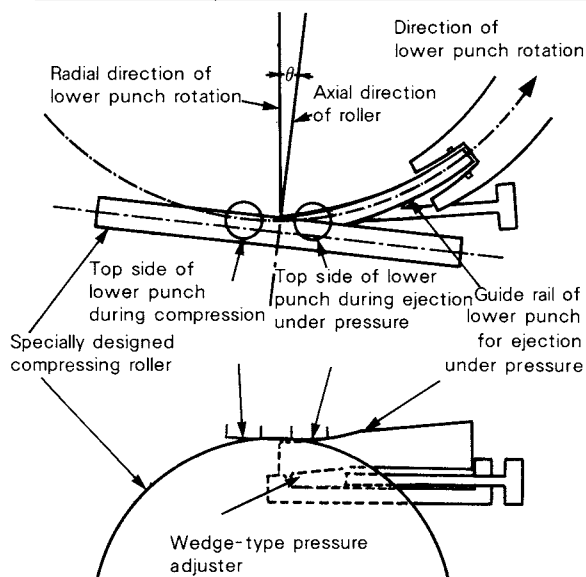


Fig. 1 Mechanism of ejection under pressure

Table 2 Compressive strength and capping percentage

1st compression	2nd compression	Compressive strength	Capping percentage
A	B	8.3 N	100%
B	A	50.8 N	0%

the compacts produced by a rotary tableting machine are involved in the ejection stage.

2) The reduction of capping can be effectively achieved by the method in which the tablets are discharged out of a die under the remaining compression of 1 to 10 MPa with an upper and lower punch.

2. 2 Stress analysis in capping generation

(a) Compressive stress during compression

Generation of capping may be considered to

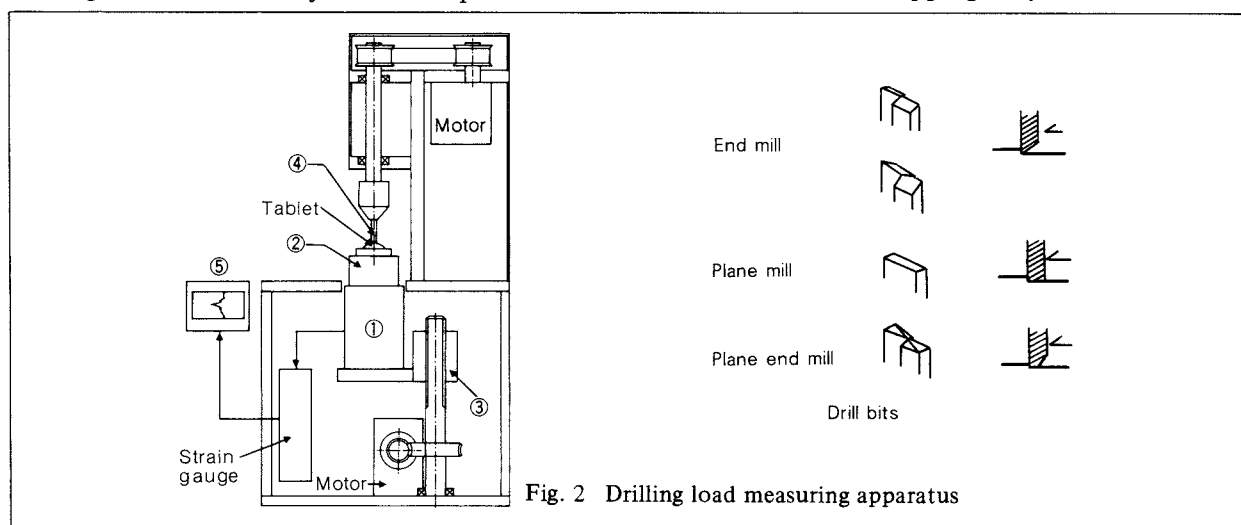


Fig. 2 Drilling load measuring apparatus

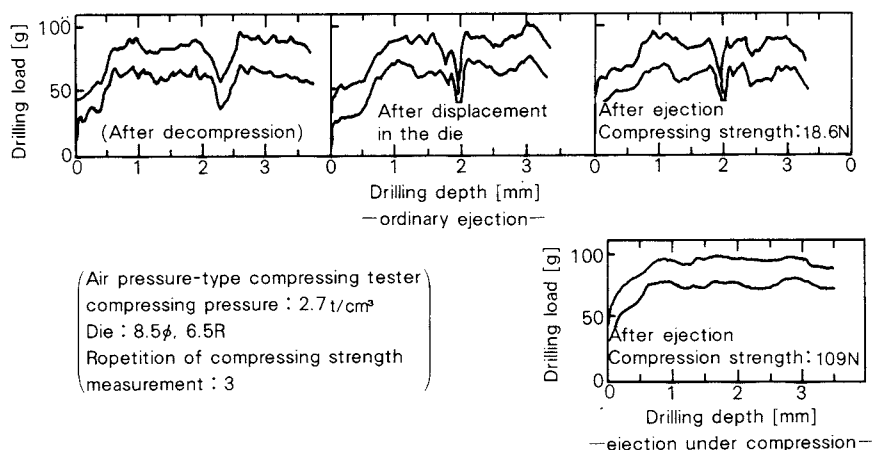


Fig. 3 Variation of drilling load distribution during ejection

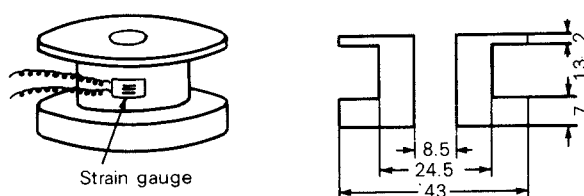


Fig. 4 Test die for measuring die wall stress

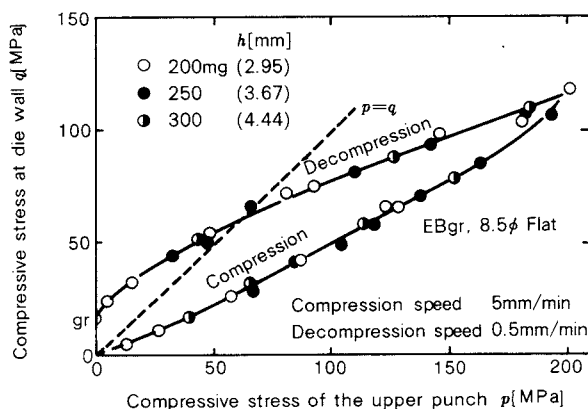


Fig. 5 Compressive stress of the upper and die wall during compression and decompression stages

be due to the stress condition during decompression. The author measured the compressive stresses in the die shown in Fig. 4 at the upper punch and the die wall during compression and decompression periods. As shown in Fig. 5, the stress q_r at the die wall still exists after complete release of the pressure applied by the upper and lower punch.

Figure 6 shows the effect of the curvature radius of a concave tablet on the residual stress

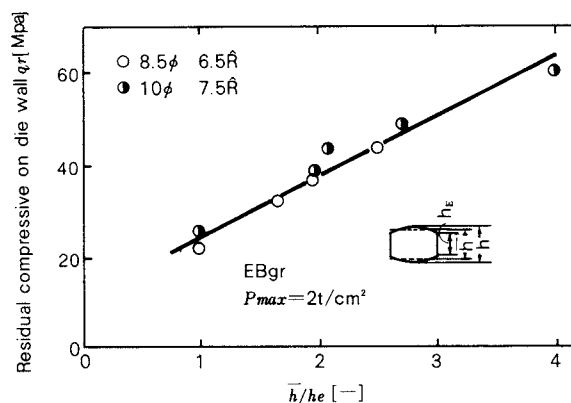


Fig. 6 Residual, compressive stress of die wall (Using concave punch)

at the die wall. As can be seen from Fig. 6, the residual stress at the die wall increased as the ratio \bar{h}/h_E increased, that is, the radius of curvature decreased. It has been empirically known that capping increases as the curvature radius decreases. In view of these facts, it may be considered that capping is closely related to the residual stress at a die wall.

(b) Residual stress at die wall q_r and extent of capping

If the compressive stress at a die wall is different from the compressive stress of an upper punch, a shear stress is generated in the body of the tablet. The maximum shear stress in the tablet may be given by

$$\tau_{\max} = \frac{(\text{Compressive load applied by upper punch}) - (\text{Stress at die wall})}{2}$$

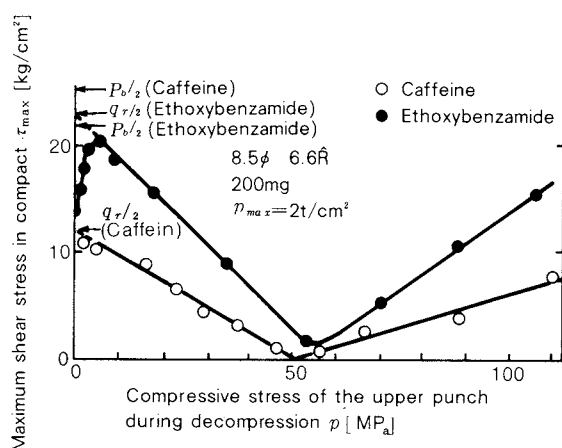


Fig. 7 Maximum shear stress in compact during decompression

The value of τ_{max} during decompression was examined for two materials: caffeine and ethoxybenzamide, which are regarded capping-poor and capping-rich, respectively. The results are shown in Fig. 7. τ_{max} becomes $q_r/2$ when the compressive force of the upper punch is completely released.

On the other hand, Fig. 8 shows the compressive stress-compressive strain curves of the cylindrical tablets of caffeine and ethoxybenzamide, which have been prepared by tableting each 1 gram of the powders by a circular die of 1 cm² cross sectional area and a flat punch. From the curve in Fig. 8, the maximum compressive strength of the tablets can be determined as P_b and then the maximum shear stresses in the tablets at fracture as $P_b/2$. By comparing the value of $P_b/2$ with those of $q_r/2$, the maximum shear stresses in the tablets under complete decompression give the relations:

$$\frac{q_r}{P_b} = 1 \quad \text{for ethoxybenzamide}$$

$$\frac{q_r}{P_b} < 1 \quad \text{for caffeine}$$

These findings have proven well that the capping tendency of ethoxybenzamide is high and that of caffeine low.

(c) Capping tendency and q_r/P_b

Consider the ratio of the compressive strength of the tablet obtained by ejection under no pressure, H , to the one under a pressure, H_0 , as the specific strength, H/H_0 . The relationship

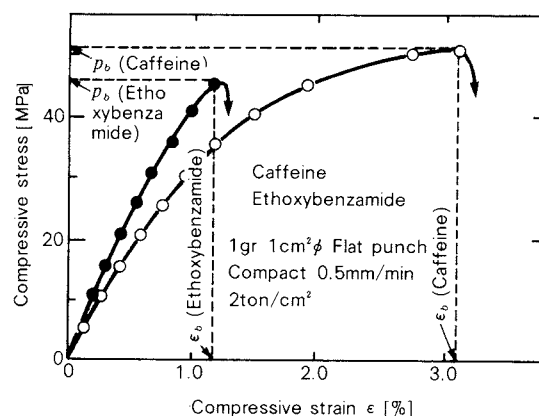


Fig. 8 Compressive fracture test

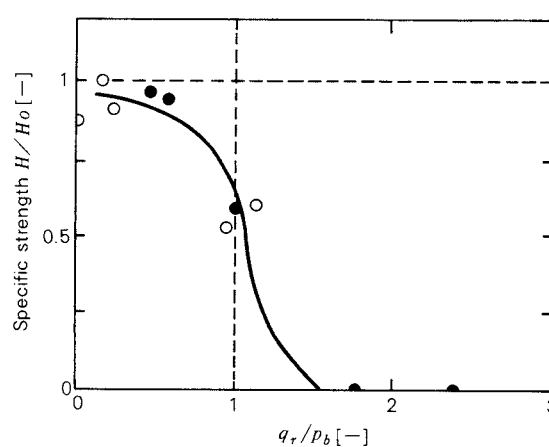


Fig. 9 q_r/P_b and capping

between H/H_0 and q_r/P_b for several materials are shown in Fig. 9. It is found that the specific strength varied largely at $q_r/P_b = 1$. This implies that the degree of capping can be estimated by the value of q_r/P_b . It is emphasized, therefore, that a practical design for a tablet requires a suitable selection of powder prescription and tablet shape.

3. Powder coating granulation and packing structure of solid-liquid system

3. 1 Necessary condition for powder coating granulation

The conditions required for powder coating granulation are considered to be:

- 1) Mixing and dispersion of solids and liquids
- 2) Optimization of moisture content
- 3) Consolidation by tumbling

The first is how uniformly coating liquids and powders can be dispersed in the bulk of solids; the second is the ratio of liquid to solid

Table 3 Processes, equipment, and operating conditions required for powder coating granulation

Required item	Required process	Equipment	Operating condition
Mixing and dispersion of liquid	Feed of small liquid droplets Shear mixing { <ul style="list-style-type: none"> Large shearing force Uniform shearing — without stagnation zone — without local excessive shearing Large mixing speed 	Spraying equipment	Liquid pressure Liquid/air flow rate Position of nozzle
Mixing and dispersion of powder	Circulating flow formation Shear mixing { as above Circulating flow formation	Coating granulator	Quantity fed Rotating speed
Optimization of moisture content	Programmed feeding of powder and liquid Program control for moisture content of particle surface	Powder and liquid feeding system Program control system for moisture content of particle surface	Control program Control program
Tumbling compaction	Moderate tumbling compaction	Coating granulator	Quantity fed Rotating speed

in the bulk of solids; the third is an importance of tumbling for suitable consolidation. The required equipments and conditions are listed in Table 3.

3. 2 Development of coating granulator

(a) Coating granulator

A configuration of the granulator which has been developed after trial and error is schematically illustrated in Fig. 10. This configuration was found to provide an excellent performance on smooth convective mixing without any local stagnation in the granulator, which was called *CF equipment* by the author. Typical mixing characteristics are shown in Fig. 11, which indicates that the mixing was finished within 20 to 30 seconds.

(b) Spraying of coating liquids

The ratio of air to liquid flow rates is of great importance for spray coating liquids with concentric two-fluid nozzle system. It is because as the droplet diameter is larger, the generation rate of particle coagulation becomes larger. As can be seen from the relationship

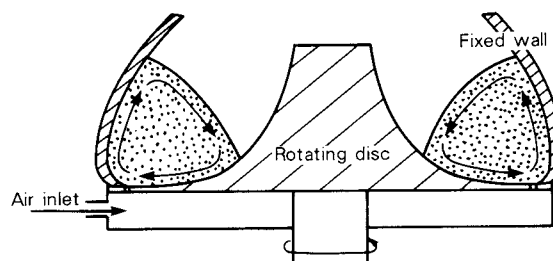


Fig. 10 Centrifugal fluidization-type coating equipment (CF equipment)

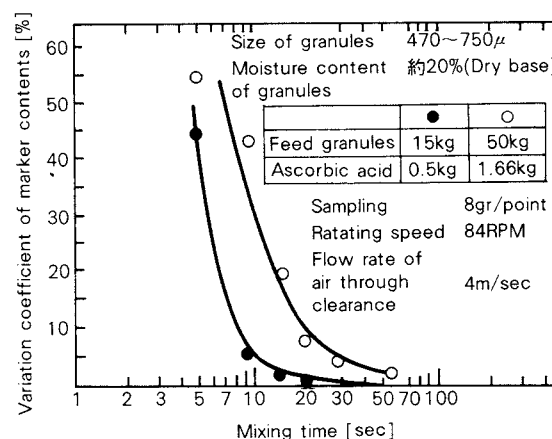


Fig. 11 Mixing characteristics of CF-1000 equipment

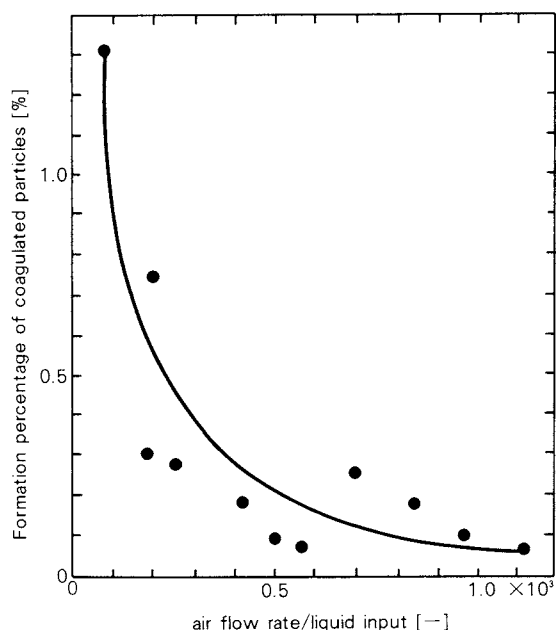


Fig. 12 Operating condition for spray vs. formation percentage of coagulated particles

between the air-to-liquid ratio and the generation rate of coagulated particles shown in Fig 12, the decrease in droplet size requires an increase in air-to-liquid ratio.

(c) Control system of moisture content on particle surface

To keep the mixture at its optimum wet condition, the granulator is required to be equipped with the specific control system which consists of measuring moisture content of particle surface and determining the feed rate of spraying liquid or powder. It is well known that powder bed becomes an electrical conductor to some extent if spraying liquid is an aqueous solution. Hence the electrical conductivity of the powder bed was used as a measure of moisture content of the particle surface. The system established is schematically indicated in Fig. 13.

3. 3 Powder coating granulation

Experimental data with the granulation established by the author and operated under the automatically controlled conditions are listed Table 4.

3. 4 Optimum ratio of solid to liquid

Another experiment using this granulator was also conducted to determine the optimum ratio of liquid to solid for practical operations.

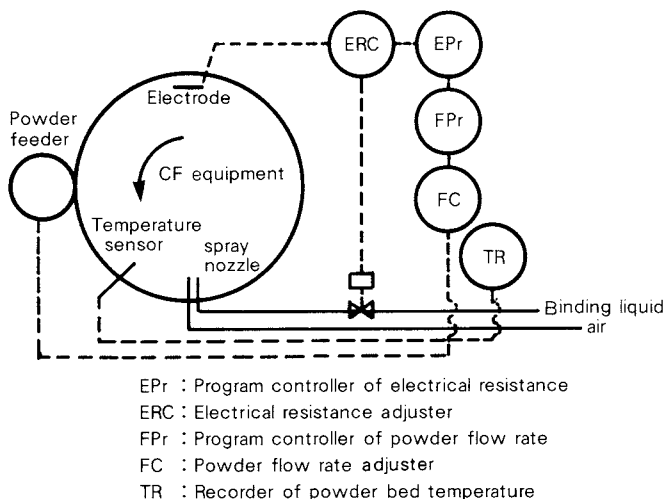


Fig. 13 Control system for powder coating granulation

The liquid used was a saturated syrup solution and the result is listed in Table 5.

3. 5 Occupation ratio of liquid among particles and optimum ratio of solid to liquid

The specific volume of wet compact φ_{01} was determined by gradually compressing the particulate material which had been preliminarily milled in a 100 cm² container with liquid at a given liquid-to-solid ratio of 1.5 kg/cm². Its porosity ϵ_{01} is calculated by the following form:

$$\epsilon_{01} = \frac{\varphi_{01} - \frac{L + S \frac{1}{\rho_p}}{S + L \rho_s}}{\varphi_{01}}$$

where L : Feed of syrup [cm³]
 S : Feed of powder [g]
 ρ_p : True density of powder [g/cm³]
 ρ_s : Density of syrup [g/cm³]

The ratio of a void filled with water among particles of a wet material in consideration of the solubility, Ψ , is expressed as

$$\begin{aligned} \Psi &= \frac{L(1 + \lambda \frac{1}{\rho_p})}{(S + L \rho_s) \varphi_{01} \epsilon_{01} + L(1 + \lambda \frac{1}{\rho_s})} \\ &= \frac{\frac{L(1 + \lambda \frac{1}{\rho_p})}{S - \lambda L}}{\frac{(S + L \rho_s) \varphi_{01} \epsilon_{01}}{S - \lambda L} + \frac{L(1 + \lambda \frac{1}{\rho_p})}{S - \lambda L}} \quad (2) \end{aligned}$$

Table 4 Experimental data of size growth for reproducibility

No.	Feed of nucleus	Sprayed amount of powder	Sprayed amount of binding liquid	Good-quality percentage	Average diameter	Particle distribution σ	Nucleus	
							Average diameter	Particle distribution σ
	[g]	[g]	[cm ³]	[%]	[μ m]	[μ m]	[μ m]	[μ m]
1	2250	1960	865	98.75	760	60	562	60
2	2250	1960	865	98.15	770	50		
3	2250	1960	855	98.58	760	50		
4	2250	1960	870	99.52	750	50		
5	2250	1960	865	99.19	760	60		
Ave.			865	98.84	760	54		
σ			4.5	0.48	3	2		

Table 5 Optimum ratio of liquid to solid of several powders

Powder	Powder sugar	Cornstarch	Ascorbic acid	Nicotinic acid	Fine crystallized cellulose
Optimum ratio of liquid to solid	0.17	0.52	0.16	0.18	9.9

As seen from Eq. (2), the occupation ratio Ψ can be calculated from the specific volume φ_{01} and the ϵ_{01} obtained from Eq. (1). Plots of the occupation ratio against the ratio $L(1 + \lambda/\rho_p)/(S - \lambda L)$ are shown in Fig. 14, in which the optimum granulating condition is expressed as the symbol \oplus .

It is obvious from this figure that the optimum condition would be involved within 55 to 65% of Ψ . The author could verify this tendency irrespective of the kind of liquid or powder materials. This suggests that powder coating granulation could be optimized in actual operation for most cases if the occupation ratio Ψ is kept within 55 to 65%.

References

- 1) Train, D.: *J. Pharm. Pharmacol.*, **8**, 745 (1956).
- 2) Long, W.M.: *Powder Met.*, **6**, 73 (1960).
- 3) Shotton, E.: *J. Pharm. Pharmacol.*, **25**, suppl., 202S (1971).

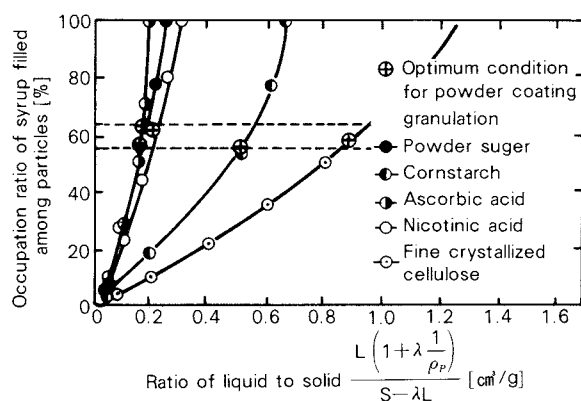


Fig. 14 Ratio of liquid to solid vs. occupation ratio of syrup filled among particles

Informational Articles

The Symposium on Powder Technology

The Party of Powder Technology (Japan) held the 18th symposium at Kousei-Nenkin Kaikan in Osaka on August 8th, 1984. This symposium was given with the theme "Production and Characteristics Measurement of Ultra-

fine Particles".

Many participants (about 230) listened eagerly to the lectures for over 8 hours. The detail of the lectures are listed below;

Session 1 To what extent is size reduction possible?

Chairmanship : Genji Jimbo (Nagoya University)

- | | |
|---|--|
| • To what extent is size reduction possible? | Yoshitaka Kuwahara
(Government Industrial Research Institute, Nagoya) |
| • To what extent is wet classification possible? | Naoya Yoshioka
(Professor emeritus of Kyoto University) |
| • Classification of fine particles by wet centrifuge | Zennosuke Tanaka
(Okayama University) |
| • Practical operation of closed-circuit grinding system | Eiichi Onuma
(Onoda Cement Co., Ltd.) |

Session 2 Characterization of sub-micron particles

Chairmanship : Tetsuo Yoshida (Chubu University)

- | | |
|--|---|
| • Survey of size analysis for sub-micron particles | Masafumi Arakawa
(Kyoto Institute of Technology) |
| • To what extent is particle size analysis possible? | Yasuo Kousaka
(University of Osaka Prefecture) |
| • Size analysis for sub-micron Particles | Genji Jimbo
(Nagoya University) |
| • Practical approach to sub-micron particles | Tohei Yokoyama
(Hosokawa Micromeritics Laboratory) |



Photos: The 18th symposium on powder technology in 1984.

Academic publication concerning powder technology in Japan (printed in 1984)

Journal of the Society of Powder Technology, Japan Vol.21 (1984)

Title	Author(s)	Page
• Measurement of Particle Orientation Distribution by a Stereological Method	K. Kanatani	3–10
• Effect of Powder Properties in the Fractional Recovery Curves in a Fine Particle Size Air Classifier	T. Suh, T. Shibata, J. Tsubaki and G. Jimbo	11–17
• Prevention of the Scattering of Stored Granular Materials in the Wind	T. Kano, F. Takeuchi, K. Jinno and A. Fujiwara	18–24
• The Effect of Agglomeration on the Flowability of Powder	M. Hirota, Y. Iwamoto, T. Kobayashi and T. Oshima	69–74
• The Influence of pH and the Concentration of Dispersants on the Coagulation and Dispersion of Fine Particles in Water	H. Hirose, M. Tani, N. Yamada and E. Abe	74–80
• Relationships between the Efficiency of Crushing and the Handling Condition of Several Wood Crushers	H. Endoh, H. Takahashi, K. Yamaguchi and K. Endoh	80–86
• An Estimation of the Wall Friction in Vertical Air-Solid Two-Phase Flow	Y. Morikawa and T. Tanaka	87–94
• The Improvement of An Annular Shear Tester and Its Performance	A. Gotoh, M. Kawamura K. Matsushima and H. Tsunakawa	131–136
• Expansion and Contraction Behavior of a Powder Bed in a Shear Process	M. Hirota, T. Kobayashi O. Sano and T. Oshima	137–142
• Study of Numerical Schemes for Stereological Estimation of Particle Size Distribution	K. Kanatani and O. Ishikawa	143–152
• The Effect of Particle Size Measurement on Classification Efficiency Assessment	Z. Tanaka, S. Kaseno and T. Takahashi	153–157
• Particle Flow-Pattern in a Storage Vessel of a Table Feeder	Z. Han, H. Masuda and T. Kadowaki	199–205
• Study on Granulation by the Fluidized Bed Granulating Method (1) – Preliminary Investigation on Explaining the Defects of Conventional Method and Their Improvement –	Y. Sagawa and T. Sakamoto	206–211
• Study on Granulation by the Fluidized Bed Granulating Method (2) – Investigation of the Granulating Conditions to Promote Compactness, Smoothness and the Growth of Granules –	Y. Sagawa and T. Sakamoto	212–217
• Electrification of Metal Powder Particles Flowing out through Inclined Pipes under Frictional Conditions	T. Sakai	259–265
• A new Estimation Method of the Powder Yield Locus of the Deposited Dust Layer in Electrostatic Precipitators and in Bag Filters	K. Makino, M. Yamada M. Kawahara and K. Kuramitsu	266–275
• The Pore Structure of Silica Gels Surface-treated with Organosilyl Chlorides	H. Utsugi, A. Endoh, N. Suzuki T. Yabiki and T. Ono	275–281
• Effect of Mulling State on Granule Yield and Properties of Granules	K. Terashita, T. Kimura and K. Miyanami	327–333
• A Study on Granulation by the Fluidized Bed Granulating Method (3) – The Comparison of the Granulating Mechanism and Granule Properties of the Conventional Method with those of the New Method –	Y. Sagawa and T. Sakamoto	393–398

Title	Author(s)	Page
• On the Principle of Similarity in the Mechanics of Granular Materials – 1st Report: Theoretical Foundation—	T. Nagao	398–405
• On the Principle of Similarity in the Mechanics of Granular Materials – 2nd Report: Its Confirmation by an Experiment of a Small and a Medium Scale Model of Silo	T. Takeuchi, T. Nagao, Y. Hatamura and N. Nakajima	406–418
• The Effect of the Reynolds Number on the Permeability Coefficient of a Porous Media	T. Issiki and T. Yaginuma	463–469
• Impact Test of a Single Particle Using a Drop Weight Type Apparatus, Part III – The Fragment Size Distribution of the Fractured Product and Fatigue Fracture Under Impact Loading—	Y. Kuwahara, F. Saito and S. Yashima	469–475
• Production of Fine Powders by an Agitating Mill	S. Morohashi, N. Ooi and S. Yashima	476–482
• The Spray Drying of Slurries of Fine Particles and the Strength of Spray-dried Particles	N. Yamada and H. Hirose	482–489
• Mathematical Simulation of Controlled Release from Matrix-type Drug Delivery Systems	K. Tojo	490–495
• Electrical Conductance of a Small Regular Packing System of Conducting and Insulating Particles	Y. Yoshimura and T. Yoshida	541–545
• Dynamic Characteristics of Grinding Mills	T. Tanaka	553–558
• The Optimum Conditions of Oscillating Air Applied to Sieve Fine Powders	J. Hidaka, N. Nakamura and S. Miwa	558–564
• Mechanics of Grinding Media in Vibration Mill	C. Boyi	615–620
• Analysis of Vibration Mill	C. Boyi	620–626
• Development of a Fineness Measuring Air Classifier (II)	Y. Yamada, M. Yasuguchi, H. Murakami, Y. Sato H. Tomiyasu, Y. Ohta and K. Iinoya	627–632
• Effects of Measurement Conditions on Particle Sizing in the Laser Diffraction Technique – On the Spatial Density, Sampling Position and Optical Setting —	M. Nakayama, T. Araki and C. Takahashi	691–696
• Preparation of Ultrafine Ceramics Particles by Hydrogen, Nitrogen and Oxygen Plasmas	M. Uda, S. Ohno and H. Okuyama	747–752
• Measurement and Classification of Submicron Particles by Electric Mobility Analyzer and Diffusion Battery	C. Kanaoka, Y. Otani and H. Emi	753–758
• Generation of Metal Ultra Fine Particles Via Gas-Phase Chemical Reaction	A. Yoshizawa and K. Otsuka	759–767
• A New Apparatus for Particle Size Measurement by the Method of Centrifugal Sedimentation	M. Arakawa, G. Shimomura A. Imamura, N. Yazawa, N. Kaya and H. Kitai	768–773

Funsai (The Micromeritics) No. 29 (1985)

Title	Author(s)	
• Fine Grinding of Silicon Nitride Powder and Mechanochemistry	Y. Kanno	4–8
• The Residue of Powder on Discharge Storage Vessel with Air-blowing Nozzles	R. Utsumi	9–14
• A Simple Estimate of the Rate Controlling Step in a Fluidized Combustion Bed	I. Tanaka	15–20
• A New particle Size Distribution Apparatus Based on Unbalance by Centrifugal Sedimentation	M. Arakawa, G. Shimomura A. Imamura, N. Yazawa N. Kaya and H. Kitai	21–27
• Relationship between Mechanical Strengths and Solidified Forms for Sulphur Melts	I. Sekiguchi and H. Nakada	28–37

Kagaku Kogaku Ronbunshu Vol. 10 (1984)

Title	Authors	Page
• Measurement of Forces of Adhesion of Powders to Glass Plate by Centrifugal Method	S. Sano, F. Saito and S. Yashima	17–24
• Relationships between Particle Size and Fracture Energy for Single Particle Crushing	Y. Kanda, F. Saito, Sano and S. Yashima	108–112
• Improvement of Suction Nozzle Performance in Pneumatic Conveying of Granular Materials	T. Kano, F. Takeuchi, S. Iida and N. Mima	139–144
• Kinetic Analysis of Comminution in a Screen Mill	Y. Kuga, J. Koga and K. Yamaguchi	204–210
• Fine Grinding of Petroleum Pitch with Grinding Aids	S. Yashima, T. Yamamoto H. Hirota and Y. Arai	273–279
• Performance of K-type Classifier	K. Yoshie, A. Suganuma H. Yamamoto and R. Aoki	323–329
• Aerosol Classification Performance of Rectangular Jet Virtual-Impactor	H. Masuda, E. Yasuki and S. Kawaguchi	561–567
• An Experimental Study of the Technics of Reduction of Power Consumption for Pneumatic Conveying of Granular Materials – Effective Utilization of Air in Plug-type Pneumatic Conveying and Optimum Forms of Bends –	T. Kano, M. Utsumi, F. Takeuchi, H. Kuroyanagi and H. Kawade	568–573
• Static Stress Conditions of a Cohesive Powder in Bins	K. Matsumoto, A. Suganuma and R. Aoki	667–674
• Estimation of Void Fraction in a Three Component Random Mixture of Spheres	M. Suzuki, A. Yagi T. Watanabe and T. Oshima	721–727
• Shearing Direction Dislodgement of Deposited Dust Layer on Fabric Filter	M. Naito, J. Tsubaki and G. Jimbo	744–750

Journal of Chemical Engineering of Japan Vol. 17 (1984)

Title	Authors	Page
• Discrimination of Shape of Particles Separated by Inclined Rotary Disk and its Evaluation by Linear Discriminant Function	S. Endoh and K. Yamaguchi	20–26
• Effects of Feed Particles Shapes on Jet Pulverization	T. Honma, M. Hasegawa and Y. Kanda	221–223

Journal of the Society of Materials Science, Japan Vol. 33 (1984)

Title	Authors	Page
• Compaction Behavior of Powder at High Temperature	M. Hirota, T. Oshima T. Ishihara and A. Kanazawa	1125–1129
• Internal Friction Factor and Tensile Strength of Fine Coals	K. Terashita, T. Konishi K. Furubayashi and K. Miyanami	1130–1134
• Simultaneous Operation of Granulation and Separation in Horizontal Rotating Conical Vessel (An Experimental Study on Closed Circuit Granulation)	M. Sugimoto and Nakamura	1135–1140
• A New Apparatus for Measuring Particle Size Distribution Based on Centrifugal Sedimentation	M. Arakawa, G. Shimomura, A. Imamura, N. Yazawa, T. Yokoyama and N. Kaya	1141–1145

Journal of the Japan Society of Powder and Powder Metallurgy Vol. 31 (1984)

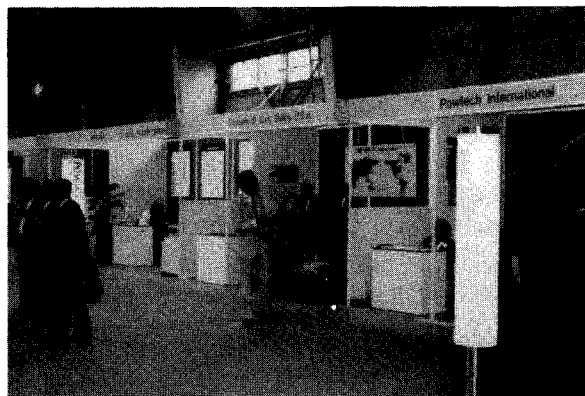
Title	Author(s)	Page
• Effect of Binary Powder Mixing in Sintering of Fine Silicon Carbide	H. Tsuda, J. Hojo and A. Kato	1–7
• Effect of Sampling Amounts on Apparent Density of Metallic Powder	J. P. Dai and X. W. Lai	8–13
• Measurement of Oxidation Amount of TiH ₂ Powder Pulverized by Ball-Milling	K. Hayashi and M. Itabashi	80–82
• On the One Dimensional Transmission Properties of the Bulk Density in Mobilized Particulate Materials inside an Inclined Tube	K. Makino, M. Yamada S. Funaki and K. Kuramitsu	122–124
• Incidence-Reflection Condition of a Loose Bulk Density Zone to a Solid Wall in Particulate Materials	K. Makino, M. Yamada A. Higashiyama and K. Kuramitsu	125–129
• Surface Treatment of Silica Gel with 1-Pentanol through Gaseous Flow Method	N. Suzuki, A. Endo and H. Utsugi	202–207
• The Surface-Treatment of Silicon Nitride with Alcohols and its Contribution to Mixing with Paraffine	H. Utsugi, A. Endo N. Suzuki and K. Ono	260–265

Title	Authors	Page
• Preparation of Transparent Ultrafine Titanium Oxide	S. Ito, M. Tanaka, K. Shiragane and T. Kuwahara	305–308
• Accuracy in the Measurement of Characteristic Particle Size with Grind Gauge	Y. Murakami, G. Chung K. Kawaguchi, T. Hirose and Y. Akimoto	435–440
• Classification Effect in a Roll Mill	Y. Murakami, G. Chung K. Kawaguchi, T. Hirose and Y. Akimoto	635–642

Powdertec Japan '84

The 5th Powdertec Japan, the biennial powder and bulk solids exposition, was held in Tokyo on October 15 to 19 in 1984. The international trading center (Harumi, Tokyo) housed the event where 159 exhibitors and about 70,000 visitors including many foreigners came together in a marketplace of tools and know-how. At this show, many new and noteworthy products were displayed: unit operation for powder processing; bulk solids handling; analyzing apparatus and controlling system; powder coating; and other related equipments.

The Powder Technology Congress '84 was also held at Hotel Urashima located near the exhibition center in the same term for discussing several major categories. These covered some of the areas concerning powder technology now being vigorously researched and developed such as new powder materials, new technology for powder metallurgy, clean room, plant control, precise filtration and ultra-pure water production, and size control for powder products.



Photos: Powdertec Japan '84

Fluid energy mill

A new-type fluid energy mill (MICRON JET) was recently developed by Hosokawa Micron Corp. (Osaka, Japan). This equipment utilizes the supersonic energy of jet stream of air or other gases to produce fine or super-fine solid particles. It efficiently incorporates both *the pulverizing chamber* where impacts of particles against the rotating ring and high-speed mutual collisions of particles take place and *the classifying chamber* where accurate classification of the ground products can be achieved with Hosokawa Micron Separator. The features are: easy control of product fineness; very narrow particle size range; effective size reduction; space and energy savings.

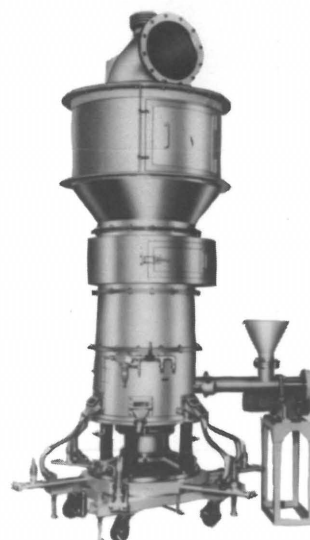


Photo: HOSOKAWA MICRON MICRON JET

Fine metal powder generator

Very fine particulate metal products with a diameter of 100 nm or so can be generated by ARC PLASMA PROCESSOR, which was recently developed by Hosokawa Micron Corp. (Osaka, Japan). The powder is produced so that it can be recovered under non-oxidized conditions. The principle of this unit is based upon the idea that was originally found by the staff of National Research Institute for Metal in the Science and Technology Agency (JP-PAT No.1146170); it utilizes the plasma reaction through which the metal is melted by arc discharge in the atmosphere of Ar and H₂. The features are: continuous feeding of raw material and continuous recovery of products; dislodging of particles on the filter by pulse jet of Ar; easy control of particle surface condition.

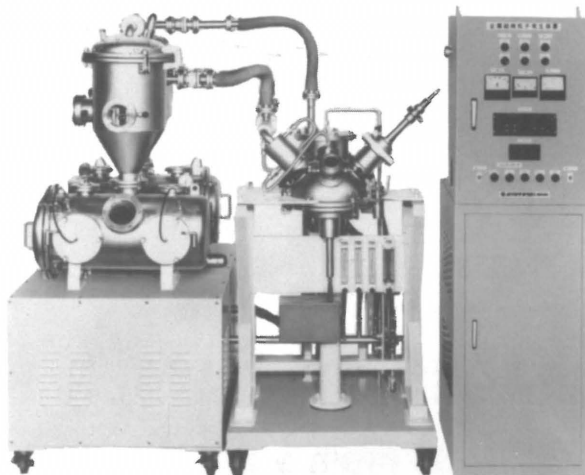
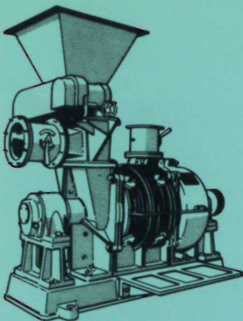
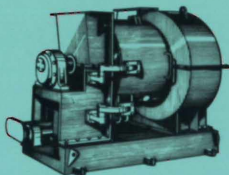
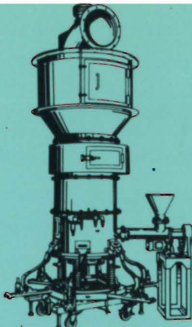
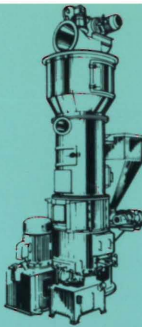
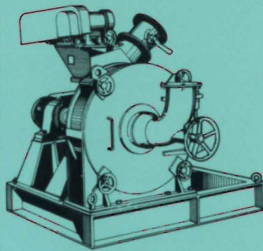
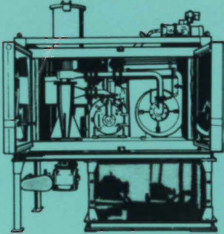
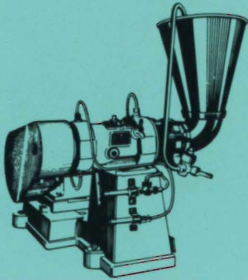
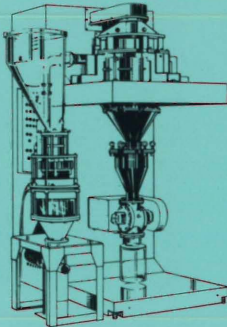
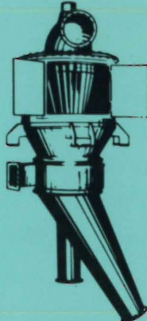
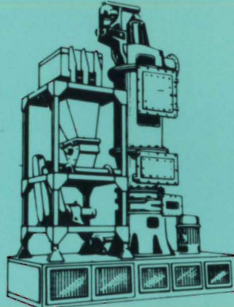
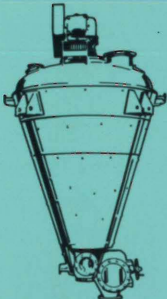

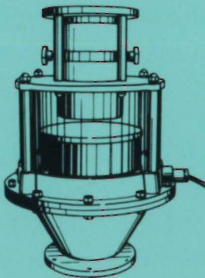
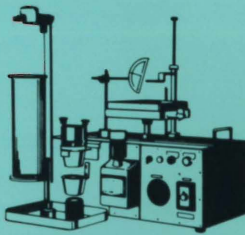
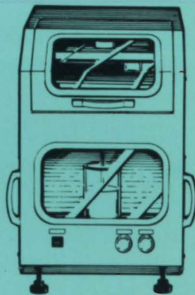


Photo: HOSOKAWA MICRON ARC PLASMA PROCESSOR

				
Ultra-fine grinding Super Micron Mill	Ultra-fine grinding Fine Micron Mill	Ultra-fine pulverizing Micron Jet	Fine-grinding Micron Vertech Mill	Fine-grinding Fine Victory Mill
				
Cryogenic pulverizing Linrex Mill	Homogenizing Disperse Mill	Classifying Super Separator	Classifying Micron Separator	Drying Micron Dryer
				
Mixing/Drying Nauta Mixer-Reactor	Bridge Breaking/ Discharging Bin Activator	Feeding/Discharging Flo-tron	Measurements Powder Characteristics Tester	Particle Size Measuring Sedimenputer

HOSOKAWA

LEADER OF POWDER PROCESSING TECHNOLOGY

From a Single Unit to Complete Treatment System

Hosokawa has specialized in powder processing technology for over 65 years. Today, Hosokawa makes a complete line of advanced equipment for fine-grinding, classifying, drying, mixing, dust collection, measurement and so on. Yet, Hosokawa's most distinguished feature is

its capability of the system engineering that will satisfy a wide variety of industrial needs. Whenever you have a problem, planning, or project relating to powders, first consult with Hosokawa.

HOSOKAWA MICRON CORPORATION

Hosokawa Products are available from:

In Europe (Continent)

Hosokawa-Nauta Europa B.V.
2003 RT Haarlem, Holland,
P.O. Box 773, Nijverheidsweg 25
Telephone: (023) 31 9073
Telex: 41167
Facsimile: 23 318380

In the U.K.

Hosokawa-Nauta (UK) Ltd.
Hughenden Road, High Wycombe
Buckinghamshire, England.
Telephone: (0494) 443866
Telex: 837208
Facsimile: 494 443868

In the U.S.A.

Vibra Screw Incorporated
755 Union Boulevard,
Totowa, N.J. 07511
Telephone: (201) 256-7410
Telex: 685-3382

Other Areas

Hosokawa International Inc.
No.10, 2-chome, Minami-kyutaro Machi,
Higashi-ku, Osaka 541, Japan
Telephone: (06) 261-5141
Telex: J63837
Facsimile: (06) 266-9314